

DISSERTATION

Modeling Spin-Dependent Transport in Silicon

ausgeführt zum Zwecke der Erlangung des akademischen Grades
eines Doktors der technischen Wissenschaften

eingereicht an der Technischen Universität Wien
Fakultät für Elektrotechnik und Informationstechnik

von

Joydeep Ghosh

Theodor-Kramer Str. 10/2/23
A-1220 Wien, Österreich

geboren am 16. September 1982 in Kolkata, Indien

Wien, im März 2016

Kurzfassung

Die wachsenden technologischen Herausforderungen und steigenden Kosten führen zu einem graduellen Ende der MOSFET-Skalierung. Demzufolge werden die fundamentalen physikalischen Grenzen bald erreicht werden, welche einen weiteren Fortschritt in der Rechenkapazität durch ladungsbasierte Bauelemente verhindern. Die Spin-Eigenschaften des Elektrons sind von immensm Interesse aufgrund des Potenzials für zukünftige Spin-basierte mikroelektronische Schaltungen. Moderne ladungsbasierte Elektronik wird hauptsächlich mit dem Materialsystem Silizium gefertigt und es ist daher das Verständnis der Details der Spin-Ausbreitung in Silizium-Strukturen und der Manipulation mit elektrischen Mitteln der Schlüssel zu neuen Spin-basierten Geräteapplikationen.

Die Spin-Relaxierung in modernen Silizium Feldeffekttransistoren wird durch das Wechselspiel zwischen Spin-Orbit-Interaktion und der Elektronenstreuung verursacht. Es wurde zwar eine verstärkte Spin-Relaxation für dünne Silizium-Filme beobachtet, diese kann jedoch durch uniaxialen Stress substanziell unterdrückt werden. Dies macht es extrem vielversprechend für zukünftige Applikationen, da die selbe Stresskonfiguration routinemäßig verwendet wird, um eine Ladungsträgermobilitätserhöhung in modernen MOSFETs zu erzielen. Um die Spin-Flip-Raten zu evaluieren, werden die Wellenfunktionen für die zugehörigen Spin-Up und Spin-Down-Projektionen in Bezug auf die Spin-Injektionsrichtung benötigt. Der $\mathbf{k} \cdot \mathbf{p}$ Hamilton-Operator für zwei Bänder mit der Spin-Orbit-Wechselwirkung, entwickelt nahe dem X -Punkt der Brillouin-Zone, wird dazu verwendet um die Subbandenergien und die Wellenfunktionen in (001) Richtung in ultra-dünnen Siliziumfilmen unter Scherverformung zu bestimmen. Die Subbandwellenfunktionen werden des Weiteren auch zur Evaluierung der zugehörigen Spin-Relaxations-Matrixelemente verwendet. Es wird gezeigt, dass Spin-Flip-Streuprozesse zwischen den zwei [001] Tälern für die Spin-Relaxation in dünnen (001) Siliziumfilmen verantwortlich sind. Die Steigerung der Spin-Lebensdauer (Spin-Kohärenzzeit) ist das Ergebnis der Unterdrückung der Intersubband-Streuung, verursacht durch die scherungsinduzierte Aufspaltung der äquivalenten [001] Täler. Es ist weiters zu beobachten, dass die Spin-Relaxation sensitiv auf die Spin-Injektionsrichtung ist und die Spin-Lebensdauer auf ihr Maximum steigt, wenn die Injektionsrichtung von senkrecht zur Ebene auf in die Ebene der Probe geändert wird.

Eines der Hauptkriterien, um die Spin-basierten Feldeffekttransistor (Spin-FET) zu realisieren, ist es effiziente Spin-Injection in Silizium zu erzielen. Daher ist die Spin-Injektion in Silizium aus einem Ferromagneten durch elektrische Mittel von großen

Interesse. Eine umfassende Studie zur Spin-Drift und -Diffusion in Silizium für Spin-Injektion von einem Ferromagneten einschließlich elektrischer Feldeffekte wird durchgeführt. Um das Widerstandsdiskrepanzproblem zu vermeiden, wird die Spin-Injektionsquelle als ferromagnetischer Halbleiter betrachtet. Der Effekt der Grenzflächenladungsschirmung auf die Spin-Injektionseffizienz wird sorgfältig geprüft. Es ist zu beobachten, dass der Spin-Strom während der Injektion aus einer Ladungsverarmungsregion ansteigt im Vergleich zu einer Injektion aus einer ladungsneutralen oder Akkumulations-Region. Es ist ebenfalls zu beobachten, dass die Spin-Injektionseffizienz immer durch die Spin-Polarisation des magnetischen Materials begrenzt wird. Diese Resultate verlangen nach einer weiteren Untersuchung des Spin-Transports in Silizium, wenn nur durch eine ladungsneutrale und eine Raumladung injiziert wird. Die substanziellen Spin-Transportunterschiede zwischen dem Spin-Injektionsverhalten durch eine Akkumulations- und eine Verarmungsschicht werden untersucht, wobei in beiden Fällen die Spin-Stromdichte nicht signifikant höher sein kann als die Spinstromdichte unter Ladungsneutralität. Daher, für eine fixierte Rand-Spin-Polarisation, ist der maximale Spin-Strom immer durch seinen Wert unter der Ladungsneutralitätsbedingung bestimmt - vorausgesetzt der Ladungsstrom wird konstant gehalten.

Abstract

The growing technological challenges and increasing costs are gradually guiding MOSFET scaling to an end. Hence the fundamental physical limitations will be reached soon, thus preventing further improvements in computational capacity with charged-based devices. The electron spin properties are of immense interest because of their potential for future spin-driven microelectronic devices. Modern charge-based electronics is dominantly fabricated on the material system with silicon, and thus understanding the details of spin propagation in silicon structures and spin manipulation by electrical means is the key for novel spin-based device applications.

The spin relaxation in modern silicon field effect transistors is caused by the interplay between the spin-orbit interaction and the electron scattering. Spin relaxation has been noticed to be stronger in thin films but can be substantially suppressed by uniaxial stress. This makes it extremely promising for future applications as the same stress configuration is routinely used to achieve a charge carrier mobility enhancement in modern MOSFETs. To evaluate the spin-flip rates, the wave functions corresponding to the spin-up and spin-down projections with respect to the spin injection direction are needed. The two-band $\mathbf{k} \cdot \mathbf{p}$ Hamiltonian with the spin-orbit interaction developed near the X -point of the Brillouin zone is used to determine the subband energies and the wave functions in a (001) ultra-thin silicon film under shear strain. The subband wave functions are further used to evaluate the corresponding spin relaxation matrix elements. It is demonstrated that the spin-flip processes between the two [001] valleys are responsible for spin relaxation in thin (001) silicon films. The enhancement of the spin lifetime is the result of the suppression of intersubband scattering caused by the shear strain induced equivalent [001] valley splitting. It is further observed that the spin relaxation is sensitive to the spin injection direction, and that the spin lifetime increases to its maximum, when the injection direction is changed from perpendicular-to-plane to in-plane relative to the sample.

One of the major criteria to realize the spin-based field-effect transistors (Spin-FETs) is to realize efficient spin injection in silicon. Therefore, the spin injection in silicon from a ferromagnet by electrical means is of great interest. A comprehensive study of the spin drift and spin diffusion in silicon for spin injection from a ferromagnet including electric field effects is performed. In order to avoid the impedance mismatch problem, the spin injecting source is considered to be a ferromagnetic semiconductor. The effect of interface charge screening on spin injection efficiency is under scrutiny. It is noted that the spin current increases while injected from a charge-depleted region

in the ferromagnet in comparison to when injected from a charge neutral or an accumulated region. Furthermore it is found that the spin injection efficiency is always limited by the bulk spin polarization of the magnetic material. These results demand a further investigation of the spin transport in silicon, when spin is injected through only a charge neutral and a space-charge layer. The substantial spin transport differences between the spin injection behavior through an accumulation and a depletion layer are investigated, whereas in both cases the spin current density can not be significantly higher than the spin current density at charge neutrality. Therefore, at a fixed boundary spin polarization, the maximum spin current is always determined by its value at the charge neutrality condition - provided the charge current is kept constant.

Acknowledgement

”Lead us from unreal to real, from
darkness to light, from death to
immortality.”

Upanishad

First I want to thank Prof. Siegfried Selberherr who provided me his full support, that made it finally possible to finish this thesis. Also I thank Prof. Selberherr for the working environment that surrounded me and the possibility to participate in international conferences which enriched this research.

I would like to thank Prof. Erasmus Langer, the head of the Institute for Microelectronics, for taking care of all the bureaucracy and providing me with the support letters for different visas and also to receive a travel grant for the 227th ECS meeting.

My deepest gratitude goes to my advisor, Privatdoz. Viktor Sverdlov. He introduced spin physics to me, strained silicon, the $\mathbf{k} \cdot \mathbf{p}$ method, and the spin drift-diffusion model. He helped me to improve my quality of writing for the conference proceedings and the scientific journals. I also thank Professor Marc Bescond for serving on my examination committee.

I am indebted to Dr. Thomas Windbacher for his consistent guidance on my research during the last couple of years, the German translation of the abstract, and the careful proofreading of the thesis. He has been always willing to provide his feedback whenever I needed. I would like to deeply thank Dr. Dmitry Osintsev for his help regarding the computational parts of the momentum relaxation time and the spin lifetime in silicon.

During my work at the institute I had the pleasure to collaborate on different levels with many other colleagues I have a high regard for: Dr. Markus Bina, Dr. Josef Weinbub, and Dr. Karl Rupp. They have helped me to improve my understanding regarding SGFramework, ViennaGrid, and ViennaSHE. Dr. Josef Weinbub also helped me using the Vienna Scientific Cluster.

I would like to mention my wonderful time in Vienna during my stay, taking part in sports, cultural events, and meeting many wonderful persons besides my Phd work. Finally, but not the least, I want to thank my parents Mr. Indra Nath Ghosh and

Acknowledgement

Mrs. Shyamali Ghosh and my elder sister Joyeeta for the endless support and faith in me. My gratitude to them is hard to describe by words.

This work was supported by the European research Council through the grant #247056 MOSILSPIN. The computational results were achieved in part using the Vienna Scientific Cluster (VSC).

Contents

Kurzfassung	ii
Abstract	iv
Acknowledgement	vi
Contents	viii
List of Figures	xi
List of Tables	xvii
List of Abbreviations and Symbols	xviii
List of Constants	xxi
1 Introduction	1
1.1 Spintronics: Historical Background	2
1.2 Silicon Spintronics	3
1.3 Spin Relaxation in Silicon	4
1.4 Spin Injection into Silicon	6
1.5 Outline of the Thesis	8
2 Electronic Band Structure	9
2.1 Band Structure Calculation Methods in Semiconductors	9
2.1.1 Nearly-Free Electron Approximation	10
2.1.2 Tight-Binding Approximation	10
2.1.3 Cellular Method	11
2.1.4 Augmented-Plane Wave Method	12
2.1.5 Pseudopotential Method	12
2.1.6 Perturbation Theory	13
2.1.7 Effective Mass Approximation	14
2.2 Spin-Orbit Coupling	15
2.3 Spin Relaxation in Semiconductors	17
3 $\mathbf{k} \cdot \mathbf{p}$ Hamiltonian and Subband Wave Functions	20
3.1 Silicon Lattice	20

3.2	Effect of Strain on Silicon Band Structure	21
3.2.1	Unstrained Silicon	21
3.2.2	Strained Silicon	24
3.3	Two-Band $\mathbf{k} \cdot \mathbf{p}$ Hamiltonian of [001] Valley at the X-Point	24
3.4	Wave Functions: Analytical Form	26
3.5	Valley Splitting by Shear Strain	31
4	Spin Relaxation	32
4.1	Spin Relaxation Matrix Elements	32
4.2	Spin Hot Spots and Spin Precession	36
4.2.1	Spin Expectation Value	37
4.2.2	Spin Precession	38
4.3	Calculation of the Spin Relaxation Rates	40
4.3.1	Surface Roughness Limited Spin Relaxation Rates	41
4.3.2	Phonons	41
4.3.3	Intravalley and g-Intervalley Relaxation Processes Rates	43
4.4	Spin Lifetime Simulations	47
4.4.1	Spin Lifetime Enhancement with Shear Strain	47
4.4.2	Inter- and Intrasubband Components	49
4.4.3	Effect of Spin Injection Orientation	50
4.5	Momentum Relaxation Time Simulations	53
4.5.1	Momentum Scattering Matrix Elements	53
4.5.2	Calculation of the Momentum Relaxation Rates	56
4.6	Valley Splitting in Unstrained Films	58
4.6.1	Spin Relaxation Matrix Elements	59
4.6.2	Spin Lifetime Calculations	60
4.7	Primed Subbands and f-Processes	63
4.7.1	Primed $\mathbf{k} \cdot \mathbf{p}$ Hamiltonian	63
4.7.2	Optical Phonon Limited Spin Relaxation Rate	63
4.7.3	Optical Phonons in Spin Lifetime	64
5	Spin Diffusion in Silicon	69
5.1	Semi-Classical Model of Charge Transport	69
5.1.1	Poisson's Equation	69
5.1.2	Continuity Equations	70
5.1.3	Drift-Diffusion Equations	70
5.1.4	Quasi-Fermi Levels	72
5.2	Spin Transport Equations	73
5.2.1	Spin Continuity Equation	73
5.2.2	Spin Drift-Diffusion	74
5.2.3	Discretized Form	75
5.2.4	Transport Channel	78
5.3	Solution	79
5.3.1	Solution with Charge Neutrality Constraint	79

5.3.2	Solutions without Charge Neutrality Constraint	83
5.4	Spin Diffusion from a Space-Charge Layer	87
5.4.1	Solution with Charge Neutrality Constraint	88
5.4.2	Solution without Charge Neutrality Constraint	94
6	Summary and Outlook	101
	Bibliography	103
	Own Publications	118
	Curriculum Vitae	122

List of Figures

2.1	Schematic plot of a pseudopotential and the pseudo-wave function in the real space (red), compared to the original ones (blue), is shown.	12
2.2	Bloch sphere with different qubit states corresponding to the axes is shown. The position of an arbitrary state (χ) can be uniquely represented by the polar (Θ) and the azimuthal angles (Φ).	16
2.3	Schematic of the Elliot-Yafet and D'yakonov-Perel' spin relaxation mechanisms.	18
3.1	Sketch of the diamond crystal lattice is portrayed. Colors gray and red represent A' atoms and color blue represents A'' atoms. For silicon, both atoms are identical.	21
3.2	The first Brillouin zone of the relaxed silicon lattice is shown. The valley positions and high symmetry points are shown as well.	22
3.3	The silicon band structure calculated by the pseudopotential method (CB is the conduction band, and VB is the valence band) is described. The VB edges are located exactly at the Γ -point and the minimum of the lowest CB lies on the symmetry Δ line close to the X -point. The lowest two CBs degenerate exactly at the X -point.	23
3.4	Left: constant energy surface of unstrained silicon (six-fold degeneracy) is shown, right: conduction band splitting under shear tensile strain on (001) plane is shown. The red (green) color-fill signifies high (low) electron concentration.	23
3.5	Sketch showing the spin injection into a (001) thin silicon film of thickness t in an arbitrary direction, described by the polar angle Θ	28
3.6	The large component of the wave function of the lowest unprimed subband in an unstrained film located in the valley centered at k_0 is shown. $\Theta = \frac{\pi}{3}$ (c.f. Figure 3.5) is maintained.	28
3.7	The absolute value of the large (small) component of the spin wave functions reduces (increases), when the spin injection changes gradually from OZ - to OX -direction. k_x , k_y , and ε_{xy} are set to be 0.4nm^{-1} , 0.4nm^{-1} , and 0.5% respectively.	29
3.8	Intersubband splitting is shown as a function of shear strain ε_{xy} for different values of the sample thickness t , and for $k_x=0.25\text{nm}^{-1}$ and $k_y=0.25\text{nm}^{-1}$	30

4.1	The normalized and squared intersubband spin relaxation matrix element ($ M_S ^2$) is shown as function of the shear strain ε_{xy} , and for an arbitrary (k_x, k_y) pair (sample thickness $t=2\text{nm}$). Spin is oriented along OZ -direction ($\Theta=0$, c.f. Figure 3.5). The splitting of the lowest subbands (valley splitting) is also shown.	33
4.2	The normalized intersubband spin relaxation matrix element (c.f. Equation 4.1) for an unstrained sample is shown, with the Fermi distribution at 300K.	33
4.3	The normalized intersubband spin relaxation matrix element for $\varepsilon_{xy}=0.2\%$ is shown, with the Fermi distribution at 300K.	34
4.4	The variation of the normalized intersubband spin relaxation matrix elements with the kinetic energy of the conduction electrons in $[110]$ direction is depicted. The influence of the spin injection direction is also shown ($t=1.36\text{nm}$).	35
4.5	The variation of the normalized intersubband spin relaxation matrix elements with Θ (c.f. Figure 3.5) and ϕ_1 (with $\tan(\phi_1) = -\frac{k_y}{k_x}$) is described. The domain for Θ is chosen to be $(0, \frac{\pi}{2})$ as it is repeated in the rest of the domain $(\frac{\pi}{2}, \pi)$	36
4.6	The dependence of the total spin expectation (S_{OZ}) over a certain (k_x, k_y) pair is shown, when spin is injected along the OZ -direction ($\varepsilon_{xy}=0.5\%$).	38
4.7	The dependence of the total spin expectation (S_{OX}) over a certain (k_x, k_y) pair is shown, when spin is injected along the OX -direction ($\varepsilon_{xy}=0.5\%$).	39
4.8	The precession of the injected spin (along OX - and OZ -directions) around the existing spin-orbit field (SOF) is portrayed ($\tan \phi_1 = -\frac{k_y}{k_x}$).	39
4.9	The four phonon modes are found in elemental semiconductors: (a) longitudinal acoustic, (b) transversal acoustic, (c) longitudinal optical, and (d) transversal optical modes.	41
4.10	The dependence of the spin lifetime including the surface roughness (SR), the longitudinal acoustic (LA) phonon, and the transversal acoustic (TA) phonon mediated components on the temperature and for different values of the electron concentration ($\varepsilon_{xy}=0$, $t=1.36\text{nm}$) is shown.	48
4.11	The dependence of the spin lifetime and its surface roughness and acoustic phonon induced components over a wide range of ε_{xy} is shown. The film thickness is $t=2.5\text{nm}$, $T=300\text{K}$, and the electron concentration is $N_S=10^{12}\text{cm}^{-2}$	48
4.12	The dependence of the spin lifetime on the shear strain ε_{xy} is depicted for a film thickness of $t=1.36\text{nm}$, and an electron concentration of $N_S=10^{12}\text{cm}^{-2}$	49
4.13	The variation of the spin lifetime with its inter- and intrasubband components with ε_{xy} is shown. The film thickness is $t=2.1\text{nm}$, $T=300\text{K}$, and the electron concentration is $N_S=10^{12}\text{cm}^{-2}$	50

4.14	The variation of the surface roughness mediated spin lifetime with its inter- and intrasubband components as a function of ε_{xy} at two distinct values of temperature is depicted. The film thickness is $t=1.36\text{nm}$, and the electron concentration is $N_S=10^{12}\text{cm}^{-2}$. The variation of the Fermi levels and the minimum energies ($k_x=k_y=0$) of the lowest unprimed subbands with ε_{xy} is shown (inset).	51
4.15	The variation of the surface roughness and the phonon mediated components of the spin lifetime with ε_{xy} is shown, when the spin injection orientation (represented by the angle Θ) is used as a parameter. The film thickness is $t=1.36\text{nm}$, $T=300\text{K}$, and the electron concentration is $N_S=10^{12}\text{cm}^{-2}$	52
4.16	The variation of inter- and intrasubband components of the spin lifetime with ε_{xy} is depicted, when Θ is used as a parameter (c.f. Figure 4.16).	52
4.17	The variation of the spin lifetime with the spin injection orientation angle Θ at any fixed value for ε_{xy} is shown. The analytical expression can be found at Equation 4.37.	53
4.18	The normalized and squared intersubband scattering matrix element is shown as function of ε_{xy} and for several pairs of (k_x, k_y) . The film thickness is set to $t=2\text{nm}$	54
4.19	The subband energies for the first and the minimum of the second subband (i.e. at $k_x=k_y=0$) as a function of ε_{xy} with the same conditions as in Figure 4.18 is shown. The points where the two cross are highlighted by arrows.	55
4.20	The normalized and squared intrasubband scattering matrix elements are shown as function of ε_{xy} ($k_x=k_y=0.25\text{nm}^{-1}$, and $t=2.7\text{nm}$).	55
4.21	The variation of the momentum relaxation time with ε_{xy} is shown with its surface roughness (SR) and phonon (Ph) mediated components at two distinct temperatures. The film thickness is $t=1.36\text{nm}$, and the electron concentration is $N_S=10^{12}\text{cm}^{-2}$	57
4.22	The variation of the momentum relaxation time with ε_{xy} is shown with its inter- and intrasubband components corresponding to Figure 4.21.	57
4.23	The variation of the normalized and squared intersubband spin relaxation matrix elements as function of ε_{xy} is depicted, where $k_x=0.3\text{nm}^{-1}$, $k_y=1\text{nm}^{-1}$, and for different values of Δ_Γ ($t=2.72\text{nm}$).	59
4.24	The variation of the normalized and squared intersubband spin relaxation matrix elements with ε_{xy} is shown, when the spin injection direction is taken as a parameter ($\Delta_\Gamma=5.5\text{eV}$, $t=1.36\text{nm}$).	60
4.25	The variation of the surface roughness (SR) and the phonon (Ph) mediated spin lifetime with ε_{xy} is shown, when all possible values for Δ_Γ (c.f. Equation 4.45) are considered. The sample thickness is $t=2.72\text{nm}$, $T=300\text{K}$, and the electron concentration is $N_S=10^{12}\text{cm}^{-2}$	61
4.26	The energies of the two lowest unprimed subbands with ε_{xy} at two distinct Δ_Γ values are shown. The sample thickness is $t=2.72\text{nm}$, $T=300\text{K}$, and the electron concentration is $N_S=10^{12}\text{cm}^{-2}$	62

4.27	The variation of the spin lifetime and its inter- and intrasubband components with ε_{xy} are depicted, when $t=2.72\text{nm}$, the electron concentration $N_S=10^{12}\text{cm}^{-2}$, and $\Delta_\Gamma=5.5\text{eV}$	62
4.28	The variation of the spin lifetime and its surface roughness (SR), the longitudinal (LA) and the transversal (TA) acoustic phonon mediated components with ε_{xy} is shown. $\Delta_\Gamma=5.5\text{eV}$ (c.f. Equation 4.45), the sample thickness $t=1.36\text{nm}$, $T=300\text{K}$, and the electron concentration $N_S=10^{12}\text{cm}^{-2}$ are used.	64
4.29	The variation of the spin lifetime and its components (along with the optical phonon Op mediated component) with ε_{xy} is shown when $t=2.72\text{nm}$ and the other parameters are as given in Figure 4.28.	65
4.30	The variation of the spin lifetime and its components with ε_{xy} is shown when $t=4.34\text{nm}$ and the other parameters are as given in Figure 4.28.	65
4.31	The dependence of the minimum energies for primed and unprimed subbands as well as the Fermi energy on strain is shown for Figure 4.30.	66
4.32	The prediction of the spin lifetime with the valley splitting results (c.f. Figure 4.26) is highlighted.	67
4.33	The variation of the spin lifetime with the valley splitting is described, when $\Delta_\Gamma=5.5\text{eV}$. The sample thickness is $t=1.36\text{nm}$, $T=300\text{K}$, and the electron concentration is $N_S=10^{12}\text{cm}^{-2}$. The spin injection orientation is used as a parameter.	68
5.1	The two-dimensional representation of the Voronoi box is shown. The domain \tilde{V}_i contains the mesh point i and is surrounded by six adjacent mesh points. $A_{i,j}$ represents the boundary between the box around the i^{th} node and its neighbor j . $d_{i,j}$ implies the distance between the i^{th} and the j^{th} nodes.	76
5.2	The schematic shows the simulation set up for the spin injection in Si from a ferromagnetic semiconductor (FMS). The left boundary ($x = -\frac{W}{2}$) is grounded, and the right boundary ($x = \frac{W}{2}$) is under the voltage bias (U_c). The interface is shown as a dotted line. The doping (effective density of states) in the Si side is N_D (N_C), and in the FMS is K_1N_D (K_2N_C).	78
5.3	The analytically calculated spin densities in the channel are shown, when the applied voltage (U_c) is used as a parameter. The bulk spin polarization in the ferromagnetic semiconductor (FMS) is $P=20\%$	82
5.4	The spin current density (α_0) and spin density (β_0) injection efficiencies at the Si interface are shown as a function of the applied electric field \tilde{E} . Lines \rightarrow theory and dots \rightarrow simulation ($P=10\%$).	83
5.5	The spin current density (α_0) and spin density (β_0) injection efficiencies at the Si interface as a function of the applied electric field \tilde{E} (c.f. Figure 5.4) is shown ($P=50\%$).	84

5.6	A plot of $M_{up} = V_T \ln \left(\frac{n_{\uparrow}}{n_{\uparrow}^{eq}} \right)$ and $M_{down} = V_T \ln \left(\frac{n_{\downarrow}}{n_{\downarrow}^{eq}} \right)$ through the bar ($P=10\%$, $\frac{ q\tilde{E} }{K_B T} = 2\mu\text{m}^{-1}$ where \tilde{E} is the applied electric field) is depicted, showing a discontinuity at the junction, which gives the term G (c.f. Equation 5.35a and Equation 5.35b). n_{\uparrow}^{eq} (n_{\downarrow}^{eq}) is the up(down)-spin concentration at the thermal equilibrium.	85
5.7	The spin density accumulation near the junction over a channel of $4\mu\text{m}$ is shown, when the current density (J_n) is fixed to $23.4\text{MA}/\text{m}^2$ with $P=20\%$. K_1 is used as a parameter (c.f. Table 5.1). λ_D represents the Debye length (c.f. Equation 5.30).	86
5.8	The variation of the electric potential through the channel is described, related to Figure 5.7.	86
5.9	The spin current density through the channel is shown, with the same conditions as in Figure 5.7. With the notations as described in Equation 5.16b and Equation 5.19b, the direction of the spin current is from the ferromagnetic semiconductor FMS towards Si.	87
5.10	The spin density accumulation through the channel is depicted, with the same conditions as in Figure 5.7. Both K_1 and K_2 are used as parameters (c.f. Table 5.1).	88
5.11	The spin density and the spin current density injection efficiencies (β_D and α_D respectively) are shown, taken at a Debye length away from the interface towards Si, with the same conditions as in Figure 5.7.	89
5.12	The schematic portrays the simulation set up for the spin injection in a Si bar. The left boundary ($x=0$) is grounded, and the right boundary ($x = W$) is under a voltage bias (U_c).	89
5.13	The analytically (c.f. Equation 5.44) calculated spin densities through the channel are shown. The boundary spin density polarization $\beta_0=50\%$. The channel length is $3\mu\text{m}$	90
5.14	The analytically (c.f. Equation 5.47) calculated spin current densities are shown, corresponding to Figure 5.13. The directions of the drift and the diffusive components of the spin current density are highlighted.	90
5.15	The variation of the spin current density in the channel with the boundary spin density polarization β_0 is shown, when no voltage is applied.	91
5.16	The schematic depicts the spin extraction phenomenon from the Si bar towards the left boundary ($x=0$). The left boundary is under zero-bias, and the right boundary ($x = W'$, where $W' \gg L_i$ with L_i as the intrinsic spin diffusion length) is under a negative bias ($U_c < 0$). The direction of the electric field is also shown.	92
5.17	The normalized critical current density is shown for spin-blockade as a function of the boundary current density spin polarization.	94
5.18	The variation of the electron current density with M_{Ch} (c.f. Equation 5.57) and the bias voltage U_c is depicted, when the channel length is $4\mu\text{m}$	95

5.19	The electron concentration is shown near the charge injection boundary (c.f. Equation 5.57). The current density is 11.9MAm^{-2} , and the channel length $4\mu\text{m}$. λ_D represents the Debye length.	96
5.20	The variation of the spin current density is delineated with the same conditions as in Figure 5.19.	96
5.21	The spin current density is shown for up to 5 times the Debye length λ_D from the left boundary, when spin is injected from a charge neutral and charge accumulated source. The carrier current is absent. The left boundary for (1) is set with $n_{\uparrow 0}=900N_D$ and $n_{\downarrow 0}=100N_D$, and for (2) c.f. Equation 5.57.	97
5.22	The charge and the spin distribution over the channel are shown under the charge accumulation and with the boundary condition Equation 5.57 ($M_{Ch}=100\text{mV}$, $U_c=-300\text{mV}$). The inset figure shows the spin density polarization β near the spin injecting interface. The current density 11.9MAm^{-2} is maintained over a $4\mu\text{m}$ channel.	98
5.23	The spin and spin current densities in depletion ($M_{Ch}=-100\text{mV}$, $U_c=-140\text{mV}$) and for charge neutrality ($U_c=-204\text{mV}$) with the boundary as in Equation 5.57 are shown. The inset figure shows the spin density polarization β . The current density 11.9MAm^{-2} is maintained over a $4\mu\text{m}$ channel.	98
5.24	The spin current densities with their up(down)-spin components are depicted, when the channel is in depletion ($M_{Ch}=-100\text{mV}$) with the boundary as in Equation 5.57. The current density 7.9MAm^{-2} is maintained.	99
5.25	The spin current density for accumulation, charge neutrality, and depletion with the boundary condition Equation 5.57 are shown. The current density 7.9MAm^{-2} is maintained.	99

List of Tables

3.1	The symmetry points of the first Brillouin zone in silicon are listed according to Figure 3.2 are listed.	22
3.2	The parameter list for the silicon lattice is shown.	25
5.1	The simulation parameters for the spin drift-diffusion equations are listed.	79
5.2	The spin injection parameters with their optimum values are shown. .	82

List of Abbreviations and Symbols

MOSFET	metal-oxide-semiconductor field-effect transistor
CMOS	complementary MOSFET
SOI	silicon on insulator
GMR	giant magnetoresistance
TMR	tunnel magnetoresistance
MRAM	magnetoresistive random-access memory
SpinFET	spin field-effect transistor
FinFET	fin-shaped field-effect transistor
MTJ	magnetic tunnel junction
STT	spin transfer torque
UTB	ultra-thin body
SOC	spin-orbit coupling
SOF	effective spin-orbit field
EY	Elliot-Yafet mechanism
DP	D'yakonov-Perel' mechanism
DOS	density of states
FMS	ferromagnetic semiconductor
TCAD	technology computer aided design
q	fundamental charge
m_e	electron rest mass
ϵ_0	vacuum permittivity
ϵ_{Si}	silicon permittivity
a	silicon lattice constant
K_B	Boltzmann constant
\hbar	reduced Planck constant
E_F	Fermi level
\mathbf{k}	wave vector
\mathbf{p}	momentum vector
k_0	position of the valley minimum relative to the X -point in unstrained silicon
$k_{0\Gamma}$	position of the valley minimum relative to the Γ -point in unstrained silicon
m_t	transversal effective mass of silicon
m_l	longitudinal effective mass of silicon
$\tilde{U}(z)$	confinement potential
c	speed of light
E	electron energy
\tilde{m}	electron effective mass

$\sigma_{x,y,z}$	Pauli matrices
T	temperature
t	film thickness
Δ_{SO}	spin-orbit splitting
ε_{xy}	shear strain component
N_S	electron concentration
L	autocorrelation length
Δ	mean square value of the surface roughness fluctuations
D	shear deformation potential
Ξ	acoustic deformation potential
D_{OP}	optical deformation potential
ν_{TA}	transversal acoustic phonon velocity
ν_{LA}	longitudinal acoustic phonon velocity
ω_{op}	frequency of the optical phonons
τ_s	spin lifetime
τ_m	momentum relaxation time
Θ	polar angle defining the spin injection orientation in (001) plane
Φ	azimuthal angle defining the spin injection orientation in (001) plane
Δ_{Γ}	splitting at Γ -point in unstrained silicon
\mathbf{J}_n	electron current density vector
\mathbf{J}_p	hole current density vector
μ_n	electron mobility
μ_p	hole mobility
D_n	electron diffusion coefficient
$\tilde{\mathbf{E}}$	electric field vector
V	electric potential
N_D	donor doping concentration per unit volume
N_C	effective density of states in the conduction band
∇	nabla operator
\tilde{t}	time
V_T	thermal potential
n_{\uparrow}	up-spin electron concentration per unit volume
n_{\downarrow}	down-spin electron concentration per unit volume
s	spin concentration per unit volume
M_{\uparrow}	up-spin chemical potential
M_{\downarrow}	down-spin chemical potential
G	spin chemical potential drop
P	bulk spin polarization (ferromagnet)
\mathbf{J}_s	spin current density vector
L_i	intrinsic spin diffusion length
λ_D	Debye charge screening length
L_u	up-stream spin diffusion length
L_d	down-stream spin diffusion length

α	polarization for spin current density
β	polarization for spin density
α_0	polarization for spin current density at the boundary
β_0	polarization for spin density at the boundary
$B(x)$	Bernoulli function

List of Constants

K_B	$8.617332478 \cdot 10^{-5}$ (eV/K)
\hbar	$1.05457172647 \cdot 10^{-34}$ (Js)
m_e	$9.1093829140 \cdot 10^{-31}$ (Kg)
q	$1.60217656535 \cdot 10^{-19}$ (C)
c	299792458 (m/s)
m_t	$0.19m_e$
m_l	$0.91m_e$
M	$(m_t^{-1} - m_e^{-1})^{-1}$
L	$15 \cdot 10^{-10}$ (m)
Δ	$3 \cdot 10^{-10}$ (m)
ρ	2329 (Kg/(m ³))
ν_{TA}	5300 (m/s)
ν_{LA}	8700 (m/s)
a	$5.431 \cdot 10^{-10}$ (m)
k_0	$0.15 \cdot 2\pi/a$
$k_{0\Gamma}$	$0.85 \cdot 2\pi/a$
D	14 (eV)
Ξ	12 (eV)
D_{SO}	15meV/ k_0
D_{OP}	6.5meV $\cdot 2\pi/a$
Δ_{SO}	1.27 meVnm
ω_{op}	$9.29791719 \cdot 10^{13}$ (Hz)
ϵ_0	$8.854187 \cdot 10^{-12}$ (F/m)
ϵ_{Si}	11.7 ϵ_0

1 Introduction

”The mind is everything. What you think you become.”

Gautam Buddha

Over the last several decades, Moore’s law has successfully predicted the persistent miniaturization of semiconductor devices, such as the transistors in microprocessors [1]. Following that and owing to the continuous demand for cheap electronics with increased performance, CMOS scaling became the key to stay competitive on the semiconductor market. The ITRS [2] offers a commonly accepted guideline for a collective effort to the upcoming technology generations. Due to the struggle to keep control over the channel in CMOS devices when scaling them down, new processes, materials, and device structures were introduced [3], e.g., local and global strain techniques, high- k /metal gates, and multi-gate three-dimensional transistors [4]. It is hereby mentioned that while introducing the new technologies the speed, size, leakage [5], economic limitations [6], and power consumption of the transistors have been kept in the mind.

The principle of MOSFET operation is based on the charge degree of freedom. The charge of an electron interacts with the gate induced electrostatic field, which in turn controls the electron flow in the channel by modulating the potential barrier. Attempts to use another fundamental property of an electron, its spin, have given rise to a new and rapidly evolving field known as spintronics. It is an acronym for spin transport electronics that was first introduced in 1996 to designate a program of the U.S. Defense Advanced Research Projects Agency (DARPA) [7]. The electron spin state is characterized by one of its two possible projections on a given axis, and thus could be potentially used in digital information processing. Two major transport parameters viz. spin lifetime and the spin diffusion length determine the scale of coherence in spintronic devices [8]. Since these parameters are several orders of magnitude larger in semiconductors than in metals [9, 10], semiconductors are promising materials for the spintronics research. Utilizing the spin properties in semiconductors also opens great opportunities to reduce the device power consumption for future electronic circuits, as it takes an amazingly small amount of energy to invert the spin orientation which is necessary for low power applications [11]. In modern times, spintronic devices [12, 13, 14, 15, 16]; particularly magneto-resistive devices [17] with a tunnel barrier junction structure [18]; are strong candidates to be used in memory technology due to their non-volatility and compatibility with CMOS technology [19, 20]. One

has to mention that by using the inherent quantum mechanical nature of spin to construct quantum computers for quantum information processing and efficient quantum mechanical simulations is also under investigation [21, 22].

1.1 Spintronics: Historical Background

The electron was discovered way back in 1897 by J. J. Thomson, and the electron charge was measured with perfection by R. Millikan. The presence of a magnetic moment for electrons was discovered in the year of 1922 [23], and later on it was also established that the electron spin is quantized. Wolfgang Pauli formalized the theory of spin in 1927 by using the basic foundations of quantum mechanics. He pioneered the description of the spin state by introducing the so-called Pauli matrices. A study on spin polarized tunneling on ferromagnetic/insulator/superconducting aluminum junctions was made [24]. This showed the conservation of the spin in electron tunneling, and gave rise to the possibility of spin sensitive tunneling between two ferromagnetic films. Later Mikhail D'yakonov and Vladimir Perel' predicted the spin Hall effect in 1971 - a spin flow perpendicular to the current flow direction [25]. Subsequently, the first experimental confirmation of the prediction was made [26]. Julliere in 1975 discovered an increase in resistance (10 % at 4.2 K), when the magnetic layers in a Fe/Ge/Co stack were switched from the parallel to the anti parallel configuration (the first experiment on tunnel magneto-resistance TMR) [27]. The proposal for the idea that the spin-polarized current can be injected into a semiconductor when a current is passed through a ferromagnet/semiconductor junction was made in 1976 [28]. However, it took until the 1980's for the process technology to be able to fabricate multi-layered devices with each layer thickness in the range of nanometers. The Physics Nobel Prize in 2007 was given to Peter Grünberg and Albert Fert for the discovery of the giant magnetoresistance (GMR) in ferromagnetic thin film multi-layers [29], which showed the general agreement on the importance of spintronics.

Currently, the advancements in TMR technology [30] led to a switch towards TMR-based read heads. Exploiting the TMR effect for the magnetic field sensing is advantageous due to the much higher resistance of the layer stack ($K\Omega$ instead of Ω) and at least one order of magnitude bigger resistance modulation ($\sim 300\%$ in comparison to $\sim 5\%$) [31]. The magnetic random access memory (MRAM) devices are a further important and practical spintronic device class. The initial MRAM devices were based upon the GMR effect, but due to the advances in TMR stacks the MRAM devices transitioned to TMR based structures [32], as produced by Freescale Semiconductor and IBM. Recently, another technique known as spin transfer torque (STT) magnetization switching has received great attention [33, 34, 35, 36]. STT-MRAM facilitates the control of the magnetization by entirely electrical means, thus featuring better scaling capabilities, and requires less switching energy. Another goal of spintronics has been to envision spin-based logic devices to replace the charge-based logic devices. The STT-MTJ technology has been reported to be attractive for building logic configurations,

which combines non-volatile memories and the logic circuits (logic-in-memory architecture [37]) in order to overcome the scaling obstacles of CMOS logics [38, 39, 11, 40].

The idea of a spin field-effect transistor, or SpinFET, is to control a spin signal analog to the charge-based transistor via applied voltage instead of a magnetic field. They are attractive candidates as basic for spin-driven integrated circuits. The first spin field effect transistor (SpinFET) was proposed by Datta and Das [41] in 1990, which is composed of two ferromagnetic terminals separated by a non-magnetic material. A good elaboration of the device structure of a spin transistor, operating principle, and performance can be found in [42]. The spin injection in semiconductors by different means is a topic under intense research, and will be highlighted later. However, if one is able to resolve the problem of spin injection into a semiconductor with sufficient accuracy, the next challenge will be the manipulation and control of the spin transport through the conducting channel. This is usually achieved by applying an external magnetic field to rotate the spin, although in principle the presence of spin-orbit coupling (SOC) allows to control spin electronically. Indeed, the SOC in the semiconductor heterostructures can be tailored by voltage gates on the top of the heterostructures, hence allowing to control the spin by voltage [41]. The practical realization of such structures is still a research topic, and hence the proper understanding of the spin-orbit coupling in semiconductors must be further developed.

1.2 Silicon Spintronics

As the SpinFET's operation demands the presence of a rather strong spin-orbit coupling SOC, the focus of the research has been concentrated on III-V materials which have a strong SOC. Therefore, until recently, silicon, the main material used by modern microelectronics, was kept aside from the main stream spin-related applications. On the other hand, there also have been predictions on alternative channel materials with a mobility higher than in silicon [43]. However, silicon possesses several properties attractive for spintronics [44]: it is composed of nuclei with predominantly zero spin [45] and it is characterized by a weak spin-orbit coupling [46, 47, 48]. Along with this, the spatial inversion symmetry of the lattice results in the absence of the Dresselhaus effective spin-orbit interaction [49] which results in a low relaxation rate accompanied by a longer spin lifetime as compared to other semiconductors. In fact, silicon has the longest spin lifetime of any inorganic bulk semiconductor at room temperature [48]. At the saturation drift velocity of silicon ($\approx 10^7 \text{ cm s}^{-1}$), this corresponds to a transport length scale exceeding 1mm [50]. It is therefore an attractive material for propagating spin information over a long distance. The use of silicon for spin driven devices would greatly facilitate their integration with MOSFETs on the same chip. These characteristics have motivated a wide interest in silicon spintronics [51, 52, 53]. The proposal of a spintronic device facilitating silicon that uses spin at every stage of its operation [54] is very important on the transition from charge-based CMOS towards a purely spin-based successor (i.e. an all-spin logic device) [11].

1.3 Spin Relaxation in Silicon

Because of the paramount importance of silicon on insulator (SOI) and FinFET 3D technology for the technology nodes from 22nm to 14nm and beyond in order to achieve a tighter confinement and thus better electrostatic control to support miniaturization as discussed earlier, it is expected that spin relaxation will further increase in the conducting channels [55]. A systematic investigation of the electron spin relaxation time in silicon was conducted a long time ago [56]. The estimate for the spin lifetime at room temperature obtained is of the order 0.1-10ns [44], which corresponds to a spin diffusion length maximum of $2\mu\text{m}$. A long spin transfer distance of conduction electrons through an undoped $350\mu\text{m}$ thick silicon wafer has been shown in a ground breaking experiment [57], and hence the spin propagation up to such a distance combined with the possibility of injecting spin at room [58] or even at elevated temperature [59] makes the fabrication of spin-based switching devices made of silicon quite plausible in the near future. In contrast, a large experimentally observed spin relaxation in electrically-gated silicon structures is an obstacle for a successful realization of spin-driven devices [60, 61]. Therefore, more research on all of the different spin relaxation mechanisms and also means to improve the spin lifetime in silicon films is needed.

The spin lifetime is determined by the spin-flip processes, and several spin relaxation mechanisms in a semiconductor can be attributed [62]. The two most significant relaxation mechanisms in metals and in semiconductors are the Elliot-Yafet [63, 64] (EY) mechanism and the D'yakonov-Perel' [65] (DP) mechanism, and this will be explained in detail in the following chapters.

It is well known that the conduction band in silicon consists of three pairs of equivalent valleys, with their energy minima located close to the corresponding X -points of the first Brillouin zone. The theory of spin relaxation in thin silicon films must account for the most relevant scattering mechanisms which are due to the electron-phonon (Ph) interaction and the surface roughness (SR) scattering [66, 63, 67, 68]. The surface roughness at the two interfaces is assumed to be equal and statistically independent. It is described by a mean and a correlation length [69]. The spin relaxation due to the electron-phonon interaction is taken care of in the deformation potential approximation [70]. The electron-phonon interaction can further be distinguished into two sub-categories. The acoustic-phonon mediated relaxation, i.e. the longitudinal(LA)- and the transversal(TA)-acoustic phonons, and the optical phonons. The most prominent contribution to the spin relaxation in bulk silicon has been identified to be due to the optical (Op) phonon scattering between the valleys residing at different crystallographic axes [53, 71]. Nevertheless, in order to investigate the impact of the surface roughness and the acoustic phonon mediated spin-flip, only the relevant [001] oriented valley pair with spin degree included must be considered, as it produces the low energy unprimed subband ladder under the confinement potential [72]. The unprimed subbands in the unstrained (001) film are degenerate, without spin-orbit effects in-

cluded [72]. An accurate inclusion of the intrinsic spin-orbit interaction results in a large mixing between the spin-up and spin-down states, resulting in spin hot spots characterized by strong spin relaxation. To remove this spin mixing and thus increase the spin lifetime one has to introduce mechanical stress into such structures.

The influence of stress on the carrier (both electron and hole) transport in semiconductors [73] has been known for over half a century. That the application of stress may influence the intrinsic electron mobility in silicon was predicted by Hall and Bardeen in 1951 [74]. The development of the generalized deformation potential theory can be accredited to [75, 76] explaining this effect. Nowadays, stress is regularly used in industry to efficiently increase the transistor drive current by enhancing the mobility of carriers in the channel [77, 78], as well as in non-classical CMOS structures [79, 80]. The strain ε_{xy} produced by an uniaxial tensile shear stress in [110] direction is known to lift the degeneracy between the unprimed subbands in the [001] oriented valley pair [72], thus it is predicted to decrease the mentioned spin mixing in such a way that the intersubband spin relaxation rate is reduced and the spin lifetime gets enhanced.

Now in order to calculate the spin lifetime, one needs to know the spin relaxation matrix elements. To estimate the matrix elements, the subband wave functions and also the eigenenergies must be known [81, 72]. One way to calculate the subband wave functions is to use the $\mathbf{k} \cdot \mathbf{p}$ method.

The $\mathbf{k} \cdot \mathbf{p}$ method was first introduced by Seitz [82] and later extended to study semiconductor band structures [83, 84, 85]. This method in combination with a Hamiltonian including strain [86] has been a reliable and computationally inexpensive method to study the stress-induced valence band modification. An effective two-band $\mathbf{k} \cdot \mathbf{p}$ based method for the relevant [001] oriented valley pair written at the vicinity of the X -point suitable to describe the electron subband structure in the presence of the shear strain ε_{xy} [72] is generalized to include the spin degree of freedom [71]. The height of the potential barrier corresponds to the potential energy barrier at the semiconductor-oxide interface for a silicon-on-insulator (SOI) structure.

In this work the subband wave functions and the eigenenergies of the unprimed valley pair are scrutinized, and the corresponding matrix elements are shown. The spin lifetime calculation steps are explained. A giant enhancement of the spin lifetime with all its components as a function of the shear strain is elucidated. The role of inter- and intrasubband transitions in determining the spin lifetime is explained, and the role of the former is observed to be dominant. In contrast and under the same conditions, the momentum relaxation time is found to be solely determined by the intrasubband transitions. The subband energies of the primed valley pair is taken into account to incorporate the influence of the optical phonons. The increase of the optical phonon mediated spin lifetime is not found to be as severe as the other mechanisms. The unprimed subband splitting in a relaxed silicon structure [87] has also been a prominent area of research for a long time, and this is incorporated to estimate the splitting between the equivalent subbands, the matrix elements, and finally the spin relaxation time.

The spin injection direction sensitive spin lifetime model is investigated in detail. It is observed that an arbitrary spin injection direction modifies the subband wave functions, the intersubband spin relaxation matrix element, and henceforth all the distinct spin relaxation mechanisms.

1.4 Spin Injection into Silicon

One of the major criteria to realize the SpinFET device is to realize efficient spin injection in the conducting channel. The spin polarization can be achieved by optical spin excitation with circularly polarized light [88, 89]. Unlike e.g. GaAs, silicon is an indirect band gap semiconductor, so optical orientation or luminescence become ineffective for spin polarization or spin detection [62]. This is why the spin injection in silicon by optical means is a challenge. One of the straight forward methods of spin injection is rather by electrical means from a ferromagnetic electrode. An early exploration on spin injection through a ferromagnet/paramagnet interface and spin accumulation in a paramagnet was made by Johnson and Silsbee [90, 91, 92]. There is also some theoretical understanding regarding the transport of spin in silicon [93, 94]. However, due to a fundamental conductivity mismatch [95, 96, 97, 98] between a ferromagnetic metal contact and the semiconductor, the realization of the injection of a spin polarized current was not feasible. Even though there is a large spin imbalance between the majority and minority spins in a metal ferromagnet, both channels with up-spin and down-spin are equally populated in a semiconductor due to the relatively small density of states as compared to that for the minority spins in a ferromagnet. On the other hand, because of the comparatively larger resistance of the semiconductor in comparison to the metal, the voltage applied between the ferromagnetic metal and the semiconductor drops completely within the semiconductor. Henceforth, the properties of the contact are dominated by the non-magnetic semiconductor (silicon), and thus resulting in a current injection without spin polarization.

The use of a spin-dependent interface resistance between the ferromagnet and the semiconductor in the form of a tunnel barrier, is supposed to provide a solution to the above described conductivity mismatch problem [96, 97]. In this case, the influx of carriers from the ferromagnet into the semiconductor is reduced to such an extent that the majority spins supply just enough carriers to support the complete occupancy of the corresponding states in the semiconductor. Under such conditions the minority spin flow in semiconductors will be a fraction of that for the majority spins defined by the spin polarization in the ferromagnet. This ensures the existence of a spin polarized current and the spin injection into the semiconductor. However, in order to be able to properly detect the spin signal, the width of the tunnel barrier has to be precisely engineered [99]. Moreover, it drives the challenge to find an appropriate ferromagnetic semiconductor to ensure high quality interfaces without the tunnel barrier. An approach based on the use of hot electrons that do not suffer from the impedance

mismatch problem, has been reported [8]. It was the first demonstration of the electrical spin injection, transport, and detection in undoped silicon at low temperature. The electrical spin injection into silicon from a ferromagnetic contact through an aluminium oxide tunnel barrier at low temperature has also been reported [100]. The vacuum tunneling is reported to preserve the spin-polarization properties of the electrons (92% spin polarized current) in GaAs at a temperature of around 100K [101]. Indeed, the introduction of a tunnel barrier, generally with defects, will cause charge trapping and eventually degrade the performance of the device. The use of ferromagnetic contacts made of semiconductors would be another possible solution. Unfortunately, no semiconductor with ferromagnetic properties at room temperature were known until recently. The existence of diluted magnetic semiconductor nanostructures having a Curie temperature above 400°C provides a promising solution to the problem [102]. Another possibility to avoid the impedance mismatch problem is to employ half-metallic ferromagnets [103]. A half-metallic ferromagnet shows metallic properties with respect to one spin orientation, and acts like an insulator with respect to the other spin orientation. Some Heusler alloys and some transition metal oxides show this property [55]. Along with the above mentioned materials, the spin transport at room temperature in a doped-silicon channel has also been studied [104].

Regardless of the indisputable advantage in realizing the spin injection, detection, and transport in silicon at ambient temperature, several difficulties not explained within the theories are pending. According to the theory as explained in [44], the value of the voltage signal ΔV due to spin accumulation divided by the carrier current density (j) flowing through the injecting contact is proportional to $\frac{\Delta V}{j} = \tilde{P}^2 \rho_S \sqrt{D_c \tau_s}$ with τ_s as the spin lifetime, and D_c as the diffusion coefficient. Because of the injection and detection, the tunnel spin polarization \tilde{P} enters squared, and the silicon resistivity ρ_S multiplied with the spin diffusion length ($L_i = \sqrt{D_c \tau_s}$) determines the additional area resistance of the contact due to spin accumulation under it. However, there is a several orders of magnitude discrepancy between the signal measured and the above mentioned theoretical value. The reasons for the discrepancies are heavily debated [44, 105, 106]. A spin signal much larger than the expected has been reported in germanium structures as well as for other semiconductors [107, 108, 109, 110]. Using single-layer graphene as the tunnel barrier can circumvent the conductivity mismatch issue, and the amplitude of the signal has been reported to be consistent with the spin accumulation in silicon [111]. An explanation based on the assumption that the resonant tunneling magneto-resistance effect and not the spin accumulation causes the electrically dependent spin signal has been proposed [105, 112]. On the other hand, an evidence that a proper account of space-charge effects at the interface may boost the spin injection signal by an order of magnitude was also presented [113].

In this work the semi-classical model of spin drift-diffusion in silicon is employed, when spin is injected in silicon from a ferromagnetic semiconductor. The effect of interface charge screening on spin injection efficiency is under scrutiny. It is noted that, the spin current increases while injected from a charge-depleted region in the ferromagnet, in comparison to when injected from a charge neutral or even a charge

accumulated region. However, the spin injection efficiency is always limited by the bulk spin polarization of the magnetic material. This necessitates the further investigation of spin diffusion in silicon, when spin is injected through a charge neutral and a space-charge layer. However, in both cases, the spin current density can not be significantly higher than the spin current density at charge neutrality. Thus at a fixed boundary spin polarization, the maximum spin current in the bulk is always determined by its value at the charge neutrality condition - provided the charge current is kept fixed.

1.5 Outline of the Thesis

Following the introduction and the motivation, the structure of the thesis is outlined as follows.

The second chapter provides an introduction to the band structure calculations. The principles of the empirical and the ab-initio approaches are described. Then the $\mathbf{k} \cdot \mathbf{p}$ method and the mechanisms of the spin relaxation in semiconductors are presented. Finally, the fundamental mechanisms of the spin relaxation in semiconductors are explained.

In the third chapter a two-band $\mathbf{k} \cdot \mathbf{p}$ Hamiltonian with shear strain and the intrinsic spin degree of freedom, developed near the X -point of the Brillouin zone, is explained. The subband spin-wave functions and their eigenenergies are calculated. The shear strain inflicted valley splitting is described.

The fourth chapter calculates the surface roughness induced spin relaxation matrix elements. The methods to calculate the spin lifetime due to the surface roughness, acoustic, and optical phonons are elaborated, and the calculated results are explained. The direction sensitive spin relaxation model is also highlighted. The major differences among the spin-flip and momentum scattering mechanisms are also investigated. Furthermore, the influence of the valley splitting in unstrained silicon films is elaborated.

In the fifth chapter a comprehensive study of the spin diffusion in silicon in presence or absence of the electric field, when spin is injected from a ferromagnetic semiconductor, is performed. The spin injecting source is assumed to be charge neutral; accumulated; and depleted. The major differences in the transport behavior are revealed. The spin diffusion in silicon from only a space charge layer is also scrutinized.

The sixth chapter summarizes the work, and describes an outlook for future work.

2 Electronic Band Structure

”As many views, as many ways.”

Ramakrishna Paramahansa

In nano-scaled devices, several quantum effects must be taken into consideration. The peculiarities of subband structures determine the carrier transport, and finally their macroscopic behavior. Electrons in any semiconductor experience the periodic potential of the crystal lattice. This periodic potential causes the formation of energy bands. The electronic band structure of a semiconductor describes the energy states that an electron and a hole are either allowed or forbidden to occupy. The analysis of the subband energies of an electron (E_n , n being the band index) with the presented calculation methods, and their dependence on the wave vector (\mathbf{k}) is thus paramount.

2.1 Band Structure Calculation Methods in Semiconductors

As the study of semiconductor properties are a fundamental part of the solid-state physics research, the investigation of the band structure via computational means are of great importance. Modern methods to calculate the electronic band structure are sophisticated enough to describe the subband behavior of semiconductors. However, commonly used methods demand the implementation of complex algorithms and a huge amount of computational power.

Both the empirical and ab-initio methods are utilized to evaluate the band structure of solids. The empirical methods rely on using a small number of adjustable parameters to obtain a fit to certain known features of the bulk band structure, whereas the ab-initio methods determine the band structure from the first principles and do not need any experimental input. Hence, a first principle approach typically involves heavy amount of computational effort, whereas the empirical methods do not [114].

Methods to calculate the band structure of a solid by using first principles can be divided into several groups. The density functional theory (DFT) is widely used to investigate the electronic structures i.e. principally the ground state of many-body systems, in particular atoms, molecules, and condensed phases [115]. The non-equilibrium Greens function (NEGF) function provides a formalism for the description

of transport phenomena of nanoscale devices [116]. Now-a-days, these are extensively used to study the new materials [114]. The most popular empirical methods are based on either pseudopotential or tight-binding methods. On the other hand, by using the perturbative $\mathbf{k} \cdot \mathbf{p}$ method (also a semi-empirical method) one can obtain analytical expressions for the band dispersion and the effective masses averting heavy numerical analysis [72]. In the following section, several methods and their key properties are described in brief.

2.1.1 Nearly-Free Electron Approximation

In the nearly-free electron approximation, interactions between electrons are completely ignored. This approximation allows the use of Bloch's Theorem, which states that electrons in a periodic potential have wave functions and energies which are periodic in wave vector up to a constant phase shift between neighboring reciprocal lattice vectors [117]

$$\Psi_{n,\mathbf{k}}(\mathbf{r}) = \exp(i\mathbf{k} \cdot \mathbf{r}) \cdot u_{n,\mathbf{k}}(\mathbf{r}), \quad (2.1)$$

where the function $u_{n,\mathbf{k}}(\mathbf{r})$ is periodic over the crystal lattice

$$u_{n,\mathbf{k}}(\mathbf{r}) = u_{n,\mathbf{k}}(\mathbf{r} - \mathbf{R}), \quad (2.2)$$

with \mathbf{R} as the periodicity. These plane wave solutions have an energy of $E(\mathbf{k}) = \frac{\hbar^2 k^2}{2m_e}$ (m_e is the electron rest mass). The electron wave function can be approximated by $u_{n,\mathbf{k}}(\mathbf{r}) = \frac{1}{\sqrt{\Omega_r}}$, where Ω_r is the volume occupied by the electron. This over-simplified method works well in the materials where the lattice constant is low (e.g. alkali metals like Na, K, Al and those have one electron in the primitive cell), and the lattice potential is only a small perturbation to the electron sea.

2.1.2 Tight-Binding Approximation

The tight-binding (TB) method uses the atomic orbitals as basis for the wave functions [118]. The electrons are assumed to be tightly bound to their atoms and they must have limited interaction with states and potentials of surrounding atoms of the solid. The crystal potential is strong. As a result the wave function of the electron will be rather similar to the atomic orbital of the bound atom to which it belongs. Any correction from the initial system Hamiltonian to the atomic potential are assumed small. Therefore, this can be considered as the opposite extreme to the nearly free electron approximation. Generally this method is good at describing the inner electronic shells of the atoms. Although the TB approximation neglects the electron-electron interactions, one can still reproduce accurately the band structure of many solids including metals by using this method.

The wave function is constructed from the valence orbitals of all of the atoms in a primitive cell of the crystal. Thus, the single electron wave function can be represented as a linear combination of the atomic orbitals

$$\Psi_{\mathbf{k}}(\mathbf{r}) = \sum_m \sum_{\zeta} \exp(i\mathbf{k} \cdot \mathbf{T}_m) c_{\zeta}(\mathbf{k}) \varphi_{\zeta}(\mathbf{r} - \mathbf{T}_m). \quad (2.3)$$

Here, the atoms are characterized by the atomic orbitals $\varphi_{\zeta}(\mathbf{r})$ (ζ refers to the atomic energy level). This atomic orbital is the eigenfunctions of the Hamiltonian of a single isolated atom. \mathbf{T}_m specifies the position of the m^{th} atom, and the function $\varphi_{\zeta}(\mathbf{r} - \mathbf{T}_m)$ represents the atomic orbital centered around the m^{th} atom. The coefficients $c_{\zeta}(\mathbf{k})$ are found from the Schrödinger equation. It can be shown that $\Psi_{\mathbf{k}}(\mathbf{r})$ in Equation 2.3 is a Bloch function which satisfies the necessary requirement,

$$\Psi_{\mathbf{k}}(\mathbf{r} + \mathbf{T}) = \exp(i\mathbf{k} \cdot \mathbf{T}) \Psi_{\mathbf{k}}(\mathbf{r}), \quad (2.4)$$

where T is the real space crystal translation vector. Now by substituting this equation into the Schrödinger equation, one can form a set of linear equations with respect to the coefficient $c_{\zeta}(\mathbf{k})$. The number of equations is equal to the number of considered orbitals in an atom, thus the solution represents the respective energy bands. The function $\Psi_{\mathbf{k}}(\mathbf{r})$ therefore satisfies both the requirement of the Bloch theorem and the assumptions in the TB model. It can be used to calculate the energy of a band via $E(\mathbf{k}) = \langle \Psi_{\mathbf{k}} | H | \Psi_{\mathbf{k}} \rangle$ [118], where H is the Hamiltonian of the electron.

Several semi-empirical TB models are available in literature depending on different number of orbitals and order of neighbors included [119, 120, 121, 122, 123]. This method can also be easily adapted to strained nanostructures [123].

2.1.3 Cellular Method

The cellular method was the earliest method employed in the band structure calculations by Wigner and Seitz (WS) [124]. In this method, one divides the crystal into several unit cells (WS cell), and each atom is supposed to center at the middle of its cell. The electron, when in a particular cell, is assumed to be only influenced by the ionic potential in that cell. In order to ensure that the function $\Psi_{\mathbf{k}}$ satisfies the Bloch form as described earlier, $u_{\mathbf{k}}$ is periodic, i.e. it is same on the opposite faces of the cell under inspection. Since a WS cell usually has a complicated structure, the use of boundary conditions in a direct way is almost impossible. To avoid this difficulty, only the simplest approximation can be applied: the cell is replaced by a WS sphere with the same volume as the WS cell. This simplifies the problem to such an extent that a solution is possible, although such an approximation can only describe s -type states.

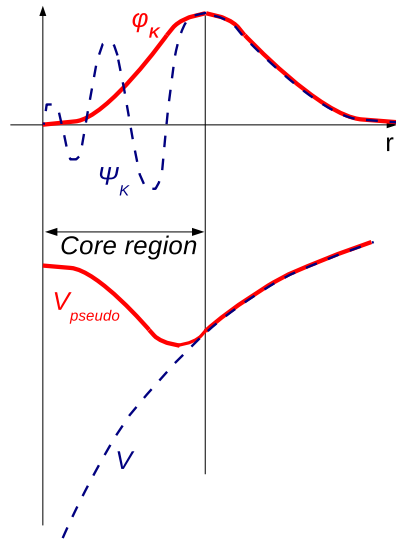


Figure 2.1: Schematic plot of a pseudopotential and the pseudo-wave function in the real space (red), compared to the original ones (blue), is shown.

2.1.4 Augmented-Plane Wave Method

The augmented-plane wave method was developed by Slater in 1937 [125]. APW begins with the assumption that the effective crystal potential is constant between the cores (muffin-tin like potential). Outside the core the wave function is a plane wave as the potential is constant, and inside the core the function is atom-like to be solved by the free-atom Schrödinger equation.

2.1.5 Pseudopotential Method

The pseudo-potential method differs from the above discussed methods by the manner in which the wave function is chosen [126]. The function which oscillates rapidly inside the core, but runs smoothly as a plane wave in the remainder of the open space of the WS cell, is sought for. This phenomenon is drawn in Figure 2.1.

One can write the expression for the wave function [127],

$$\Psi_{\mathbf{k}} = \varphi_{\mathbf{k}} - \sum_{\zeta} c_{\zeta} \varphi_{\zeta}. \quad (2.5)$$

where $\varphi_{\mathbf{k}}$ is a plane-wave like wave function (same as for the APW method), and φ_{ζ} is an atomic wave function. In silicon which has an atomic number of fourteen ($1s^2 2s^2 2p^6 3s^2 3p^2$), the summation over ζ in Equation 2.5 is a sum over the core states $1s^2 2s^2 2p^6$ (i.e. all the occupied atomic shells). $\varphi_{\mathbf{k}}$ is the wave function of any of

the outer core electrons, and φ_ζ are the core wave functions. The coefficients c_ζ are chosen such that the function $\Psi_{\mathbf{k}}$ is orthogonal to the core wave function φ_ζ . By this orthogonality requirement, one can ensure that the outer electrons do not occupy the already filled atomic orbitals. Thus one can avoid violating the Pauli exclusion principle. The formulation of the Schrödinger equation with the pseudo-wave functions can be written as [127]

$$\left(-\frac{\hbar^2}{2m}\nabla^2 + V_{pseudo} \right) \varphi_{\mathbf{k}}(\mathbf{r}) = E\varphi_{\mathbf{k}}(\mathbf{r}). \quad (2.6)$$

Here, V_{pseudo} represents the pseudo-potential which cancels the crystal potential near the core region. The empirical pseudopotential method allows to reproduce all the characteristics including the band gap, spin-orbit split-off, the effective masses, the non-parabolicity parameters etc [72].

2.1.6 Perturbation Theory

Perturbation theory is widely used in mathematics to find an approximate solution to a problem, by starting from a known solution at a known position [72]. This theory is applicable when the problem can be formulated by adding a rather small term to the mathematical description of the exactly solvable problem. Thus, one can start with a system Hamiltonian associated with a known solution and then add an additional 'perturbing' Hamiltonian which imposes a weak disturbance to the known system. On the other hand, one can divide the Hamiltonian representing the quantum state of a system into one bigger and one smaller part and apply the perturbation theory to deduce the approximated solution.

The $\mathbf{k} \cdot \mathbf{p}$ method is based on the perturbative approach and allows to obtain the analytical band structure close to a chosen point provided the eigenenergies and the eigenfunctions at that point are known. The expressions for the band dispersion and also the effective masses can be obtained by using this method [86, 128]. While the $\mathbf{k} \cdot \mathbf{p}$ theory has been frequently used to model the valence band of semiconductors, it can also be applied to model the impact of strain on the conduction band minimum [72]. One can write the one-electron Schrödinger equation as,

$$H_{\mathbf{k}}\Psi_{n,\mathbf{k}}(\mathbf{r}) = E_{n,\mathbf{k}}\Psi_{n,\mathbf{k}}(\mathbf{r}), \quad (2.7)$$

where $H_{\mathbf{k}}$ is the system Hamiltonian

$$H_{\mathbf{k}} = \frac{p^2}{2m_e} + V(\mathbf{r}), \quad (2.8)$$

with n is the band index, \mathbf{k} is the wave vector, m_e is the free electron mass, V is the potential energy, \mathbf{p} is the electron momentum operator ($\mathbf{p} = -i\hbar\nabla$ with \hbar as the reduced Planck constant), $E_{n,\mathbf{k}}$ corresponds to the eigenenergy of the electron wave

function $\Psi_{n,\mathbf{k}}$. Due to the periodicity of the lattice potential, the Bloch theorem can be applied and the solution is of the form of $\Psi_{n,\mathbf{k}} = \exp(i\mathbf{k}\cdot\mathbf{r})u_{n,\mathbf{k}}$.

If one now applies the Bloch wave function ansatz,

$$\mathbf{p}(\Psi_{n,\mathbf{k}}) = \mathbf{p}(\exp(i\mathbf{k}\cdot\mathbf{r})u_{n,\mathbf{k}}) = (\hbar\mathbf{k} + \mathbf{p})(\exp(i\mathbf{k}\cdot\mathbf{r})u_{n,\mathbf{k}}). \quad (2.9)$$

Again,

$$p^2\Psi_{n,\mathbf{k}} = \mathbf{p} \cdot \mathbf{p}(\Psi_{n,\mathbf{k}}) = (\hbar^2k^2 + 2\hbar(\mathbf{k} \cdot \mathbf{p}) + p^2)(\exp(i\mathbf{k}\cdot\mathbf{r})u_{n,\mathbf{k}}). \quad (2.10)$$

From these two identities, Equation 2.7 and Equation 2.8 involving the periodic function $u_{n,\mathbf{k}}$ rather than $\Psi_{n,\mathbf{k}}$ can be rewritten as

$$H'_{\mathbf{k}} = \frac{\hbar^2k^2}{2m_e} + \frac{2\hbar(\mathbf{k} \cdot \mathbf{p})}{2m_e} + \frac{p^2}{2m_e} + V, \quad (2.11a)$$

$$H'_{\mathbf{k}}u_{n,\mathbf{k}} = E_{n,\mathbf{k}}u_{n,\mathbf{k}}. \quad (2.11b)$$

In any case, one can write this Hamiltonian as the sum of two terms $H'_{\mathbf{k}} = H'_{\mathbf{k}\mathbf{0}} + H''_{\mathbf{k}}$, where

$$H'_{\mathbf{k}\mathbf{0}} = \frac{p^2}{2m_e} + V, \quad (2.12a)$$

$$H''_{\mathbf{k}} = \frac{\hbar^2k^2}{2m_e} + \frac{2\hbar(\mathbf{k} \cdot \mathbf{p})}{2m_e}. \quad (2.12b)$$

Hence, the total Hamiltonian $H'_{\mathbf{k}}$ can be divided into an unperturbed part $H'_{\mathbf{k}\mathbf{0}}$ with the eigenfunctions $u_{n,\mathbf{k}\mathbf{0}}$ at $\mathbf{k} = \mathbf{k}\mathbf{0}$, and a perturbative part $H''_{\mathbf{k}}$.

2.1.7 Effective Mass Approximation

The mass of a free electron or the electronic rest mass can be expressed as m_e . When this electron is placed in a crystal lattice the situation changes, and the electron effective mass is the mass that it seems to have when responding to atomic forces. This effective mass must be interpreted as mass of the electron such that the classical energy formula $E = \frac{p^2}{2m}$ holds. Considering the force acting on the electron is \mathbf{F} , the acceleration $\tilde{\mathbf{a}}$ of the electron can be represented as $\tilde{\mathbf{a}} = \frac{\mathbf{F}}{m_e}$. The expression for the velocity is $\mathbf{v} = \frac{dE}{d\mathbf{p}}$ where \mathbf{p} represents the momentum of the electron. Since by definition $\mathbf{F} = \frac{d\mathbf{p}}{dt}$, $\tilde{\mathbf{a}} = \frac{d\mathbf{v}}{dt} = \left(\frac{\partial\mathbf{v}}{\partial\mathbf{p}}\right)\left(\frac{\partial\mathbf{p}}{\partial t}\right) = \left(\frac{\partial^2 E}{\partial\mathbf{p}^2}\right)\mathbf{F}$. By generalizing this equation for a three-dimensional model, one can write [129]

$$\tilde{a}_x = \frac{\partial^2 E}{\partial p_x^2} F_x + \frac{\partial^2 E}{\partial p_x \partial p_y} F_y + \frac{\partial^2 E}{\partial p_x \partial p_z} F_z, \quad (2.13a)$$

$$\tilde{a}_y = \frac{\partial^2 E}{\partial p_x \partial p_y} F_x + \frac{\partial^2 E}{\partial p_y^2} F_y + \frac{\partial^2 E}{\partial p_y \partial p_z} F_z, \quad (2.13b)$$

$$\tilde{a}_z = \frac{\partial^2 E}{\partial p_x \partial p_z} F_x + \frac{\partial^2 E}{\partial p_y \partial p_z} F_y + \frac{\partial^2 E}{\partial p_z^2} F_z. \quad (2.13c)$$

The inverse of the position-dependent effective mass tensor \tilde{m} can be expressed as (the momentum operator and the wave vector \mathbf{k} are related by $\mathbf{p} = \hbar\mathbf{k}$)

$$\begin{aligned} \tilde{m}^{-1} &= \frac{1}{\hbar^2} \begin{bmatrix} \frac{\partial^2 E}{\partial k_x^2} & \frac{\partial^2 E}{\partial k_x \partial k_y} & \frac{\partial^2 E}{\partial k_x \partial k_z} \\ \frac{\partial^2 E}{\partial k_x \partial k_y} & \frac{\partial^2 E}{\partial k_y^2} & \frac{\partial^2 E}{\partial k_y \partial k_z} \\ \frac{\partial^2 E}{\partial k_x \partial k_z} & \frac{\partial^2 E}{\partial k_y \partial k_z} & \frac{\partial^2 E}{\partial k_z^2} \end{bmatrix} \\ &= \begin{bmatrix} m_{xx}^{-1} & m_{xy}^{-1} & m_{xz}^{-1} \\ m_{yx}^{-1} & m_{yy}^{-1} & m_{yz}^{-1} \\ m_{zx}^{-1} & m_{zy}^{-1} & m_{zz}^{-1} \end{bmatrix}. \end{aligned} \quad (2.14)$$

The time-independent Schrödinger equation including \tilde{m} is then expressed as [130]

$$\left(-\frac{\hbar^2}{2} \nabla \tilde{m}^{-1} \nabla + V \right) \Psi_{n,\mathbf{k}}(\mathbf{r}) = E \Psi_{n,\mathbf{k}}(\mathbf{r}). \quad (2.15)$$

2.2 Spin-Orbit Coupling

Classically electrons can be thought of a spinning ball of charge, and the correlated angular momentum is called spin. The experiment from [23] confirmed the quantization of the electron spin into two orientations which paved the way of quantum mechanics of spin. Theoretically, a two-state quantum system (e.g. electron spin) is a system which can exist in any quantum superposition of two independent and physically distinguishable states. The actual state of the electron spin can geometrically be represented by any point in the Bloch sphere (Figure 2.2). Through several experiments it has been shown that the electrons' spin can have only two opposing projections on a fixed axis, and hence only two independent measurable states. These two orthonormal eigenstates (basis) are postulated as $|\uparrow\rangle$ and $|\downarrow\rangle$ where,

$$|\uparrow\rangle \rightarrow \begin{bmatrix} 1 \\ 0 \end{bmatrix}, \quad (2.16)$$

$$|\downarrow\rangle \rightarrow \begin{bmatrix} 0 \\ 1 \end{bmatrix}. \quad (2.17)$$

Any quantum state $|\chi\rangle$ represented by a point on the Bloch sphere (defined through the polar Θ and the azimuthal Φ angles) can always be expressed as a superposition of the basis vectors $|\uparrow\rangle$ and $|\downarrow\rangle$, where the coefficient or amount of each basis vector is

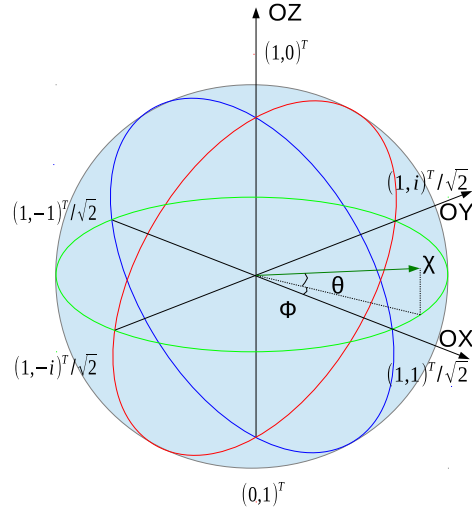


Figure 2.2: Bloch sphere with different qubit states corresponding to the axes is shown. The position of an arbitrary state (χ) can be uniquely represented by the polar (Θ) and the azimuthal angles (Φ).

a complex number. Since only the relative phase between the coefficients of the two basis vectors has any physical meaning, one can take the coefficient of $|\uparrow\rangle$ to be real and non-negative. From postulates of quantum mechanics the total probability of the system has to be one, and thus $\langle\chi|\chi\rangle=1$. Given this constraint, the quantum state $|\chi\rangle$ can be expressed as [131]

$$|\chi\rangle = \cos\left(\frac{\Theta}{2}\right)|\uparrow\rangle + \exp(i\Phi) \cdot \sin\left(\frac{\Theta}{2}\right)|\downarrow\rangle. \quad (2.18)$$

where $0 \leq \Theta \leq \pi$ and $0 \leq \Phi < 2\pi$.

The interaction of the electron spin with the electric field (via the associated magnetic field in the electrons rest frame) and hence the electron's motion in a crystal is called the spin-orbit interaction. This can be represented by the Hamiltonian [128],

$$H_{SO} = \frac{\hbar}{4m_e^2c^2}[\nabla V \times \mathbf{p}] \cdot \boldsymbol{\sigma}. \quad (2.19)$$

Here, c is the speed of light at vacuum, m_e is the electron rest mass, V is the periodic potential, and $\boldsymbol{\sigma} = (\sigma_x, \sigma_y, \sigma_z)$ is the spin vector in the Pauli matrices basis.

The $\mathbf{k} \cdot \mathbf{p}$ Method with Spin-Orbit Coupling

In order to include the spin-orbit coupling, one has to add Equation 2.19 to Equation 2.8 to obtain

$$H_{\mathbf{k}} = \frac{p^2}{2m_e} + V + \frac{\hbar}{4m_e^2c^2}[\nabla V \times \mathbf{p}] \cdot \boldsymbol{\sigma}. \quad (2.20)$$

Analog to the derivation shown in the section 2.1.6, one has to apply a Bloch ansatz to the Schrödinger equation with the modified Hamiltonian from Equation 2.20 [132] to derive the equation for the $\mathbf{k} \cdot \mathbf{p}$ method analysis.

$$H'_{\mathbf{k}} = \frac{p^2}{2m_e} + V + \frac{\hbar^2 k^2}{2m_e} + \frac{2\hbar \mathbf{k} \cdot \mathbf{p}}{2m_e} + \frac{\hbar}{4m_e^2c^2}(\boldsymbol{\sigma} \times \nabla V) \cdot (\hbar \mathbf{k} + \mathbf{p}), \quad (2.21a)$$

$$H'_{\mathbf{k}} u_{n,\mathbf{k}} = E_{n,\mathbf{k}} u_{n,\mathbf{k}}. \quad (2.21b)$$

With the notation

$$\boldsymbol{\Pi} = \mathbf{p} + \frac{\hbar}{4m_e c^2}(\boldsymbol{\sigma} \times \nabla V), \quad (2.22)$$

the above equation turns out to be

$$H'_{\mathbf{k}} = H_{\mathbf{k}} + \frac{\hbar^2 k^2}{2m_e} + \frac{\hbar}{m_e}(\mathbf{k} \cdot \boldsymbol{\Pi}). \quad (2.23)$$

2.3 Spin Relaxation in Semiconductors

The mechanisms of decay for a spin polarized population can be broadly classified as spin-flip scattering (spin relaxation or spin-lattice relaxation) and spin dephasing (or spin decoherence) [131]. The different mechanisms responsible for the spin relaxation time is now discussed [131].

- Elliot-Yafet (EY) mechanism, for elemental metals and semiconductors (c.f. Figure 2.3).
- D'yakonov-Perel' (DP) mechanism, for semiconductors without center of inversion symmetry (c.f. Figure 2.3).
- Bir-Aronov-Pikus mechanism, for heavily p-doped semiconductors.
- Hyperfine interaction, for electrons bound on impurity sites or confined in a quantum dot.

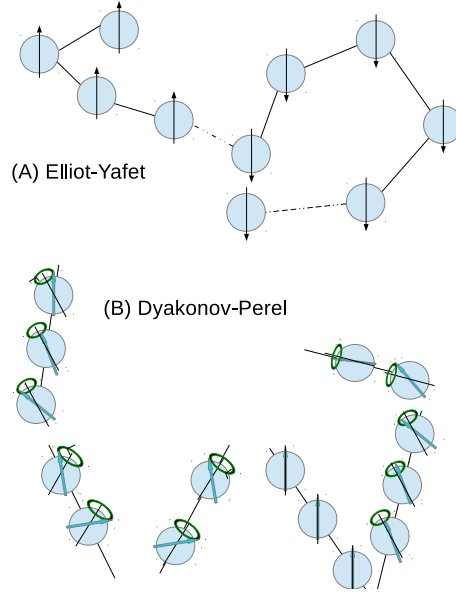


Figure 2.3: Schematic of the Elliot-Yafet and D'yakonov-Perel' spin relaxation mechanisms.

The EY mechanism is important for small gap semiconductors with large spin-orbit splitting [133]. In electronic band structures the up-spin and the down-spin states are mixed by the spin-orbit interaction [63], which means the up(down)-spin state contains the down(up)-spin state. The degenerate Bloch states corresponding to the lattice wave vector \mathbf{k} in the presence of the spin-orbit coupling can be expressed as [131]:

$$\Psi_{\mathbf{k},n,\uparrow}(\mathbf{r}) = (a_{\mathbf{k},n}(\mathbf{r}) |\uparrow\rangle + b_{\mathbf{k},n}(\mathbf{r}) |\downarrow\rangle) \cdot \exp(i\mathbf{k}\mathbf{r}), \quad (2.24a)$$

$$\Psi_{\mathbf{k},n,\downarrow}(\mathbf{r}) = (a_{-\mathbf{k},n}^*(\mathbf{r}) |\downarrow\rangle - b_{-\mathbf{k},n}^*(\mathbf{r}) |\uparrow\rangle) \cdot \exp(i\mathbf{k}\mathbf{r}). \quad (2.24b)$$

Here, n signifies the band index. As spin mixing is usually quite small, one can write $|b_{k,n}| \ll |a_{k,n}|$. In the presence of such mixing spin relaxation events can be caused by any spin-independent scattering, and in the absence of scattering events the spin state remains conserved. This process is called the Elliott process. However, the momentum scattering time is generally of the order of picoseconds and the spin relaxation time several nanoseconds. The Yafet process is due to a spin-orbit interaction in which the spin-orbit coupling of the conduction electrons to the lattice potential can be modulated by lattice vibrations. This leads to an interaction in which the spin of the electron is coupled to the quantum of the lattice vibrations (phonon). Nevertheless when the EY is the dominant scattering mechanism, a direct proportionality correlation between the momentum scattering time and the spin relaxation time can be found [63, 134].

The DP mechanism arises from the effective magnetic fields. This effective field arise from systems that lack inversion symmetry, and are classified as two types, Dressel-

haus [135] and Bychkov-Rashba [136]. In the DP mechanism, the spin of moving electrons precesses due to the effective magnetic field until a scattering occurs and after a scattering event the precession angle changes. One of the major distinguishing features is that in contrary to the EY mechanism, the spin scattering rate is inversely proportional to the momentum scattering rate. There has been work on a unified theory of spin relaxation including both EY and DP dominated scattering [137]. Nevertheless, there has been promising experimental evidence that at room and elevated temperatures, the EY relaxation mechanism is the most important in silicon [67, 138].

3 $\mathbf{k} \cdot \mathbf{p}$ Hamiltonian and Subband Wave Functions

”Arise! Awake! and stop not until the goal is reached.”

Swami Vivekananda

In this chapter the effect of the shear strain ε_{xy} on the relaxed silicon band structure is explained, and then the effective $\mathbf{k} \cdot \mathbf{p}$ Hamiltonian with ε_{xy} and properly included spin-orbit interaction is introduced. The wave functions and the valley splitting are investigated.

3.1 Silicon Lattice

The Miller indices, denoted as h , k , and l , are a symbolic vector representation for the orientation of atomic planes and directions in a crystal lattice. Defining three lattice vectors forming the lattice axes, any crystal plane would intersect the axes at three distinct points. The Miller indices are obtained by taking the reciprocal of the intercepted values. By convention, negative indices are written with a bar over the indices. The adopted nomenclature is as described below [139].

- A direction is represented by $[hkl]$,
- the equivalent directions are denoted by $\langle hkl \rangle$,
- a plane with the normal vector $[hkl]$ is represented by (hkl) , and
- the equivalent planes are denoted by $\{hkl\}$.

The crystal structure of silicon is classified under the diamond structure [139], and thus has two atoms in a primitive cell. Germanium, and carbon are further examples of a diamond structure lattice. On the contrary, the III-V semiconductors (GaAs, AlAs, InAs, InP etc.) are of zinc blende type. The crystal lattice of silicon can be represented as two penetrating face centered cubic lattices (fcc) with the cube side $a=0.543\text{nm}$ as portrayed in Figure 3.1. The structure is visualized as a tetrahedron with four vertices of the first fcc lattice at $(0,0,0)$, $(a/2,0,0)$, $(0,a/2,0)$ and $(0,0,a/2)$ and an additional atom added to the center of this tetrahedron. The additional atom is displaced by

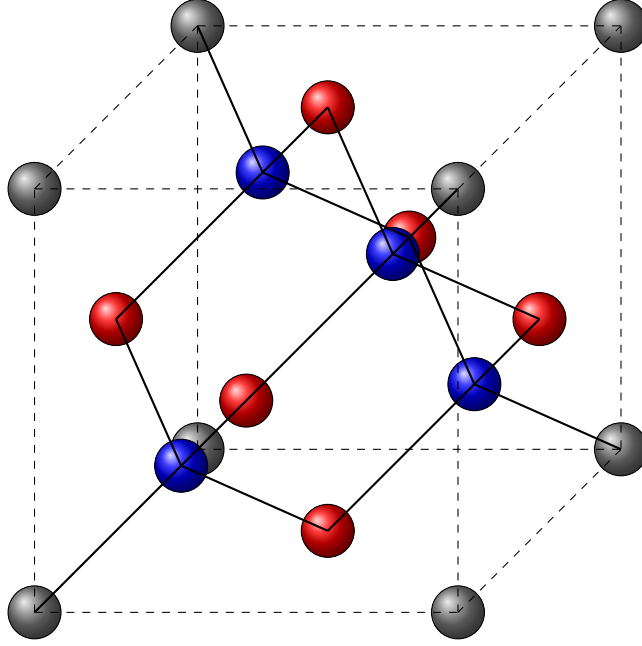


Figure 3.1: Sketch of the diamond crystal lattice is portrayed. Colors gray and red represent A' atoms and color blue represents A'' atoms. For silicon, both atoms are identical.

$a(\frac{1}{4}, \frac{1}{4}, \frac{1}{4})$ with respect to the original fcc lattice. One unit cell of silicon consists of eight atoms, where their distribution with reference to Figure 3.1 is described as below.

- Each of the eight atoms (A' , pertaining to the first fcc lattice) on the corners are shared among each cell, thus counting equivalent one atom inside the cell (gray colored),
- each of the six atoms (A') on the faces are shared among two cells, thus counting three more atoms inside the shell (red colored), and
- four atoms (A'' , pertaining to the second fcc lattice) rest completely inside the cell (blue colored).

3.2 Effect of Strain on Silicon Band Structure

3.2.1 Unstrained Silicon

The first Brillouin zone is defined as the primitive cell in the reciprocal lattice. In silicon, the first Brillouin zone has a shape of a truncated octahedron (c.f. Figure 3.2), and is characterized by eight hexagonal faces and six square faces. The conduction band (CB) edge is located near the zone boundary X points along the Δ symmetry

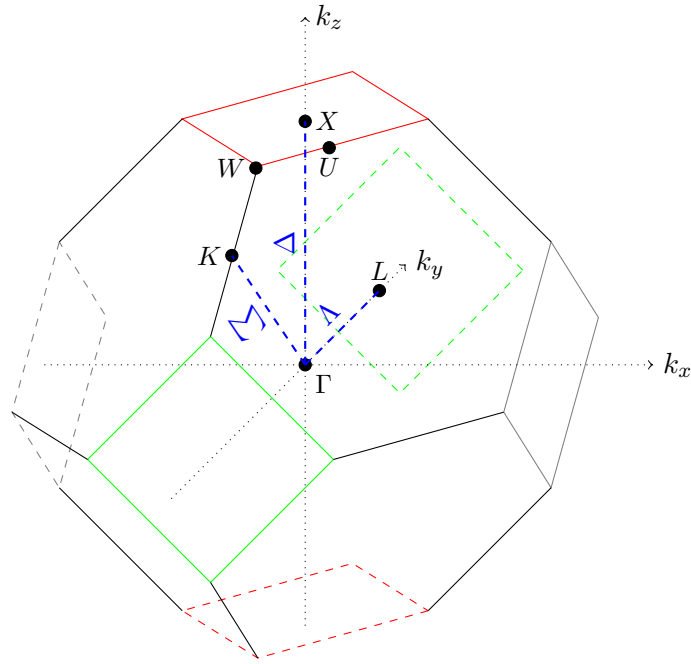


Figure 3.2: The first Brillouin zone of the relaxed silicon lattice is shown. The valley positions and high symmetry points are shown as well.

Directions	Coordinate	Remark
Γ	(0,0,0)	Center of the Brillouin zone (\mathbf{k} space origin)
X	(0,0,1)	Middle of square faces
L	$(\frac{1}{2}, -\frac{1}{2}, \frac{1}{2})$	Middle of hexagonal faces
K	$(0, -\frac{3}{4}, \frac{3}{4})$	Middle of edge shared by two hexagons
U	$(\frac{1}{4}, -\frac{1}{4}, 1)$	Middle of edge shared by a hexagons and a square
W	$(0, -\frac{1}{2}, 1)$	Middle of edge shared by two hexagons and a square
Δ		Directed from Γ to X
Λ		Directed from Γ to L
Σ		Directed from Γ to K

Table 3.1: The symmetry points of the first Brillouin zone in silicon are listed according to Figure 3.2 are listed.

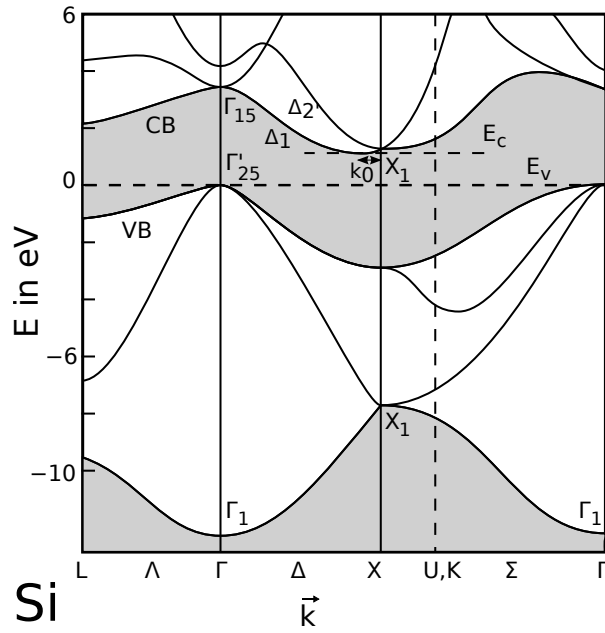


Figure 3.3: The silicon band structure calculated by the pseudopotential method (CB is the conduction band, and VB is the valence band) is described. The VB edges are located exactly at the Γ -point and the minimum of the lowest CB lies on the symmetry Δ line close to the X -point. The lowest two CBs degenerate exactly at the X -point.

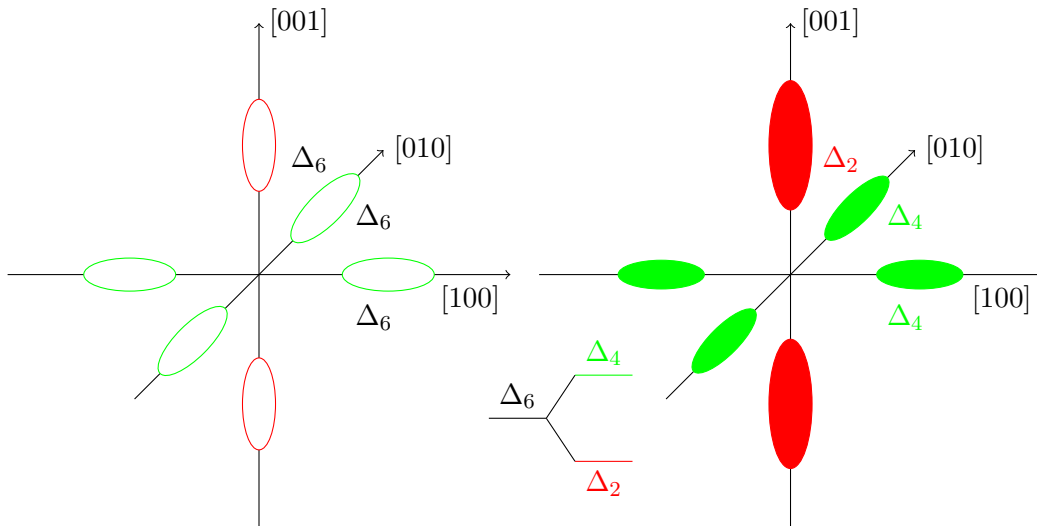


Figure 3.4: Left: constant energy surface of unstrained silicon (six-fold degeneracy) is shown, right: conduction band splitting under shear tensile strain on (001) plane is shown. The red (green) color-fill signifies high (low) electron concentration.

lines. The corresponding symmetry points and directions are tabulated in Table 3.1. The valence bands (VB) contain the last filled energy levels at $T=0\text{K}$, whereas the conduction bands are empty. The band gap E_{gap} separates the CB from the VB. The band structure is usually visualized by plotting $E_n(\mathbf{k})$ along symmetry lines.

The general band structure of unstrained silicon can be sketched as in Figure 3.3. The principal conduction band CB minima are located along the [100], [010], and [001] directions at a distance of about 85% from the Γ -point to the X -points (or equivalently, 15% from the X -point to the Γ -point). The energy of the two lowest CBs are degenerate at the X -points. Close to the CB edge, the band structure can be approximated by constant ellipsoidal energy surfaces (c.f. Figure 3.4 left) and a parabolic energy dispersion [140, 141]. The semi-axes of the ellipse show the direction of the longitudinal m_l and the transversal electron mass m_t . The six-fold degeneracy of the valleys arise due to the symmetry of the lattice along the [100], [010], and [001] directions. The electrons occupy all of these 3 pairs equally, making the transport isotropic.

3.2.2 Strained Silicon

The application of stress modifies the various symmetry properties, causes a change in the band structure, and thus modifies the effective mass which leads to the mobility enhancement [142]. The values of m_l and m_t change under the influence of shear strain [140]. The shear strain also induces a shift in the energy levels of the conduction band and the valence band [72]. This energy shift can be calculated by using the deformation potential theory [72]. The six-fold degenerate Δ_6 valleys in silicon are split into a two-fold degenerate Δ_2 valley pair along [001] direction, and a four-fold degenerate Δ_4 valley pair located along the other two axes. Strain results in lowering (increasing) energy of the Δ_2 (Δ_4) valley pair(s) [72, 143, 141]. Under this condition, the electron population of the Δ_2 (Δ_4) valley pair(s) is increased (decreased), c.f. Figure 3.4.

3.3 Two-Band $\mathbf{k} \cdot \mathbf{p}$ Hamiltonian of [001] Valley at the X-Point

As the lowest two conduction bands Δ_1 and Δ_2' (c.f. Figure 3.3) have their minima just k_0 (c.f. Table 3.2) away from the X -point in the Brillouin zone, a two-band perturbation theory considering only these two bands developed near the X -point describes the band dispersion and subband wave functions very well [72]. The two-band $\mathbf{k} \cdot \mathbf{p}$ Hamiltonian accurately describes the bulk structure up to energies of 0.5-0.8eV [72]. However, this approach is in contrast to [144, 145] where the model has been developed around the Γ -symmetry point which is far away from the conduction band minimum and therefore requires a significant increase in considered bands.

The two-band $\mathbf{k} \cdot \mathbf{p}$ Hamiltonian of a [001] valley in the vicinity of the X -point of the Brillouin zone along the quantization OZ -axis including the shear strain (ε_{xy}) must be of the form [72, 146]

$$H = \begin{bmatrix} \frac{\hbar^2 k_z^2}{2m_l} + \frac{\hbar^2(k_x^2 + k_y^2)}{2m_t} + \frac{\hbar^2 k_0 k_z}{m_l} + \tilde{U}(z) & D\varepsilon_{xy} - \frac{\hbar^2 k_x k_y}{M} \\ D\varepsilon_{xy} - \frac{\hbar^2 k_x k_y}{M} & \frac{\hbar^2 k_z^2}{2m_l} + \frac{\hbar^2(k_x^2 + k_y^2)}{2m_t} - \frac{\hbar^2 k_0 k_z}{m_l} + \tilde{U}(z) \end{bmatrix}, \quad (3.1)$$

where k_i with $i \in x, y, z$ are the projections of the wave vector on the coordinate axes, $\tilde{U}(z)$ is the confinement potential, and ε_{xy} is the shear strain in [110] direction. $\tilde{U}(z)$ arises as the UTB silicon film is supposed to be sandwiched between two oxide layers. The diagonal terms of the (2x2) Hamiltonian correspond to the Hamiltonian of the individual bands, and the off-diagonal term signifies the coupling between those two [72].

Hamiltonian including the Spin Degree of Freedom

The corresponding $\mathbf{k} \cdot \mathbf{p}$ Hamiltonian including the spin degree of freedom considering only the relevant [001] oriented valleys written in the vicinity of the X -point along the OZ -axis in the Brillouin zone can also be derived from Equation 3.1 by introducing the intrinsic spin-orbit term Δ_{SO} [71, 129]. Δ_{SO} couples the states with opposite spin projections to their respective opposite valleys. The basis is conveniently chosen as $[(X_1, \uparrow), (X_1, \downarrow), (X_{2'}, \uparrow), (X_{2'}, \downarrow)]$, where \uparrow and \downarrow indicate the spin projection at the quantization OZ -axis, X_1 and $X_{2'}$ are the basis functions corresponding to the two valleys. Thus, the effective (4x4) Hamiltonian with the spin degree of freedom

Parameter	Value
Silicon lattice constant	$a=0.5431\text{nm}$
Spin-orbit term	$\Delta_{SO}=1.27\text{meVnm}$ [129]
Shear deformation potential	$D=14\text{eV}$
Electron rest mass in silicon	$m_e=9.1093 \cdot 10^{-31}\text{kg}$
Transversal effective mass	$m_t=0.19 \cdot m_e$
Longitudinal effective mass	$m_l=0.91 \cdot m_e$
Valley minimum position from X -point	$k_0=0.15 \cdot \frac{2\pi}{a}$
Valley minimum position from Γ -point	$k_{0\Gamma}=0.85 \cdot \frac{2\pi}{a}$
M^{-1}	$m_t^{-1} - m_e^{-1}$

Table 3.2: The parameter list for the silicon lattice is shown.

reads [129, 147]

$$H = \begin{bmatrix} H_1 & H_3 \\ H_3^\dagger & H_2 \end{bmatrix}, \quad (3.2)$$

where H_1 , H_2 , and H_3 are written as,

$$H_{j=1,2} = \left[\frac{\hbar^2 k_z^2}{2m_l} + \frac{\hbar^2 (k_x^2 + k_y^2)}{2m_t} + \frac{(-1)^j \hbar^2 k_0 k_z}{m_l} + \tilde{U}(z) \right] I \quad (3.3)$$

$$H_3 = \begin{bmatrix} D\varepsilon_{xy} - \frac{\hbar^2 k_x k_y}{M} & (k_y - k_x i) \Delta_{SO} \\ (-k_y - k_x i) \Delta_{SO} & D\varepsilon_{xy} - \frac{\hbar^2 k_x k_y}{M} \end{bmatrix}. \quad (3.4)$$

The spin-orbit field (SOF) acts along $(k_x, -k_y)$ direction. For a zero value of the confinement potential $\tilde{U}(z)$ the energy dispersion of the lowest conduction bands is given by [129]

$$E(k) = \frac{\hbar^2 k_z^2}{2m_l} + \frac{\hbar^2 (k_x^2 + k_y^2)}{2m_t} \pm \sqrt{\left(\frac{\hbar^2 k_z k_0}{m_l} \right)^2 + \delta^2}, \quad (3.5)$$

where

$$\delta = \sqrt{\left(D\varepsilon_{xy} - \frac{\hbar^2 k_x k_y}{M} \right)^2 + \Delta_{SO}^2 (k_x^2 + k_y^2)}. \quad (3.6)$$

The \pm sign signifies the two bands. This expression generalizes the corresponding dispersion relation from [71] by including shear strain.

In order to evaluate the effective spin-orbit interaction Δ_{SO} term one can use the dispersion relation Equation 3.5. If one evaluates the dispersion for $k_x \neq 0$ but $k_y = k_z = 0$, the gap between the lowest two conduction bands can be opened by Δ_{SO} alone in an unstrained sample. The band splitting along the OX -axis is then equal to $2|\Delta_{SO} k_x|$ and thus linearly related to k_x . This splitting can also be evaluated numerically by the empirical pseudopotential method, and thereby one can obtain the value for Δ_{SO} using the linear fitting technique as described in [129]. Δ_{SO} is reported to be 1.27meVnm.

3.4 Wave Functions: Analytical Form

As Δ_{SO} couples two opposite spin projections on two different valleys, one has to use the unitary transformation as described below in order to decouple the spins with opposite direction in those valleys. The four-component wave functions in the two-valley two spin projection basis can thus be straightforwardly obtained as described in [72, 148].

The four basis functions $X_{1\uparrow}$, $X_{1\downarrow}$, $X_{2'\uparrow}$, and $X_{2'\downarrow}$ for the two [001] valleys with spin up, spin down are transformed according to the steps in [129]. After these transformations, the spin quantization is oriented along the axis of the spin-orbit field. One assumes

$$k_{xy} = \sqrt{k_x^2 + k_y^2}. \quad (3.7)$$

$$\psi_1 = \frac{1}{2} \left[(X_{1\uparrow} + X_{2'\uparrow}) + (X_{1\downarrow} + X_{2'\downarrow}) \cdot \frac{k_x - ik_y}{k_{xy}} \right], \quad (3.8a)$$

$$\psi_2 = \frac{1}{2} \left[(X_{1\uparrow} + X_{2'\uparrow}) - (X_{1\downarrow} + X_{2'\downarrow}) \cdot \frac{k_x - ik_y}{k_{xy}} \right], \quad (3.8b)$$

$$\psi_3 = \frac{1}{2} \left[(X_{1\uparrow} - X_{2'\uparrow}) + (X_{1\downarrow} - X_{2'\downarrow}) \cdot \frac{k_x - ik_y}{k_{xy}} \right], \quad (3.8c)$$

$$\psi_4 = \frac{1}{2} \left[(X_{1\uparrow} - X_{2'\uparrow}) - (X_{1\downarrow} - X_{2'\downarrow}) \cdot \frac{k_x - ik_y}{k_{xy}} \right]. \quad (3.8d)$$

$$X_1 = \psi_1 \cos\left(\frac{\gamma}{2}\right) - i\psi_3 \sin\left(\frac{\gamma}{2}\right), \quad (3.9a)$$

$$X_2 = \psi_2 \cos\left(\frac{\gamma}{2}\right) + i\psi_4 \sin\left(\frac{\gamma}{2}\right), \quad (3.9b)$$

$$X_3 = \psi_3 \cos\left(\frac{\gamma}{2}\right) - i\psi_1 \sin\left(\frac{\gamma}{2}\right), \quad (3.9c)$$

$$X_4 = \psi_4 \cos\left(\frac{\gamma}{2}\right) + i\psi_2 \sin\left(\frac{\gamma}{2}\right). \quad (3.9d)$$

Here, X_1 , X_2 , X_3 , and X_4 are the new rotated basis, and the angle γ is given by,

$$\tan(\gamma) = \frac{\Delta_{SO} \cdot k_{xy}}{D\varepsilon_{xy} - \frac{\hbar^2 k_x k_y}{M}}. \quad (3.10)$$

Under these conditions, the new Hamiltonian can be written as

$$H = \begin{bmatrix} H_1 & H_3 \\ H_3 & H_2 \end{bmatrix}, \quad (3.11)$$

with

$$H_{j=1,2} = \left[\frac{\hbar^2 k_z^2}{2m_l} + \frac{\hbar^2 (k_x^2 + k_y^2)}{2m_t} + (-1)^j \delta + \tilde{U}(z) \right] I, \quad (3.12)$$

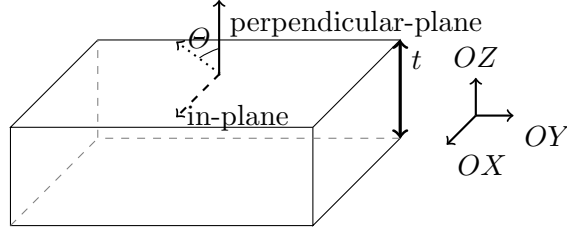


Figure 3.5: Sketch showing the spin injection into a (001) thin silicon film of thickness t in an arbitrary direction, described by the polar angle Θ .

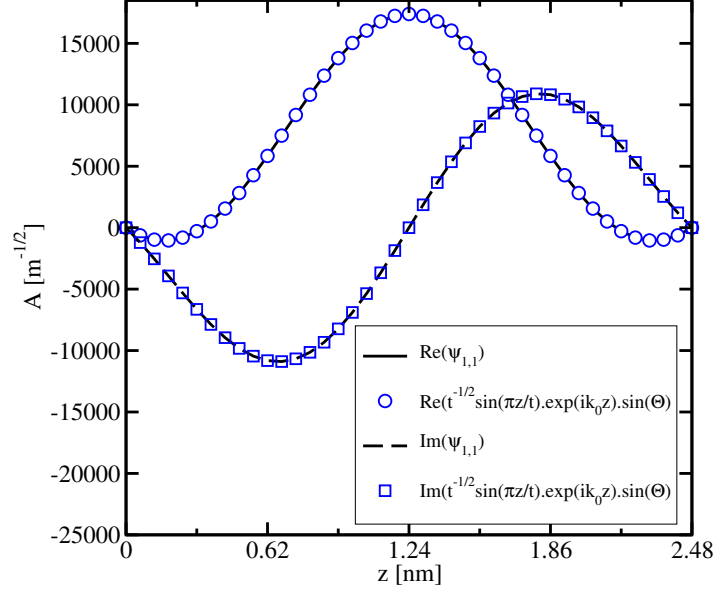


Figure 3.6: The large component of the wave function of the lowest unprimed subband in an unstrained film located in the valley centered at k_0 is shown. $\Theta = \frac{\pi}{3}$ (c.f. Figure 3.5) is maintained.

$$H_3 = \begin{bmatrix} \frac{\hbar^2 k_0 k_z}{m_l} & 0 \\ 0 & \frac{\hbar^2 k_0 k_z}{m_l} \end{bmatrix}. \quad (3.13)$$

The wave functions corresponding to the Hamiltonian Equation 3.11 can be expressed as $\Phi_{1\uparrow}$, $\Phi_{1\downarrow}$, $\Phi_{2\uparrow}$, and $\Phi_{2\downarrow}$.

Wave Functions with Arbitrary Spin Orientation

By considering Θ as the polar angle (c.f. Figure 3.5, and also the azimuthal angle by Φ), a set of linear transformations can be performed to obtain the wave functions $\Psi_{1\uparrow}$,

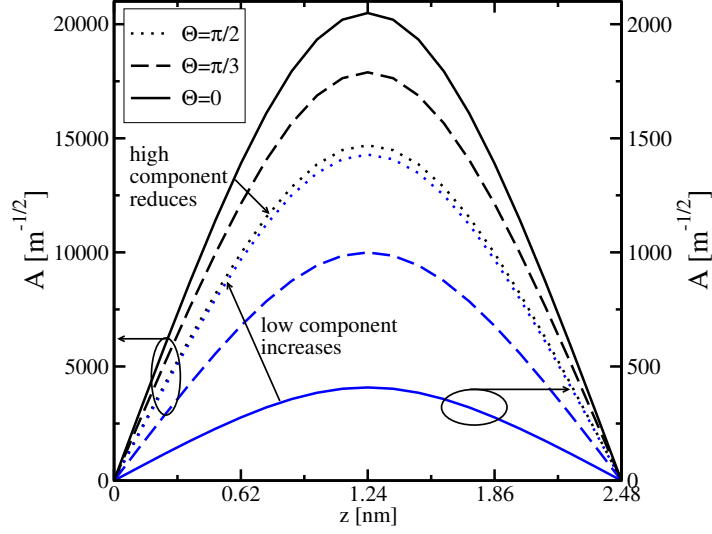


Figure 3.7: The absolute value of the large (small) component of the spin wave functions reduces (increases), when the spin injection changes gradually from OZ - to OX -direction. k_x , k_y , and ε_{xy} are set to be 0.4nm^{-1} , 0.4nm^{-1} , and 0.5% respectively.

$\Psi_{1\downarrow}$, $\Psi_{2\uparrow}$, and $\Psi_{2\downarrow}$ with spin along the injection orientation. This transformation is described below [149].

$$\begin{aligned} \Psi_{n\uparrow} = & \left(\frac{\cos \frac{\Theta}{2}}{\sqrt{2}} + \frac{\sin \frac{\Theta}{2}}{\sqrt{2}} \cdot \exp(-i(\phi_1 - \Phi)) \right) \cdot \Phi_{n\uparrow} \\ & + \left(\frac{\cos \frac{\Theta}{2}}{\sqrt{2}} - \frac{\sin \frac{\Theta}{2}}{\sqrt{2}} \cdot \exp(-i(\phi_1 - \Phi)) \right) \cdot \Phi_{n\downarrow}. \end{aligned} \quad (3.14)$$

$$\begin{aligned} \Psi_{n\downarrow} = & \left(\frac{-\sin \frac{\Theta}{2}}{\sqrt{2}} + \frac{\cos \frac{\Theta}{2}}{\sqrt{2}} \cdot \exp(-i(\phi_1 - \Phi)) \right) \cdot \Phi_{n\uparrow} \\ & + \left(\frac{-\sin \frac{\Theta}{2}}{\sqrt{2}} - \frac{\cos \frac{\Theta}{2}}{\sqrt{2}} \cdot \exp(-i(\phi_1 - \Phi)) \right) \cdot \Phi_{n\downarrow}. \end{aligned} \quad (3.15)$$

Here, $\tan \phi_1 = -\frac{k_y}{k_x}$. Thus, when $\Theta=0$ and the spin is orientated along the OZ -axis and the up(down)-spin wave function in each subband consists of majority and minority components [150] respectively. Their absolute values depend on ε_{xy} . The small components of the wave functions are the result of the Δ_{SO} term [150]. When $k=0$, the up(down)-spin states become eigenstates, which means the small component will be completely absent. Only when $k_x \neq 0$ or $k_y \neq 0$ the small component will be non-vanishing. As depicted in Figure 3.6 and for $\Theta = \frac{\pi}{3}$, the large components of the

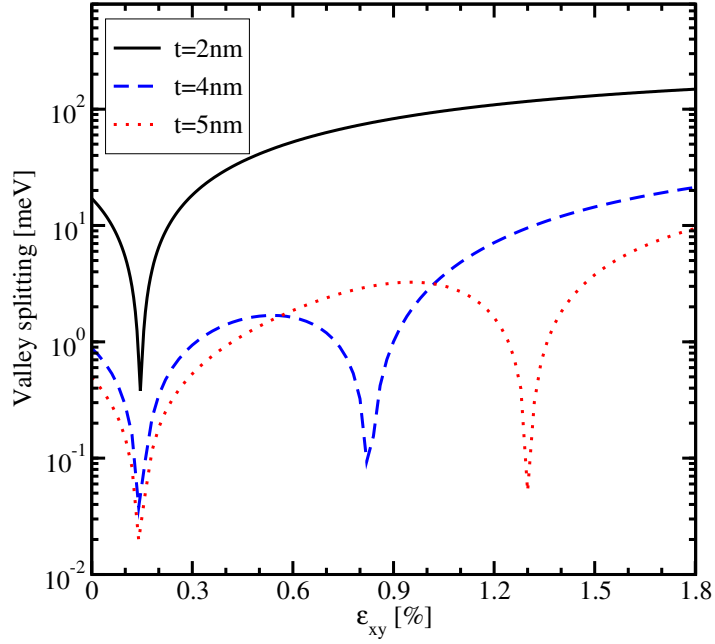


Figure 3.8: Intersubband splitting is shown as a function of shear strain ε_{xy} for different values of the sample thickness t , and for $k_x=0.25\text{nm}^{-1}$ and $k_y=0.25\text{nm}^{-1}$.

four-components' wave functions ($\Psi_{1,1}$) can be described by the envelope quantization function

$$\Psi_{1,1} = \frac{\exp(ik_0z) \sin(\frac{\pi z}{t})}{\sqrt{t}} \cdot \sin(\Theta), \quad (3.16)$$

where t signifies the sample thickness.

The small component is considerably suppressed by the application of the shear strain ε_{xy} [150]. The vanishing values of the small components decrease the spin mixing between the states with opposite spin projections, which causes the increment of the spin lifetime with ε_{xy} . Indeed, the large components of the wave functions do not change significantly with shear strain [150].

The spin injection orientation also has a strong effect on the components of the wave functions. For a fixed in-plane wave vector (k_x, k_y) and at every stress point, the absolute value of the majority (minority) component reduces (increases), when the spin injection direction is changed gradually from perpendicular (OZ -axis) to in-plane (say, OX -axis). This phenomenon is depicted in Figure 3.7, and has an impact on the spin relaxation as will be explained later.

3.5 Valley Splitting by Shear Strain

The presence of the [001] confinement combined with the off-diagonal valley coupling results in the degeneracy lifting of the unprimed subband ladder, leading to the valley splitting [72]. If the potential profile $\tilde{U}(z)$ is approximated by an infinite square well, the expression for the valley splitting can be approximated by [72, 151]

$$\Delta E_C = \frac{2y^2\delta}{k_0t\sqrt{(1-y^2-\eta^2)(1-y^2)}} \left| \sin \left(\sqrt{\frac{1-y^2-\eta^2}{1-y^2}} k_0t \right) \right|, \quad (3.17)$$

where t describes the quantum well thickness, δ is given in Equation 3.6, the parameters y and η are given by

$$y = \frac{\pi}{k_0t}, \quad (3.18)$$

$$\eta = \frac{m_l\delta}{\hbar^2k_0^2}, \quad (3.19)$$

and for the other parameters c.f. Table 3.2.

It is noted that the spin-orbit coupling Δ_{SO} also impacts the valley splitting strength ΔE_C . ΔE_C oscillates with t and is drastically increased by ε_{xy} . The degeneracy between the subbands is exactly recovered, when the sinusoidal oscillating term in Equation 3.17 is zero. However, this degeneracy is not so significant, as it does not add any peculiar behavior to the spin relaxation matrix elements [151]. One has to mention that the analytical expressions for the spin relaxation matrix elements can be found in the following chapters. On the other hand, ΔE_C can be minimized when δ is at its minimum, owing to a very strong spin relaxation as will be described in the following sections.

Figure 3.8 shows the variation of the valley splitting with the shear strain ε_{xy} when the sample thickness t is used as a parameter. The first minimum of the valley splitting is determined by the spin-orbit interaction term alone (i.e. when δ in Equation 3.17 is minimum), and appears to be independent of the quantum well width. The other valley splitting minima (observed for $t=4\text{nm}$ and 5nm in Figure 3.8) depend on the film thickness and are caused by vanishing values of the $\left| \sin \left(\sqrt{\frac{1-y^2-\eta^2}{1-y^2}} k_0t \right) \right|$ term.

4 Spin Relaxation

”Give me blood and I will give you freedom!”

Netaji Subhas C. Bose

Once the subband wave functions are evaluated, one can proceed further to calculate the surface roughness SR induced spin relaxation matrix elements [129]. The UTB silicon films under consideration consist of a very thin conducting layer sandwiched between two oxide layers. Thus, significant parts of the spin transport are carried along the oxide/silicon interfaces and the transport becomes very sensitive to the interface roughness. Therefore, the SR induced scattering plays an important role in UTB films and must be accounted for in spin relaxation calculations.

4.1 Spin Relaxation Matrix Elements

The surface roughness induced spin relaxation matrix elements, normalized to the intrasubband scattering matrix elements at zero strain, are expressed between the wave functions with opposite spin projections [129]

$$M_{s,ij} = \left[\frac{\frac{d\Psi_{i-\sigma}(z)}{dz} \frac{d\Psi_{j\sigma}(z)}{dz}}{\left(\frac{d\Psi_{i\sigma}(z)}{dz} \frac{d\Psi_{i\sigma}(z)}{dz}\right)_{\varepsilon_{xy}=0}} \right]_{z=\pm \frac{t}{2}}, \quad (4.1)$$

where $\sigma=\pm 1$ is the spin projection to the [001] axis.

The up-spin and the down-spin wave functions are orthogonal to each other in every subband which makes the intrasubband relaxation matrix elements zero. The corresponding normalized and squared surface roughness induced intersubband relaxation matrix element ($|M_S|^2$) is depicted in Figure 4.1. One finds that, $|M_S|^2$ is characterized by very sharp peaks when

$$D\varepsilon_{xy} - \frac{\hbar^2 k_x k_y}{M} = 0 \quad (4.2)$$

condition is satisfied, which is also known as the spin hot spots. At this condition, the value of δ in Equation 3.6 attains its minimum. The subband splitting is at its minimum at the spin hot spots, which signifies a maximum mixing between up- and

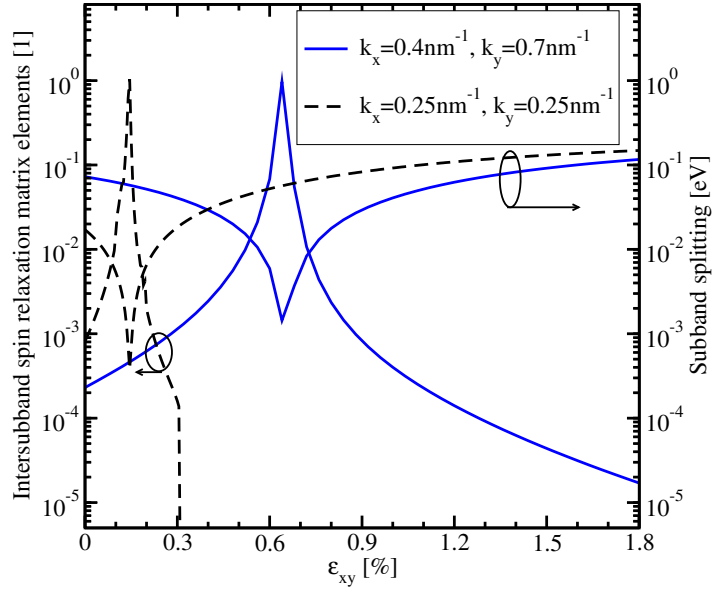


Figure 4.1: The normalized and squared intersubband spin relaxation matrix element ($|M_S|^2$) is shown as function of the shear strain ε_{xy} , and for an arbitrary (k_x, k_y) pair (sample thickness $t=2\text{nm}$). Spin is oriented along OZ -direction ($\Theta=0$, c.f. Figure 3.5). The splitting of the lowest subbands (valley splitting) is also shown.

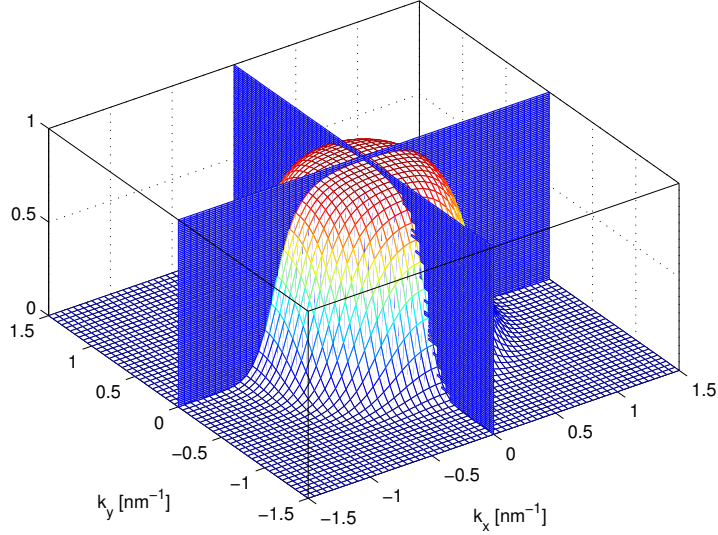


Figure 4.2: The normalized intersubband spin relaxation matrix element (c.f. Equation 4.1) for an unstrained sample is shown, with the Fermi distribution at 300K.

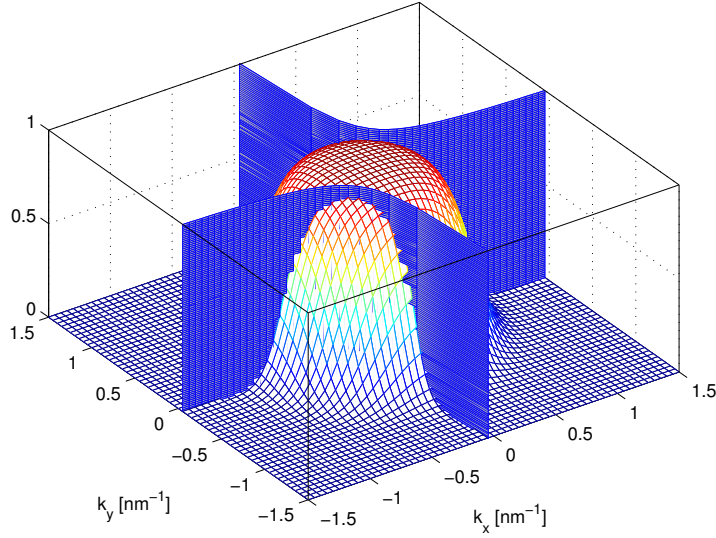


Figure 4.3: The normalized intersubband spin relaxation matrix element for $\varepsilon_{xy}=0.2\%$ is shown, with the Fermi distribution at 300K.

down-spin eigenstates. These hot spots should be contrasted with the spin hot spots appearing in the bulk system along the same directions at the edge of the Brillouin zone [71, 67]. The origin of the hot spots in thin films lies in the unprimed subband degeneracy, which effectively projects the bulk spin hot spots from the edge of the Brillouin zone to the center of the 2D Brillouin zone. As soon as the intersubband splitting becomes larger than the spin-orbit interaction strength, the mixing of states caused by this spin-orbit interaction is reduced, signifying the reduction of spin relaxation.

Figure 4.2 shows $|M_S|^2$ for an unstrained film. The hot spots are along the [100] and [010] directions. Figure 4.3 describes how the shear strain pushes the spin hot spots to the higher energies outside of the states occupied by carriers. This leads to a reduction of the surface roughness induced spin relaxation.

Influence of Arbitrary Spin Orientation

The position of the spin hot spots in the surface roughness induced normalized and squared intersubband relaxation matrix element ($|M_S|^2$) with respect to the kinetic energy of the conducting electrons is shown in Figure 4.4, which again shows that increasing ε_{xy} pushes the scattering peak to higher energy states. It has already been described how the spin injection orientation defined by the angle Θ influences the subband wave functions in the section 3.4. Under the same conditions, $|M_S|^2$ is observed to be decreasing with increasing Θ , reaching its minimum when $\Theta=\frac{\pi}{2}$ (i.e.

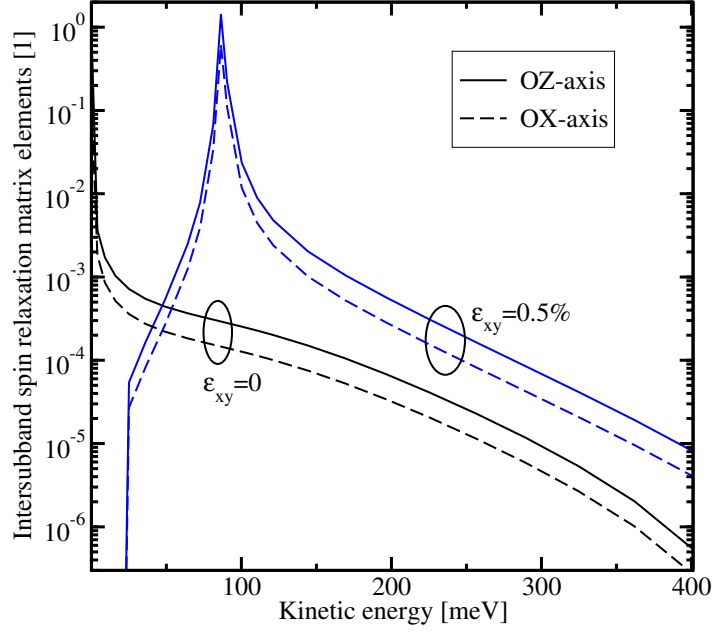


Figure 4.4: The variation of the normalized intersubband spin relaxation matrix elements with the kinetic energy of the conduction electrons in [110] direction is depicted. The influence of the spin injection direction is also shown ($t=1.36\text{nm}$).

when spin is injected along the OX -direction). The dependence of $|M_S|^2$ on Θ and (k_x, k_y) is evaluated to be [149]

$$|M_S|^2 \propto 1 + \left(\frac{k_x}{k_y}\right)^2 \cdot \cos^2 \Theta. \quad (4.3)$$

Then one can proceed further to write,

$$\frac{|M_S|^2(\Theta)}{|M_S|^2(\Theta=0)} = \frac{1 + \left(\frac{k_x}{k_y}\right)^2 \cdot \cos^2 \Theta}{1 + \left(\frac{k_x}{k_y}\right)^2}. \quad (4.4)$$

Rewriting Equation 4.4 with $\tan \phi_1 = -\frac{k_y}{k_x}$ leads to

$$\frac{|M_S|^2(\Theta)}{|M_S|^2(\Theta=0)} = \sin^2 \phi_1 + \cos^2 \phi_1 \cdot \cos^2 \Theta. \quad (4.5)$$

Figure 4.5 describes the variation of $|M_S|^2$ with Θ and $\tan \phi_1 = -\frac{k_y}{k_x}$. $|M_S|^2$ oscillates with respect to ϕ_1 , but steadily decreases when the spin injection orientation is drawn from perpendicular OZ -axis towards in-plane OX axis. This shows that the spin scattering rate must decrease, when the spin injection orientation is drawn gradually towards in-plane.

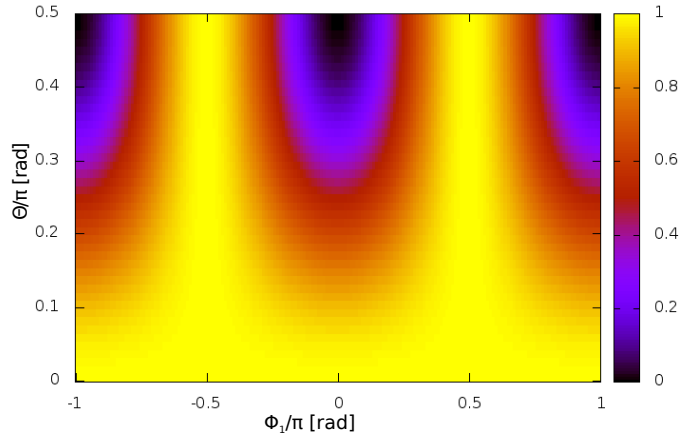


Figure 4.5: The variation of the normalized intersubband spin relaxation matrix elements with Θ (c.f. Figure 3.5) and ϕ_1 (with $\tan(\phi_1) = -\frac{k_y}{k_x}$) is described. The domain for Θ is chosen to be $(0, \frac{\pi}{2})$ as it is repeated in the rest of the domain $(\frac{\pi}{2}, \pi)$.

4.2 Spin Hot Spots and Spin Precession

As the spin hot spot condition is characterized by a strong increase of the mixing of the up- and down-spin states, the equivalent subband splitting at the spin hot spots is purely determined by the effective spin-orbit term, which is in turn linear with $\Delta_{SO}\sqrt{k_x^2 + k_y^2}$, where k_x and k_y are the components of the in-plane electron wave vector. This linear dependence of the splitting is similar to the Zeeman splitting in a magnetic field [152]. Therefore, the spin-orbit interaction term $\Delta_{SO}\tilde{\mathbf{k}}$ with $\tilde{\mathbf{k}}=(k_x, -k_y)$ can be interpreted as an effective magnetic field known as spin-orbit field (SOF), while the pairs of states (X_1, \uparrow) , $(X_{2'}, \downarrow)$ and $(X_{2'}, \uparrow)$, (X_1, \downarrow) it couples have similarities with the Zeeman up- and down-spin states split because of the effective field [152]. It is now obvious that the angle ϕ_1 defined in the section 3.4 represents the direction of the SOF. The spin injection orientation impacts the spin precession at the spin hot spots and some of the related effects are now studied.

4.2.1 Spin Expectation Value

One can estimate the spin expectations which depend on the spin injection orientation. The spin Pauli matrices for the two [001] valleys can be written as,

$$\sigma_x = \begin{bmatrix} 0 & 1 & 0 & 0 \\ 1 & 0 & 0 & 0 \\ 0 & 0 & 0 & 1 \\ 0 & 0 & 1 & 0 \end{bmatrix}, \quad (4.6a)$$

$$\sigma_y = \begin{bmatrix} 0 & -i & 0 & 0 \\ i & 0 & 0 & 0 \\ 0 & 0 & 0 & -i \\ 0 & 0 & i & 0 \end{bmatrix}, \quad (4.6b)$$

$$\sigma_z = \begin{bmatrix} 1 & 0 & 0 & 0 \\ 0 & -1 & 0 & 0 \\ 0 & 0 & 1 & 0 \\ 0 & 0 & 0 & -1 \end{bmatrix}. \quad (4.6c)$$

Now one can express the expectation values of the spin projection on the coordinate axes, denoted as $\langle S_{n,p} \rangle$ ($n=1,2$ and $p \in x, y, z$),

$$\langle S_{n,p} \rangle = \int_0^t \Psi_n^\dagger \sigma_p \Psi_n dz. \quad (4.7)$$

The total spin expectation can be represented as,

$$\langle S_n \rangle = \sqrt{\sum_p \langle S_{n,p} \rangle^2}. \quad (4.8)$$

When spin is injected along OZ -axis ($\Theta=0$), $\langle S_{n,x} \rangle = \langle S_{n,y} \rangle = 0$ but $\langle S_{n,z} \rangle = 1$. It is spotted that at spin hot spots, the $\langle S_{n,z} \rangle$ value also drops to zero. When spin is injected along OX -axis ($\Theta = \frac{\pi}{2}$, $\Phi=0$), $\langle S_{n,y} \rangle = \langle S_{n,z} \rangle = 0$ but $\langle S_{n,x} \rangle = 1$. On the contrary at the spin hot spots [153, 154],

$$\langle S_{n,x} \rangle = \sin^2 \left(\arctan \left(\frac{k_x}{k_y} \right) \right), \quad (4.9a)$$

$$\langle S_{n,y} \rangle = -0.5 \sin \left(2 \arctan \left(\frac{k_x}{k_y} \right) \right), \quad (4.9b)$$

$$\langle S_{n,z} \rangle = 0, \quad (4.9c)$$

thus making $\langle S_n \rangle = \sin \left(\arctan \left(\frac{k_x}{k_y} \right) \right)$. When spin is injected along an arbitrary direction on the XZ -plane, one can obtain at the spin hot spots,

$$\langle S_{n,x} \rangle = \sin^2 \left(\arctan \left(\frac{k_x}{k_y} \right) \right) \cdot \sin \Theta, \quad (4.10a)$$

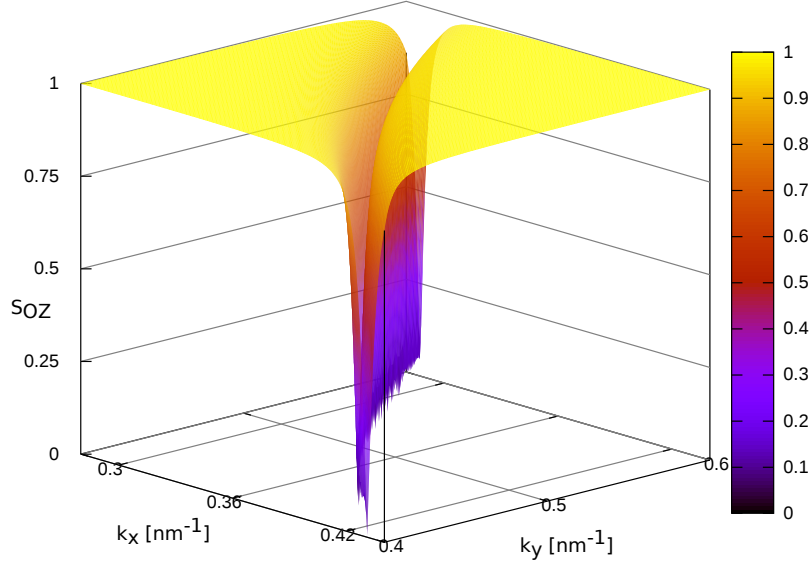


Figure 4.6: The dependence of the total spin expectation (S_{OZ}) over a certain (k_x, k_y) pair is shown, when spin is injected along the OZ -direction ($\varepsilon_{xy}=0.5\%$).

$$\langle S_{n,y} \rangle = -0.5 \sin \left(2 \arctan \left(\frac{k_x}{k_y} \right) \right) \cdot \sin \Theta, \quad (4.10b)$$

$$\langle S_{n,z} \rangle = 0, \quad (4.10c)$$

and hence

$$\langle S_n \rangle = \sin \left(\arctan \left(\frac{k_x}{k_y} \right) \right) \cdot \sin \Theta. \quad (4.11)$$

Figure 4.6 and Figure 4.7 portray the values for $\langle S_n \rangle$ over a range of (k_x, k_y) pairs, when spin is injected along OZ - and OX -directions respectively. The value of $\langle S_n \rangle$ always remains to one, but its value drops to zero when the spin is injected along OZ -direction and when the spin hot spot condition is reached. On the contrary when the spin is injected along OX -direction, $\langle S_n \rangle = \sin \left(\arctan \left(\frac{k_x}{k_y} \right) \right)$ at the spin hot spots. When Θ is increased from zero to the maximum, $\langle S_n \rangle$ gradually increases at the spin hot spots. This indicates that the spin relaxation rate (lifetime) is expected to decrease (increase), when the injection orientation is drawn towards in-plane.

4.2.2 Spin Precession

The effective spin-orbit field SOF is given by $\Delta_{SO} \tilde{\mathbf{k}}$ and lies on the XY -plane along the $(k_x, -k_y)$ direction. The electron spin starts precessing around the SOF when injected along any direction. One can see that (c.f. Figure 4.8), when the spin is injected along OZ -direction, the average spin projection on the OX - and the OY -axes will always

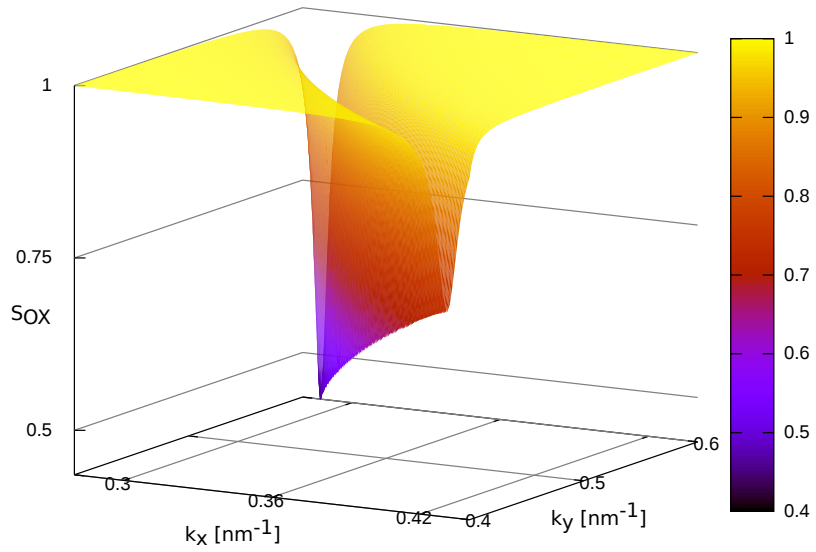


Figure 4.7: The dependence of the total spin expectation (S_{OX}) over a certain (k_x, k_y) pair is shown, when spin is injected along the OX -direction ($\varepsilon_{xy}=0.5\%$).

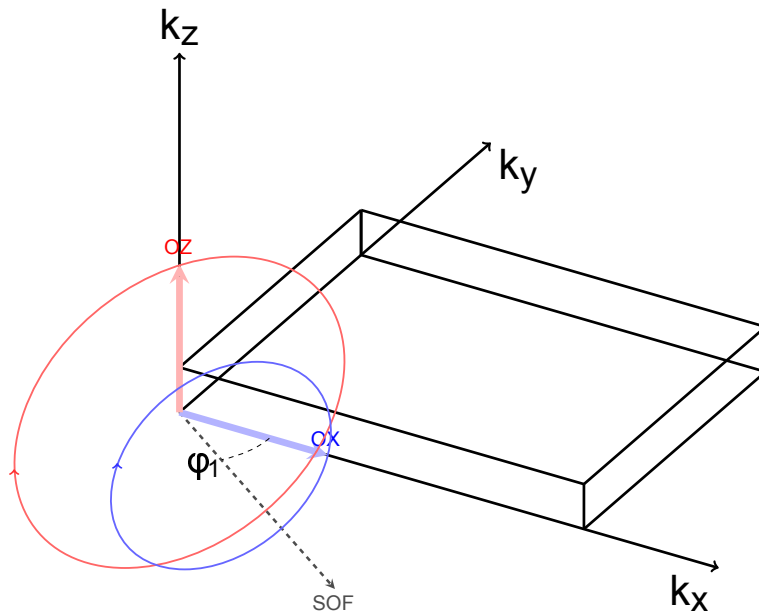


Figure 4.8: The precession of the injected spin (along OX - and OZ -directions) around the existing spin-orbit field (SOF) is portrayed ($\tan \phi_1 = -\frac{k_y}{k_x}$).

be zero. On the contrary when the spin injection is gradually drawn towards the OX -direction, the spin projection value gradually increases. This phenomenon is correlated with the already obtained spin expectation values at the spin hot spots. Because of the zero spin expectation value at any pair of (k_x, k_y) resulting in maximal spin randomization, the spin relaxation rate (time) is predicted to be strongest (weakest) for perpendicular-plane spin injection.

4.3 Calculation of the Spin Relaxation Rates

The spin relaxation times for all the individual components are evaluated by thermal averaging [71, 53, 69] as

$$\frac{1}{\tau_m[\tau_s]} = \frac{\sum_i \int \frac{1}{\tau_i(\mathbf{k}_1)} \cdot f(E)(1 - f(E)) d\mathbf{k}_1}{\sum_i \int f(E) d\mathbf{k}_1}, \quad (4.12)$$

where

$$\int d\mathbf{k}_1 = \int_0^{2\pi} d\varphi \cdot \int_{E_i^{(0)}}^{\infty} \frac{|\mathbf{k}_1|}{\left| \frac{\partial E(\mathbf{k}_1)}{\partial \mathbf{k}_1} \right|_{\mathbf{k}_1}} dE. \quad (4.13)$$

$\mathbf{k}_1(E, \varphi) = (k_1(E, \varphi) \cos(\varphi), k_1(E, \varphi) \sin(\varphi))$ is the in-plane subband wave vector of the electron before scattering. The angle φ defines the \mathbf{k}_1 direction, thus the term $\left| \frac{\partial E(\mathbf{k}_1)}{\partial \mathbf{k}_1} \right|_{\mathbf{k}_1}$ is the derivative of the subband dispersion along \mathbf{k}_1 at the angle φ . The Fermi distribution function is

$$f(E) = \frac{1}{\left[1 + \exp\left(\frac{E - E_F}{K_B T}\right) \right]}. \quad (4.14)$$

Here, K_B is the Boltzmann constant, T is the temperature, E_F is the Fermi level, and E can be expressed as

$$E = E_i^{(0)} + E_i(\mathbf{k}_1), \quad (4.15a)$$

$$E_i^{(0)} = E_i(\mathbf{k}_1 = 0), \quad (4.15b)$$

where $E_i^{(0)}$ is the energy of the bottom of the subband i . When the values of the electron concentration and temperature are provided, E_F is evaluated numerically by following [69]. Nevertheless, when both the surface roughness and the phonon mediated components are calculated, the total spin lifetime is calculated by the Matthiessen rule [117].

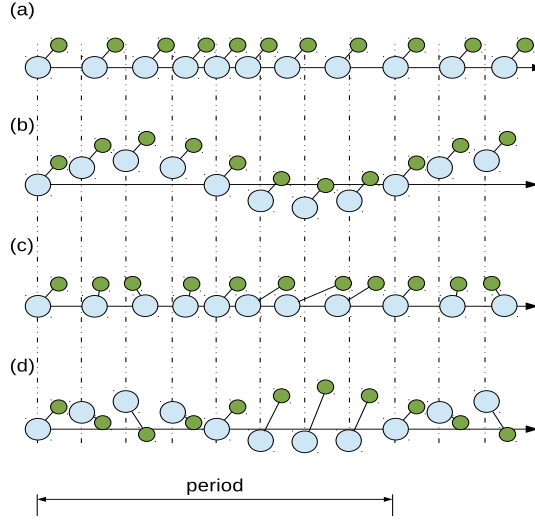


Figure 4.9: The four phonon modes are found in elemental semiconductors: (a) longitudinal acoustic, (b) transversal acoustic, (c) longitudinal optical, and (d) transversal optical modes.

4.3.1 Surface Roughness Limited Spin Relaxation Rates

The spin-flip rate can be written as [55]

$$\begin{aligned}
 \frac{1}{\tau_{i,s,SR}(\mathbf{k}_1)} &= \frac{4\pi}{\hbar(2\pi)^2} \sum_{j=1,2} \int_0^{2\pi} d\varphi \cdot \pi \Delta^2 L^2 \cdot \frac{1}{\epsilon_{ij}^2 |\mathbf{k}_2 - \mathbf{k}_1|} \cdot \frac{\hbar^4}{4m_i^2} \cdot \frac{|\mathbf{k}_2|}{\left| \frac{\partial E(\mathbf{k}_2)}{\partial \mathbf{k}_2} \right|} \\
 &\cdot \left[\left(\frac{d\Psi_{i\mathbf{k}_1\sigma}}{dz} \right)^* \left(\frac{d\Psi_{j\mathbf{k}_2-\sigma}}{dz} \right) \right]_{z=\pm \frac{t}{2}}^2 \cdot \exp\left(\frac{-|\mathbf{k}_2 - \mathbf{k}_1|^2 L^2}{4} \right) \\
 &\cdot \theta(E_j(\mathbf{k}_2) - E_j^{(0)}).
 \end{aligned} \tag{4.16}$$

Here, \mathbf{k}_1 (\mathbf{k}_2) is the in-plane wave vector of the electron before (after) scattering, φ is the angle between \mathbf{k}_1 and \mathbf{k}_2 vectors, $\epsilon_{i,j}$ is the dielectric permittivity, L is the autocorrelation length, and Δ is the mean square value of the SR -fluctuations [129]. $\sigma = \pm 1$ is the spin projection to the $[001]$ axis. $\theta(x)$ is the Heaviside function.

4.3.2 Phonons

Phonons are the lattice vibrations, but those can be imagined as particles which carry vibrational energy in a similar manner to photons, i.e. they are discrete and quan-

tized [117]. The energy of a phonon is characterized by its own intrinsic frequency. In a lattice with a basis of more than one atom in the primitive cell (which may or may not be different), the allowed frequencies of a propagating wave can be split into an upper branch known as the optical branch, and a lower branch called the acoustical branch. Acoustic phonons are coherent movements of atoms of the lattice out of their equilibrium positions. In contrast for optic phonons, the center of mass of the cell during oscillations does not move [117, 128, 155] (i.e. one atom moving to the left, and its neighbour to the right). The nature of the vibrations are sketched in Figure 4.9. The acoustic branch has its name because it gives rise to long wavelength vibrations, and the speed of its propagation is the speed of a sound wave in the lattice. The optical branch is a higher energy vibration, and one can excite these modes with the electromagnetic radiation [117]. For both of acoustic and optical modes, the vibration is restricted to the direction of propagation in the longitudinal mode, whereas in the transversal mode the vibration occurs in the perpendicular planes.

In the three-dimensional lattice system the number of optical modes for the primitive cell that contains p atoms is given by the expression $3(p-1)$, while the number of acoustic modes is always three. Each of the modes has three components: two transversal ($TA1$, $TA2$, $TO1$, $TO2$) and one longitudinal (LA , LO).

In the analysis of intrasubband electron-phonon scattering, the explicit forms of the polarization vectors of phonons are needed. Following [156, 53] the phonons polarization vectors can be written as

$$\varrho_{LA} = \frac{1}{q} \begin{bmatrix} q_x \\ q_y \\ q_z \end{bmatrix}, \quad (4.17)$$

$$\varrho_{TA1} = \frac{1}{\sqrt{q_x^2 + q_y^2}} \begin{bmatrix} q_y \\ -q_x \\ 0 \end{bmatrix}, \quad (4.18)$$

$$\varrho_{TA2} = \frac{1}{q\sqrt{q_x^2 + q_y^2}} \begin{bmatrix} q_x q_z \\ q_y q_z \\ -(q_x^2 + q_y^2) \end{bmatrix}, \quad (4.19)$$

where $q = \sqrt{q_x^2 + q_y^2 + q_z^2}$ is related to the momentum transfer in the scattering [53].

The formulation for the transition rate from one energy eigenstate of a quantum system into the other energy eigenstates in a continuum is given by Fermi's golden rule [157]. The electron-phonon mediated momentum and the spin relaxation rates, where m is the relaxation mechanism signifying contributions from the acoustic and the optical phonon for transitions from band i to band j are calculated by using Fermi's second Golden Rule as described in [53, 157]

$$\frac{1}{\tau_i(k_i)} = \frac{2(4)\pi}{\hbar(2\pi)^2} \int d^2 k_j |M_{m,i,j}(k_i, k_j)|^2 \delta(E_j - E_i + \Delta E_m), \quad (4.20)$$

where M represents the momentum scattering (spin relaxation) matrix element, and the material volume is chosen as the unit volume. The value 4 (2) for spin (momentum) relaxation accounts for the fact that the net number of spin polarized electrons changes by two with each spin flip [53].

4.3.3 Intravalley and g-Intervalley Relaxation Processes Rates

The spin relaxation rate for the wave vector \mathbf{k}_1 in subband i can be written as [69]

$$\begin{aligned}
 \frac{1}{\tau_{i,AC}(\mathbf{k}_1)} &= \frac{4\pi K_B T}{\hbar \rho \nu^2} \sum_j \int_0^{2\pi} \frac{d\varphi}{2\pi} \int_{-\infty}^{\infty} \frac{dq_z}{(2\pi)^2} \frac{|\mathbf{k}_2|}{\left| \frac{\partial E(\mathbf{k}_2)}{\partial \mathbf{k}_2} \right|} \\
 &\cdot \left[1 - \frac{\left| \frac{\partial E(\mathbf{k}_2)}{\partial \mathbf{k}_2} \right| f(E(\mathbf{k}_2))}{\left| \frac{\partial E(\mathbf{k}_1)}{\partial \mathbf{k}_1} \right| f(E(\mathbf{k}_1))} \right] \\
 &\cdot \sum_{\alpha_1 \alpha_2} \left| \frac{q_{\alpha_1}}{q} \varrho_{\alpha_2}(\mathbf{q}) D_{\alpha_1 \alpha_2} \int_0^t dz \Psi_{j\mathbf{k}_2-\sigma}^\dagger(z) \exp(-iq_z z) \Psi_{i\mathbf{k}_1\sigma}(z) \right|^2 \\
 &\cdot \theta(E_j(\mathbf{k}_2) - E_j^{(0)}).
 \end{aligned} \tag{4.21}$$

Here, the momentum transfer vector \mathbf{q} can be realized by $\mathbf{q} = (\mathbf{k}_2 - \mathbf{k}_1, q_z)$, $D_{\alpha_1 \alpha_2}$ is the deformation potential, $(\alpha_1, \alpha_2) = (x, y)$, $\varrho_{\alpha_2}(\mathbf{q}) = (\varrho_{LA}(\mathbf{q}), \varrho_{TA1}(\mathbf{q}), \varrho_{TA2}(\mathbf{q}))$ is the polarization vector.

By applying Fubini's theorem the modulus in the above equation can be replaced by a repeated integral,

$$\begin{aligned}
 \frac{1}{\tau_{i,AC}(\mathbf{k}_1)} &= \frac{4\pi K_B T}{\hbar \rho \nu^2} \sum_j \int_0^{2\pi} \frac{d\varphi}{2\pi} \int_{-\infty}^{\infty} \frac{dq_z}{(2\pi)^2} \frac{|\mathbf{k}_2|}{\left| \frac{\partial E(\mathbf{k}_2)}{\partial \mathbf{k}_2} \right|} \\
 &\cdot \left[1 - \frac{\left| \frac{\partial E(\mathbf{k}_2)}{\partial \mathbf{k}_2} \right| f(E(\mathbf{k}_2))}{\left| \frac{\partial E(\mathbf{k}_1)}{\partial \mathbf{k}_1} \right| f(E(\mathbf{k}_1))} \right] \\
 &\cdot \int_0^t dz \int_0^t dz' \left[\psi_{j\mathbf{k}_2-\sigma}^\dagger(z) M^{AC} \psi_{i\mathbf{k}_1\sigma}(z) \right]^* \\
 &\cdot \left[\psi_{j\mathbf{k}_2-\sigma}^\dagger(z') M^{AC} \psi_{i\mathbf{k}_1\sigma}(z') \right] L_{AC} \exp(-iq_z |z - z'|) \\
 &\cdot \theta(E_j(\mathbf{k}_2) - E_j^{(0)}).
 \end{aligned} \tag{4.22}$$

M^{AC} is the deformation potential matrix, the exact form of the matrix depends on the phonon mode and is shown later. The L_{AC} term depends on the spin-flip process

and the phonon mode [53]. By replacing the order of the integration in Equation 4.22 the acoustic phonon mediated relaxation rate can be written as

$$\begin{aligned}
 \frac{1}{\tau_{i,AC}(\mathbf{k}_1)} &= \frac{4\pi K_B T}{\hbar \rho \nu^2} \sum_j \int_0^{2\pi} \frac{d\varphi}{2\pi} \frac{1}{(2\pi)^2} \frac{|\mathbf{k}_2|}{\left| \frac{\partial E(\mathbf{k}_2)}{\partial \mathbf{k}_2} \right|} \\
 &\cdot \left[1 - \frac{\left| \frac{\partial E(\mathbf{k}_2)}{\partial \mathbf{k}_2} \right| f(E(\mathbf{k}_2))}{\left| \frac{\partial E(\mathbf{k}_1)}{\partial \mathbf{k}_1} \right| f(E(\mathbf{k}_1))} \right] \\
 &\cdot \int_0^t dz \int_0^t dz' \left[\psi_{j\mathbf{k}_2-\sigma}^\dagger(z) M^{AC} \psi_{i\mathbf{k}_1\sigma}(z) \right]^* \\
 &\cdot \left[\psi_{j\mathbf{k}_2-\sigma}^\dagger(z') M^{AC} \psi_{i\mathbf{k}_1\sigma}(z') \right] \int_{-\infty}^{\infty} dq_z L_{AC} \exp(-iq_z |z - z'|) dz' \\
 &\cdot \theta(E_j(\mathbf{k}_2) - E_j^{(0)}).
 \end{aligned} \tag{4.23}$$

Intervalley g-Process Spin Relaxation

The g-process describes the electron intervalley scattering between opposite valleys, which includes only the [001] valley pair in the Brillouin zone. The f-process involves scattering between valleys that reside on perpendicular axes, which will be treated later. For intervalley scattering [53], $L_{AC}=1$. By introducing the Dirac delta function, $2\pi\delta(z - z') = \int_{-\infty}^{\infty} \exp(-iq_z |z - z'|) dq_z$. Again,

$$\int dz' \left[\psi_{j\mathbf{k}_2-\sigma}^\dagger(z') M^{AC} \psi_{i\mathbf{k}_1\sigma}(z') \right] \delta(z - z') = \left[\psi_{j\mathbf{k}_2-\sigma}^\dagger(z) M^{AC} \psi_{i\mathbf{k}_1\sigma}(z) \right]. \tag{4.24}$$

This simplifies Equation 4.23 to

$$\begin{aligned}
 \frac{1}{\tau_{i,LA}(\mathbf{k}_1)} &= \frac{4\pi K_B T}{\hbar \rho \nu_{LA}^2} \sum_j \int_0^{2\pi} \frac{d\varphi}{2\pi} \cdot \frac{1}{(2\pi)^2} \frac{|\mathbf{k}_2|}{\left| \frac{\partial E(\mathbf{k}_2)}{\partial \mathbf{k}_2} \right|} \\
 &\cdot \left[1 - \frac{\left| \frac{\partial E(\mathbf{k}_2)}{\partial \mathbf{k}_2} \right| f(E(\mathbf{k}_2))}{\left| \frac{\partial E(\mathbf{k}_1)}{\partial \mathbf{k}_1} \right| f(E(\mathbf{k}_1))} \right] \\
 &\cdot 2\pi \int_0^t dz \left[\psi_{j\mathbf{k}_2-\sigma}^\dagger(z) M^{AC} \psi_{i\mathbf{k}_1\sigma}(z) \right]^* \left[\psi_{j\mathbf{k}_2-\sigma}^\dagger(z) M^{AC} \psi_{i\mathbf{k}_1\sigma}(z) \right] \\
 &\cdot \theta(E_j(\mathbf{k}_2) - E_j^{(0)}).
 \end{aligned} \tag{4.25}$$

Here, $\nu_{LA}=8700 \frac{m}{s}$, M^{AC} contains the Elliott and Yafet contributions [53], and can be written as (M')

$$M' = \begin{bmatrix} M_{ZZ} & M_{SO} \\ M_{SO}^\dagger & M_{ZZ} \end{bmatrix}, \tag{4.26}$$

$$M_{ZZ} = \begin{bmatrix} \Xi & 0 \\ 0 & \Xi \end{bmatrix}, \quad (4.27)$$

$$M_{SO} = \begin{bmatrix} 0 & D_{SO}(r_y - ir_x) \\ D_{SO}(-r_y - ir_x) & 0 \end{bmatrix}, \quad (4.28)$$

where $(r_y, r_x) = \mathbf{k}_1 + \mathbf{k}_2$, $D_{SO} = 15 \text{meV}/k_0$, $\Xi = 12 \text{eV}$ as the acoustic deformation potential, and other parameters as in Table 3.2. Thus, the expression for M' can be reformulated as

$$M' = \begin{bmatrix} \Xi & 0 & 0 & D_{SO}(r_y - ir_x) \\ 0 & \Xi & D_{SO}(-r_y - ir_x) & 0 \\ 0 & D_{SO}(-r_y + ir_x) & \Xi & 0 \\ D_{SO}(r_y + ir_x) & 0 & 0 & \Xi \end{bmatrix} \quad (4.29)$$

Intravalley Transversal Acoustic Phonons Spin Relaxation

Intrasubband transitions are important for the contributions determined by the shear deformation potential. The term L_{AC} due to transversal acoustic phonons is [53]

$$L_{AC} = \frac{(q_x^2 - q_y^2)^2}{q_x^2 + q_y^2} + \frac{4q_x^2 q_y^2 q_z^2}{(q_x^2 + q_y^2)|q|^2}. \quad (4.30)$$

Applying the theory of residues with $Q^2 = q_x^2 + q_y^2$, one can perform the following integral,

$$\begin{aligned} \int_{-\infty}^{\infty} dq_z \frac{q_z^2 \exp(-iq_z|z - z'|)}{(Q^2 + q_z^2)^2} &= \int_{-\infty}^{\infty} dq_z \frac{q_z^2 \exp(-iq_z|z - z'|)}{(iQ - q_z)^2 (iQ + q_z)^2} \\ &= -2\pi i \left[\left(\frac{d}{dq_z} \frac{q_z^2 \exp(-iq_z|z - z'|)}{(iQ - q_z)^2} \right)_{q_z = -iQ} \right] \\ &= \frac{\pi}{2} \frac{1 - Q|z - z'|}{Q} \exp(-Q|z - z'|). \end{aligned} \quad (4.31)$$

The matrix M^{AC} for the intrasubband transversal acoustic phonons (M) can be expressed like

$$M = \begin{bmatrix} 0 & 0 & \frac{D}{2} & 0 \\ 0 & 0 & 0 & \frac{D}{2} \\ \frac{D}{2} & 0 & 0 & 0 \\ 0 & \frac{D}{2} & 0 & 0 \end{bmatrix}, \quad (4.32)$$

where D is the shear deformation potential as mentioned in Table 3.2. Indeed the intrasubband transitions are important for the contributions determined by D .

Following Equation 4.23 the intrasubband transversal acoustic phonons is

$$\begin{aligned}
 \frac{1}{\tau_{i,TA}(\mathbf{k}_1)} &= \frac{4\pi K_B T}{\hbar \rho \nu_{TA}^2} \sum_j \int_0^{2\pi} \frac{d\varphi}{2\pi} \cdot \frac{1}{(2\pi)^2} \frac{|\mathbf{k}_2|}{\left| \frac{\partial E(\mathbf{k}_2)}{\partial \mathbf{k}_2} \right|} \\
 &\cdot \left[1 - \frac{\left| \frac{\partial E(\mathbf{k}_2)}{\partial \mathbf{k}_2} \right| f(E(\mathbf{k}_2))}{\left| \frac{\partial E(\mathbf{k}_1)}{\partial \mathbf{k}_1} \right| f(E(\mathbf{k}_1))} \right] \\
 &\cdot \int_0^t dz \int_0^t dz' \exp(-\sqrt{q_x^2 + q_y^2} |z - z'|) \cdot \frac{\pi}{2} \\
 &\cdot \left[\Psi_{j\mathbf{k}_2-\sigma}^\dagger(z) M \Psi_{i\mathbf{k}_1\sigma}(z) \right]^* \left[\Psi_{j\mathbf{k}_2-\sigma}(z) M \Psi_{i\mathbf{k}_1\sigma}(z) \right] \\
 &\cdot \left[\frac{4q_x^2 q_y^2 (1 - |z - z'| \sqrt{q_x^2 + q_y^2})}{(\sqrt{q_x^2 + q_y^2})^3} \right] \cdot \theta(E_j(\mathbf{k}_2) - E_j^{(0)}).
 \end{aligned} \tag{4.33}$$

Here, $\nu_{TA} = 5300 \frac{m}{s}$ is the transversal phonon velocity, and $\rho = 2329 \frac{Kg}{m^3}$ is the silicon density [158].

Intravalley Longitudinal Acoustic Phonon Spin Relaxation

The term L_{AC} due to the longitudinal acoustic phonons is [53]

$$L_{AC} = \frac{4q_x^2 q_y^2}{|q|^2}. \tag{4.34}$$

Applying the theory of residues with $Q^2 = q_x^2 + q_y^2$, one can perform the following integral,

$$\begin{aligned}
 \int_{-\infty}^{\infty} dq_z \frac{\exp(-iq_z |z - z'|)}{(Q^2 + q_z^2)^2} &= \int_{-\infty}^{\infty} dq_z \frac{\exp(-iq_z |z - z'|)}{(iQ - q_z)^2 (iQ + q_z)^2} \\
 &= -2\pi i \left[\left(\frac{d}{dq_z} \frac{\exp(-iq_z |z - z'|)}{(iQ - q_z)^2} \right)_{q_z = -iQ} \right] \\
 &= \frac{\pi}{2} \frac{Q |z - z'| + 1}{Q^3} \exp(-Q |z - z'|).
 \end{aligned} \tag{4.35}$$

The matrix M^{AC} for the intrasubband longitudinal acoustic phonons is the same as in Equation 4.32. Then, the intravalley spin relaxation rate due to longitudinal acoustic phonons can be expressed as

$$\begin{aligned}
 \frac{1}{\tau_{i,LA}(\mathbf{k}_1)} &= \frac{4\pi K_B T}{\hbar \rho \nu_{LA}^2} \sum_j \int_0^{2\pi} \frac{d\varphi}{2\pi} \cdot \frac{1}{(2\pi)^2} \cdot \frac{|\mathbf{k}_2|}{\left| \frac{\partial E(\mathbf{k}_2)}{\partial \mathbf{k}_2} \right|} \\
 &\cdot \left[1 - \frac{\left| \frac{\partial E(\mathbf{k}_2)}{\partial \mathbf{k}_2} \right| f(E(\mathbf{k}_2))}{\left| \frac{\partial E(\mathbf{k}_1)}{\partial \mathbf{k}_1} \right| f(E(\mathbf{k}_1))} \right] \\
 &\cdot \int_0^t dz \int_0^t dz' \exp(-\sqrt{q_x^2 + q_y^2} |z - z'|) \frac{\pi}{2} \\
 &\cdot \left[\Psi_{j\mathbf{k}_2-\sigma}^\dagger(z) M \Psi_{i\mathbf{k}_1\sigma}(z) \right]^* \left[\Psi_{j\mathbf{k}_2-\sigma}^\dagger(z) M \Psi_{i\mathbf{k}_1\sigma}(z) \right] \\
 &\cdot \frac{4q_x^2 q_y^2}{(q_x^2 + q_y^2)^{\frac{3}{2}}} \left[\sqrt{q_x^2 + q_y^2} |z - z'| + 1 \right] \theta(E_j(\mathbf{k}_2) - E_j^{(0)}).
 \end{aligned} \tag{4.36}$$

When both the surface roughness and the acoustic phonon mediated components are calculated, the total spin lifetime is calculated by the Matthiessen rule.

4.4 Spin Lifetime Simulations

The observed spin lifetime in unstrained thin films is much different compared to bulk samples. Experiments show a dramatic reduction of the spin relaxation time in Si/SiO₂ interfaces [159]. Figure 4.10 describes how the total spin lifetime (τ_s) and its surface roughness and phonon mediated components vary with the temperature in an unstrained silicon thin-film, for different electron concentrations N_S . With increasing temperature, the number of hot spot points which lie in the energy range determined by the term $f(E)(1 - f(E))$ increases [160]. In combination with the Fermi level lowering this results in the reduction of the spin lifetime. The opposite trend is observed when N_S increases. Increasing the electron concentration shifts the Fermi level upwards and thus increases the spin lifetime. The surface roughness mediated component of τ_s becomes prominent for a sample thickness of as low as $t=1.36\text{nm}$. Thus, τ_s in unstrained silicon film is significantly affected by the electron concentration and temperature. It is further noticed that with increasing temperature, the difference between the spin lifetimes for different values of the electron concentration becomes less pronounced.

4.4.1 Spin Lifetime Enhancement with Shear Strain

Figure 4.11 shows the contributions of the surface roughness (SR), longitudinal acoustic (LA), and transversal acoustic (TA) induced spin lifetime for a sample thickness of $t=2.5\text{nm}$ at room temperature. The spin injection orientation is perpendicular ($\Theta=0$)

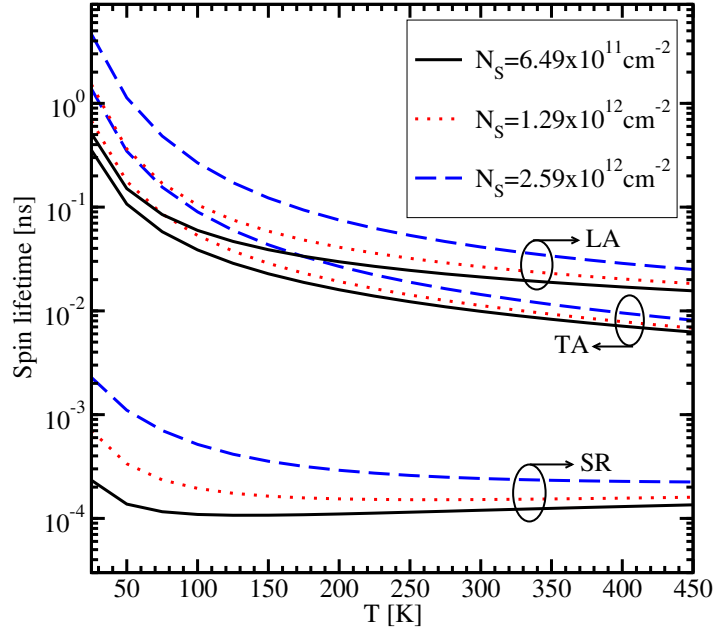


Figure 4.10: The dependence of the spin lifetime including the surface roughness (SR), the longitudinal acoustic (LA) phonon, and the transversal acoustic (TA) phonon mediated components on the temperature and for different values of the electron concentration ($\varepsilon_{xy}=0$, $t=1.36\text{nm}$) is shown.

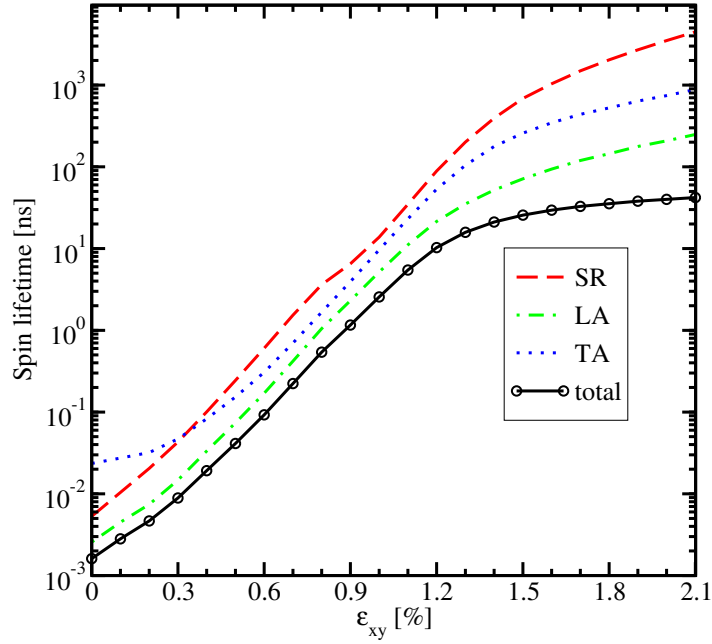


Figure 4.11: The dependence of the spin lifetime and its surface roughness and acoustic phonon induced components over a wide range of ε_{xy} is shown. The film thickness is $t=2.5\text{nm}$, $T=300\text{K}$, and the electron concentration is $N_s=10^{12}\text{cm}^{-2}$.

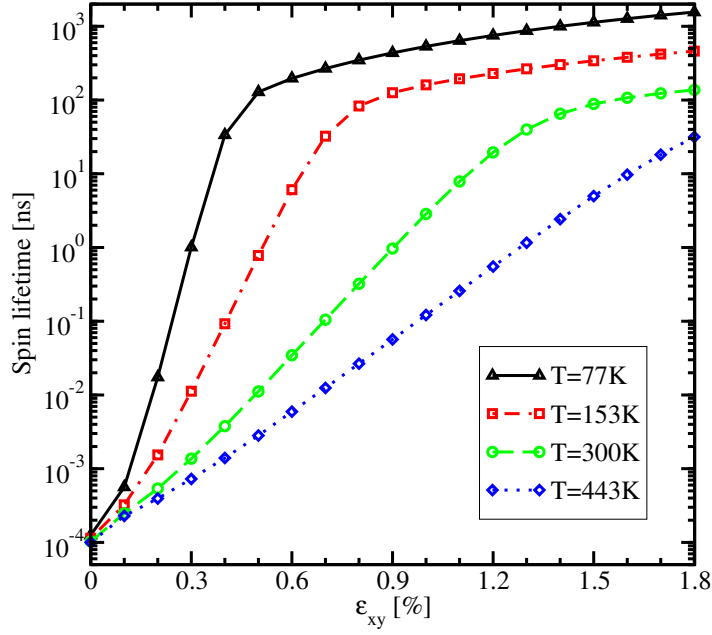


Figure 4.12: The dependence of the spin lifetime on the shear strain ϵ_{xy} is depicted for a film thickness of $t=1.36\text{nm}$, and an electron concentration of $N_S=10^{12}\text{cm}^{-2}$.

to the (001) surface (c.f. Figure 3.5). Several orders of magnitude enhancement is noticed with increasing shear strain ϵ_{xy} for the total spin lifetime τ_s and its all individual components. The variation of τ_s with ϵ_{xy} at different temperatures is shown in Figure 4.12. An orders of magnitude increase of τ_s is noticed for all four evaluated temperatures, and τ_s is highly sensitive to the operating temperature at each stress point. One can confirm that, at higher temperatures the electron-phonon scattering rate significantly increases causing the reduction of τ_s .

4.4.2 Inter- and Intrasubband Components

In order to elucidate the spin relaxation mechanism, the spin-flip caused by the intra- and intersubband scattering must be analyzed. The corresponding components of the spin lifetime at the room temperature (RT) for a sample thickness of $t=2.1\text{nm}$ is shown in Figure 4.13. It is revealed that the major contribution to the spin relaxation time τ_s comes from the intersubband processes. This dependence of τ_s on intersubband transition is attributed to the presence of the spin hot spots. It is further noted that, for a thickness $t=2.1\text{nm}$ when $\epsilon_{xy} \geq 1.4\%$, the intrasubband component also turns out to be non-negligible.

Figure 4.14 delineates the surface roughness induced spin relaxation time with its inter- and intrasubband components at two distinct temperatures and at a very low sample thickness. One can see that, when the temperature decreases the Fermi level energy

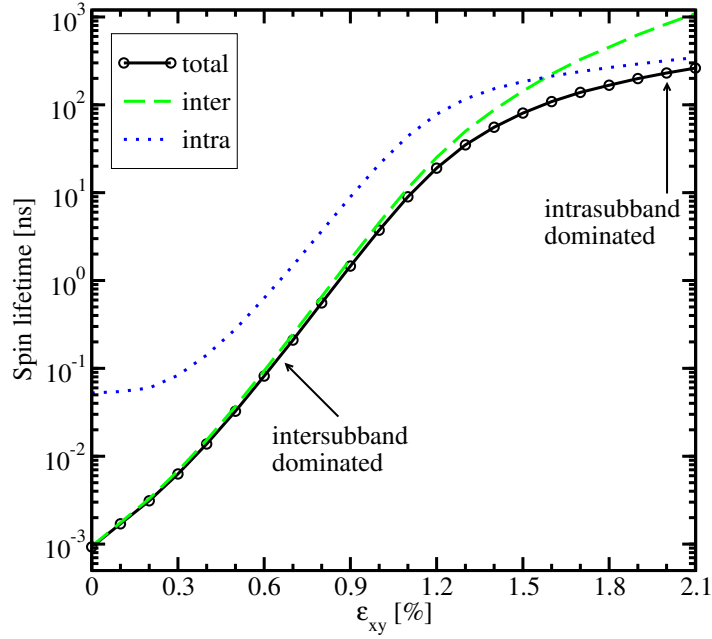


Figure 4.13: The variation of the spin lifetime with its inter- and intrasubband components with ε_{xy} is shown. The film thickness is $t=2.1\text{nm}$, $T=300\text{K}$, and the electron concentration is $N_S=10^{12}\text{cm}^{-2}$.

increases (c.f. Figure 4.14 inset), the intersubband scattering becomes less efficient already at lower values of the shear strain component ε_{xy} , and the total intrasubband component of the spin relaxation time starts playing the significant role at higher ε_{xy} . It is also revealed that at higher ε_{xy} , the surface roughness scattering intrasubband components become close to each other for different temperatures [161]. Therefore, the increase of the total spin lifetime (τ_s) is a consequence of the fact that ε_{xy} introduces a splitting between the usually degenerate unprimed subbands. This lifting of the degeneracy is the crucial factor for the spin lifetime enhancement, as the splitting pushes out the regions of large mixing between the spin-up and spin-down states to higher energies outside of the occupied states (c.f. Figure 4.4). The degeneracy between equivalent valleys has been a longstanding problem in silicon spintronics [55].

4.4.3 Effect of Spin Injection Orientation

Figure 4.15 shows how the surface roughness and the phonon mediated components of the total spin lifetime (denoted as τ_s) depend on the spin injection direction over a wide range of shear strain ε_{xy} . They increase with the spin injection polar angle Θ with equal proportionally factor. This happens as the inter- and intrasubband components of τ_s are equivalently sensitive to Θ , as those increase with increasing Θ . This phenomenon is described in Figure 4.16. Accordingly, τ_s increases with Θ

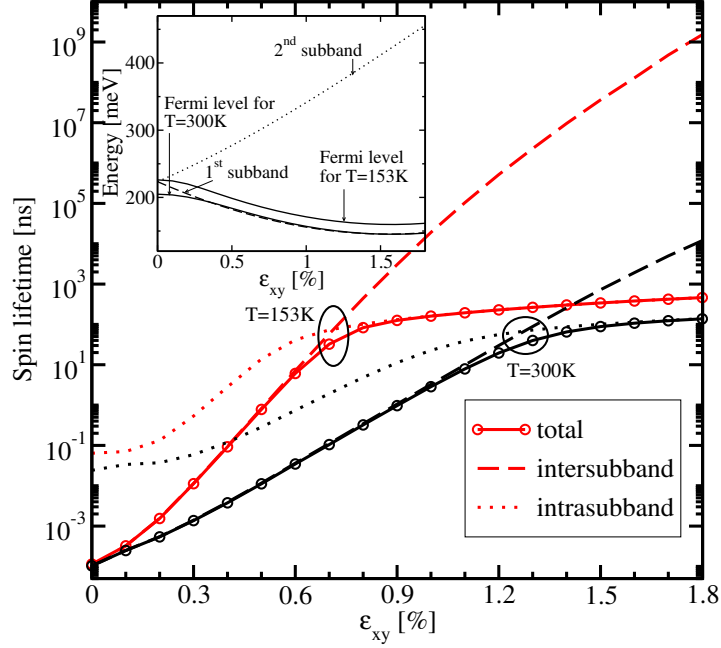


Figure 4.14: The variation of the surface roughness mediated spin lifetime with its inter- and intrasubband components as a function of ε_{xy} at two distinct values of temperature is depicted. The film thickness is $t=1.36\text{nm}$, and the electron concentration is $N_S=10^{12}\text{cm}^{-2}$. The variation of the Fermi levels and the minimum energies ($k_x=k_y=0$) of the lowest unprimed subbands with ε_{xy} is shown (inset).

for all values of the shear strain ε_{xy} . τ_s attains the maximum value for an in-plane spin injection. This result can be correlated with the earlier findings that the spin randomization decreases with increasing Θ at the spin hot spots, and accordingly the spin relaxation rate decreases and the spin lifetime increases (c.f. the section 4.2).

Now, one needs to investigate the dependence of the total spin lifetime τ_s (and the inter- and intrasubband components) on Θ at a fixed stress point. Figure 4.17 highlights the ratio of τ_s for an arbitrary Θ value compared to a perpendicular-plane injection. An analytical expression describing this dependence can be deduced by averaging $|M_S|^2$ (c.f. Equation 4.3) over the in-plane momentum vector and can be expressed as

$$\frac{1}{\tau_s(\Theta)} \propto 1 + \cos^2 \Theta. \quad (4.37)$$

In such a condition,

$$\frac{\tau_s(\Theta)}{\tau_s(\Theta=0)} = \frac{2}{1 + \cos^2 \Theta}, \quad (4.38)$$

and therefore,

$$\tau_s\left(\Theta = \frac{\pi}{2}\right) = 2 \cdot \tau_s(\Theta=0). \quad (4.39)$$

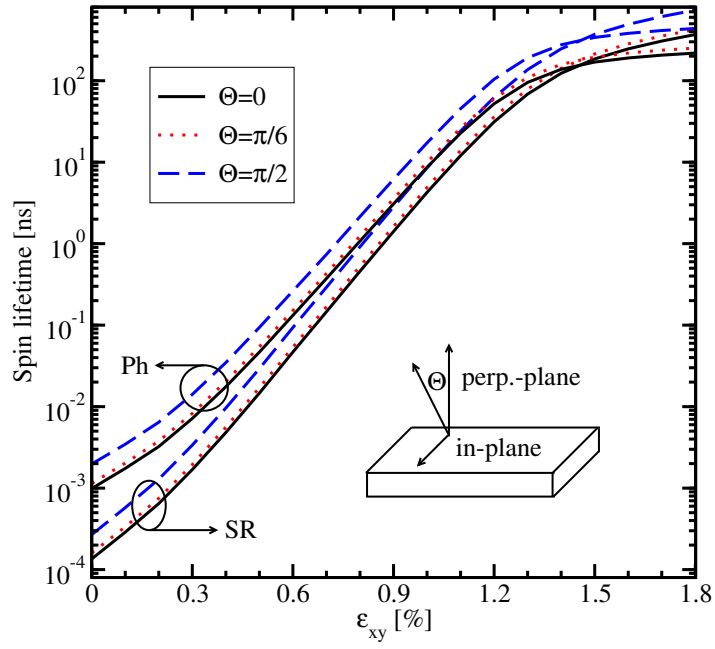


Figure 4.15: The variation of the surface roughness and the phonon mediated components of the spin lifetime with ε_{xy} is shown, when the spin injection orientation (represented by the angle Θ) is used as a parameter. The film thickness is $t=1.36\text{nm}$, $T=300\text{K}$, and the electron concentration is $N_S=10^{12}\text{cm}^{-2}$.

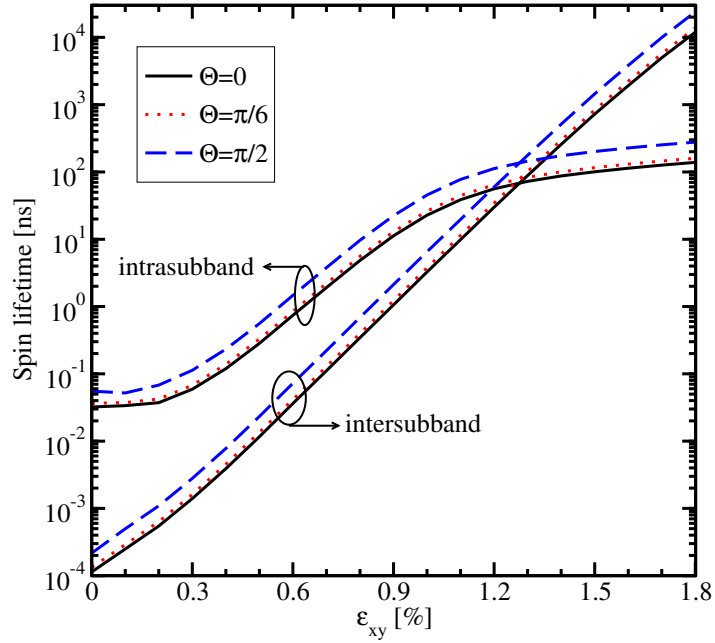


Figure 4.16: The variation of inter- and intrasubband components of the spin lifetime with ε_{xy} is depicted, when Θ is used as a parameter (c.f. Figure 4.16).

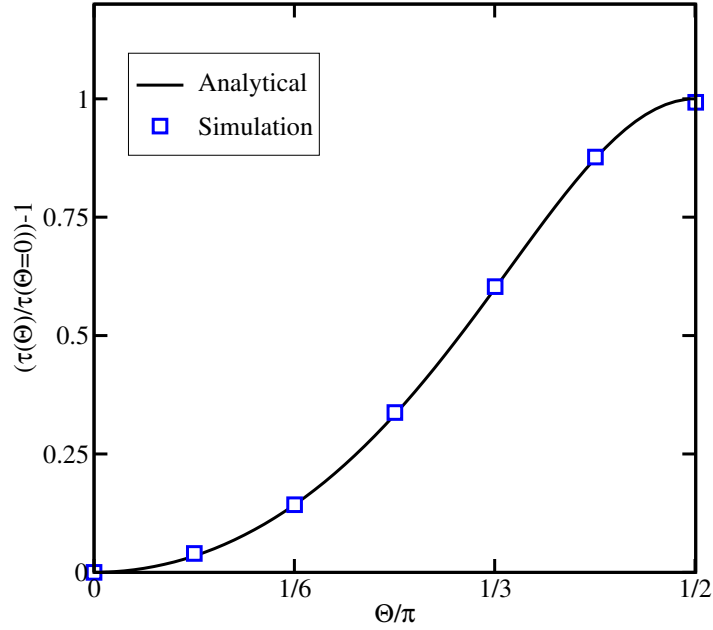


Figure 4.17: The variation of the spin lifetime with the spin injection orientation angle Θ at any fixed value for ε_{xy} is shown. The analytical expression can be found at Equation 4.37.

So, the total spin lifetime τ_s is increased by a factor of two when injected in-plane (OX -direction) compared to the perpendicular-plane (OZ -direction). It is mentioned here that this increase of spin lifetime by the factor of two for an in-plane injection has also been mentioned for bulk silicon [67, 162].

4.5 Momentum Relaxation Time Simulations

In the previous sections one has seen how intersubband transition predominantly determines the total spin lifetime τ_s . The shear strain ε_{xy} can remove the degeneracy between the equivalent valleys to cause the reduction of intersubband spin-flip and hence the giant increment in τ_s . As the momentum scattering times for all the individual components can also be calculated by the thermal averaging as described in Equation 4.12, one must calculate the total momentum scattering time τ_m as a function of ε_{xy} to investigate how the inter- and intrasubband transitions impact τ_m .

4.5.1 Momentum Scattering Matrix Elements

The simplified expression for the surface roughness SR induced momentum scattering matrix elements, normalized to the intrasubband scattering matrix elements at zero

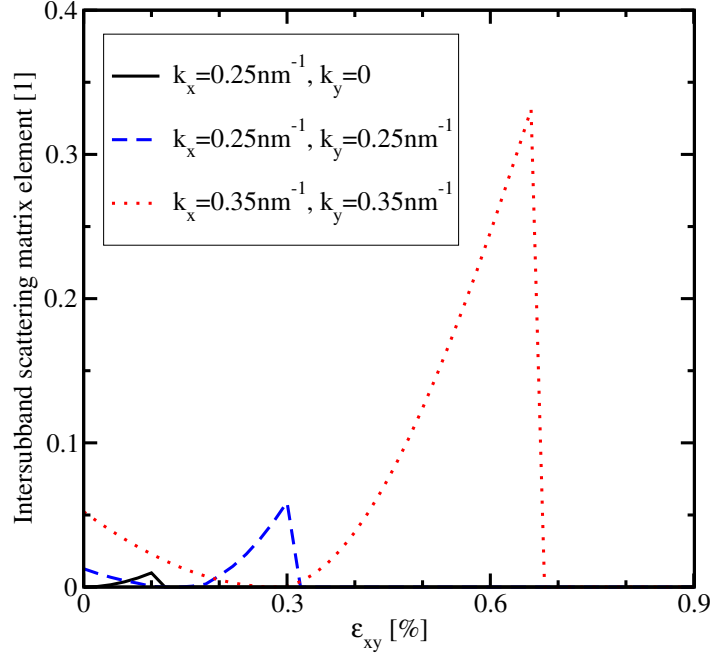


Figure 4.18: The normalized and squared intersubband scattering matrix element is shown as function of ε_{xy} and for several pairs of (k_x, k_y) . The film thickness is set to $t=2\text{nm}$.

strain, is calculated as [129]

$$M_{m,ij} = \left[\frac{\frac{d\Psi_{i\sigma}(z)}{dz} \frac{d\Psi_{j\sigma}(z)}{dz}}{\left(\frac{d\Psi_{i\sigma}(z)}{dz} \frac{d\Psi_{i\sigma}(z)}{dz}\right)_{\varepsilon_{xy}=0}} \right]_{z=\pm \frac{t}{2}}, \quad (4.40)$$

where $\Psi_{i,j}$ are the subband eigenfunctions as obtained earlier. $i, j=1, 2$ are the subband indices, and $\sigma=\pm 1$ is the spin projection to the [001] axis.

Figure 4.18 shows the variation of the normalized and squared intersubband scattering matrix elements with ε_{xy} , for an arbitrary in-plane projection of the \mathbf{k} vector. In contrast to Figure 4.1 no peak is noticed in this case. The intersubband scattering attains its minimum when Equation 4.2 is met [163]. In each case, the intersubband scattering is noticed to be vanishing after a certain strain point. To explain this behavior, the variation of the corresponding energies of the first lowest subband with ε_{xy} , and the minimum energy of the second subband are shown in Figure 4.19. When former goes below the latter, no intersubband scattering would be possible as because the kinetic energy is not sufficient to occupy the states after scattering in the second subband. Figure 4.20 shows the respective normalized and squared intrasubband scattering matrix elements, for a certain (k_x, k_y) pair. The stress-induced unprimed subband splitting is illustrated (c.f. right hand side). The valley splitting minimum is observed to be around $\varepsilon_{xy}=0.145\%$ in agreement with Equation 4.2.

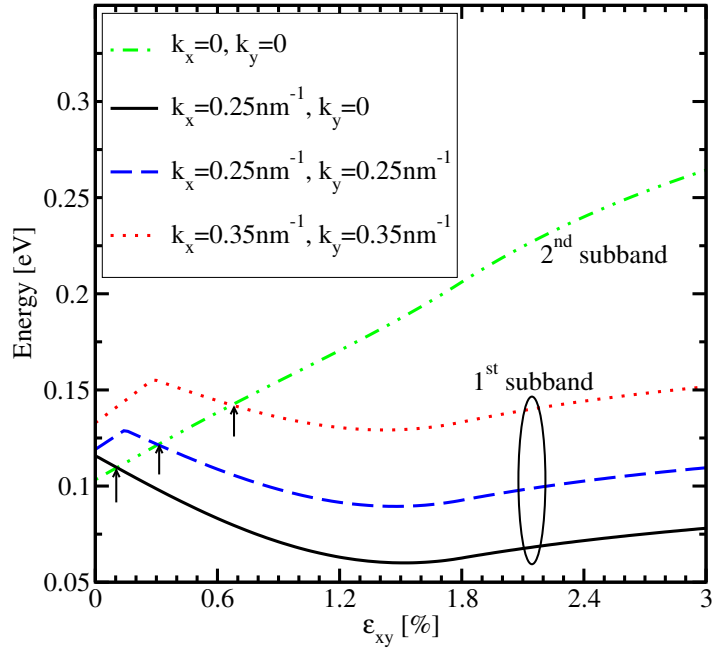


Figure 4.19: The subband energies for the first and the minimum of the second subband (i.e. at $k_x=k_y=0$) as a function of ε_{xy} with the same conditions as in Figure 4.18 is shown. The points where the two cross are highlighted by arrows.

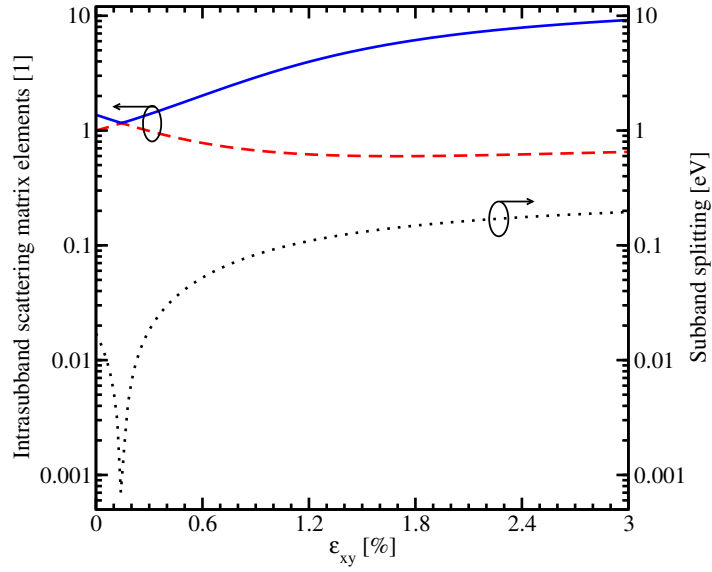


Figure 4.20: The normalized and squared intrasubband scattering matrix elements are shown as function of ε_{xy} ($k_x=k_y=0.25\text{nm}^{-1}$, and $t=2.7\text{nm}$).

4.5.2 Calculation of the Momentum Relaxation Rates

Analogous to Equation 4.16, the surface roughness SR induced momentum relaxation rate is

$$\begin{aligned} \frac{1}{\tau_{i,SR}(\mathbf{k}_1)} &= \frac{2\pi}{\hbar(2\pi)^2} \sum_{j=1,2} \int_0^{2\pi} d\varphi \cdot \pi \Delta^2 L^2 \cdot \frac{1}{\epsilon_{ij}^2 |\mathbf{k}_2 - \mathbf{k}_1|} \cdot \frac{\hbar^4}{4m_l^2} \cdot \frac{|\mathbf{k}_2|}{\left| \frac{\partial E(\mathbf{k}_2)}{\partial \mathbf{k}_2} \right|} \\ &\cdot \left[\left(\frac{d\Psi_{i\mathbf{k}_1\sigma}}{dz} \right)^* \left(\frac{d\Psi_{j\mathbf{k}_2\sigma}}{dz} \right) \right]_{z=\pm \frac{t}{2}}^2 \cdot \exp\left(\frac{-|\mathbf{k}_2 - \mathbf{k}_1|^2 L^2}{4} \right) \\ &\cdot \theta(E_j(\mathbf{k}_2) - E_j^{(0)}). \end{aligned} \quad (4.41)$$

\mathbf{k}_2 is the in-plane wave vector after scattering, φ is the angle between the \mathbf{k}_1 and \mathbf{k}_2 vectors, $\epsilon_{i,j}$ is the dielectric permittivity, L is the autocorrelation length, and Δ is the mean square value of the surface roughness fluctuations [164]. $\sigma = \pm 1$ is the spin projection to the [001] axis. This scattering rate is modeled according to [81], who adapted the original approach of [87] for scattering at two interfaces.

Analogous to the calculation of the spin-flip rate, the phonon induced momentum scattering rate can be written as [69]

$$\begin{aligned} \frac{1}{\tau_{i,PH}(\mathbf{k}_1)} &= \frac{2\pi K_B T}{\hbar \rho \nu_{PH}^2} \sum_j \int_0^{2\pi} \frac{d\varphi}{2\pi} \cdot \frac{1}{(2\pi)^2} \frac{|\mathbf{k}_2|}{\left| \frac{\partial E(\mathbf{k}_2)}{\partial \mathbf{k}_2} \right|} \\ &\cdot \left[1 - \frac{\left| \frac{\partial E(\mathbf{k}_2)}{\partial \mathbf{k}_2} \right| f(E(\mathbf{k}_2))}{\left| \frac{\partial E(\mathbf{k}_1)}{\partial \mathbf{k}_1} \right| f(E(\mathbf{k}_1))} \right] \\ &\cdot 2\pi \int_0^t dz \left[\psi_{j\mathbf{k}_2\sigma}^\dagger(z) M^{PH} \psi_{i\mathbf{k}_1\sigma}(z) \right]^* \left[\psi_{j\mathbf{k}_2\sigma}^\dagger(z) M^{PH} \psi_{i\mathbf{k}_1\sigma}(z) \right] \\ &\cdot \theta(E_j(\mathbf{k}_2) - E_j^{(0)}). \end{aligned} \quad (4.42)$$

Here,

$$\nu_{PH} = \frac{2\nu_{TA} + \nu_{LA}}{3}, \quad (4.43)$$

where $\nu_{TA}=5300 \frac{m}{s}$ is the transversal phonon velocity, $\nu_{LA}=8700 \frac{m}{s}$ is the longitudinal phonon velocity, $\rho=2329 \frac{Kg}{m^3}$ is the silicon density [158], t is the film thickness, and M^{PH} can be described as

$$M^{PH} = \begin{bmatrix} \Xi & 0 & 0 & 0 \\ 0 & \Xi & 0 & 0 \\ 0 & 0 & \Xi & 0 \\ 0 & 0 & 0 & \Xi \end{bmatrix}, \quad (4.44)$$

with $\Xi=12\text{eV}$ [165] as the acoustic deformation potential.

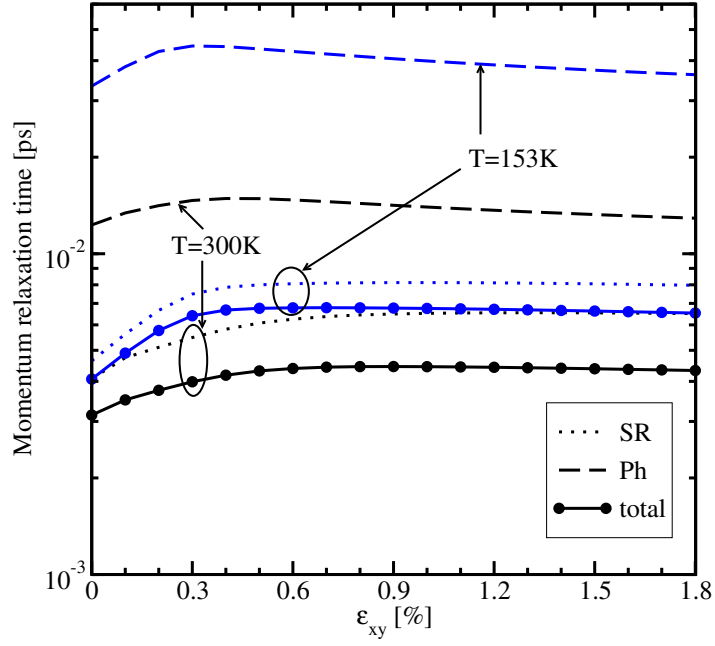


Figure 4.21: The variation of the momentum relaxation time with ε_{xy} is shown with its surface roughness (*SR*) and phonon (*Ph*) mediated components at two distinct temperatures. The film thickness is $t=1.36\text{nm}$, and the electron concentration is $N_S=10^{12}\text{cm}^{-2}$.

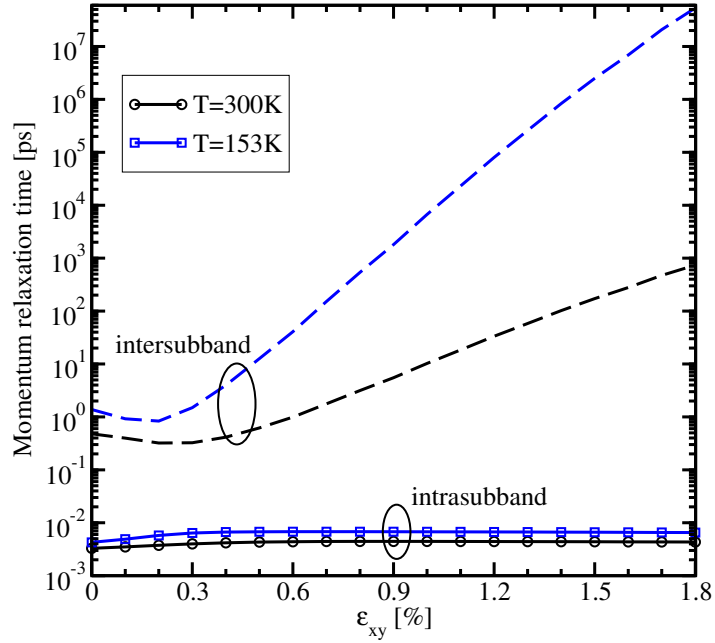


Figure 4.22: The variation of the momentum relaxation time with ε_{xy} is shown with its inter- and intrasubband components corresponding to Figure 4.21.

The dependence of the total momentum relaxation time (τ_m) and its surface roughness and phonon mediated components on the applied shear stress strength ε_{xy} is shown in Figure 4.21 for two different temperatures. It is clear that for a film thickness of $t=1.36\text{nm}$ the surface roughness scattering effect dominates the total momentum relaxation time. This can be seen in Figure 4.21 for $T=300\text{K}$ as well as $T=153\text{K}$. While the surface roughness component is not much affected by temperature, the phonon mediated momentum relaxation rate (time) increases (decreases) strongly with increasing temperature. For this reason, τ_m drops with increasing temperature. Within the ε_{xy} range of 0 to 1.8%, the increment of τ_m is around 130% at $T=300\text{K}$, and 150% at $T=153\text{K}$ for the film thickness of $t=1.36\text{nm}$.

In order to explain the observed behavior, the inter- and intrasubband components of the calculated momentum relaxation time is shown in Figure 4.22. It is revealed that intrasubband scattering solely determines the momentum relaxation time over a wide range of shear strain and at any temperature range. This is in agreement with the selection rule that the elastic processes result in strong intrasubband momentum relaxation [166, 129].

4.6 Valley Splitting in Unstrained Films

The [001] equivalent valley coupling through the Γ -point results in a subband splitting in confined electron structures [87]. This subband splitting is not limited to strained structures and thus must be taken properly into account for the calculation of the spin lifetimes in relaxed structures as well. The valley splitting in a silicon quantum well at zero strain as a function of the quantum well width has been studied for a long time. The expression for the valley splitting can be written as [55]

$$\Lambda_{\Gamma} = \frac{2\pi^2 \Delta_{\Gamma}}{(k_{0\Gamma} \cdot t)^3} \cdot |\sin(k_{0\Gamma} t)|. \quad (4.45)$$

where Δ_{Γ} is the splitting at Γ -point, t is the film thickness, and the other parameters are listed in Table 3.2.

The values of the valley splitting obtained from a 30-band $\mathbf{k} \cdot \mathbf{p}$ model can be found in [167]. This method was developed around the Γ -symmetry point of the Brillouin zone for strained silicon, germanium, and SiGe alloys [145]. On the other hand, a theory based on the localized-orbital approaches has been developed to describe the valley splitting observed in silicon quantum wells in the limit of low electron density by using a $sp^3d^5s^*$ spin-orbit coupled tight-binding model [168]. The use of sp^3s^* tight binding model has also been investigated [169]. Nevertheless, the values of the valley splitting obtained from a 30-band $\mathbf{k} \cdot \mathbf{p}$ model and the tight binding models are summarized and analyzed in [170]. By using the simplified analytical expressions,

- $\Delta_{\Gamma}=2\text{eV}$ for the 30-band $\mathbf{k} \cdot \mathbf{p}$ model, and

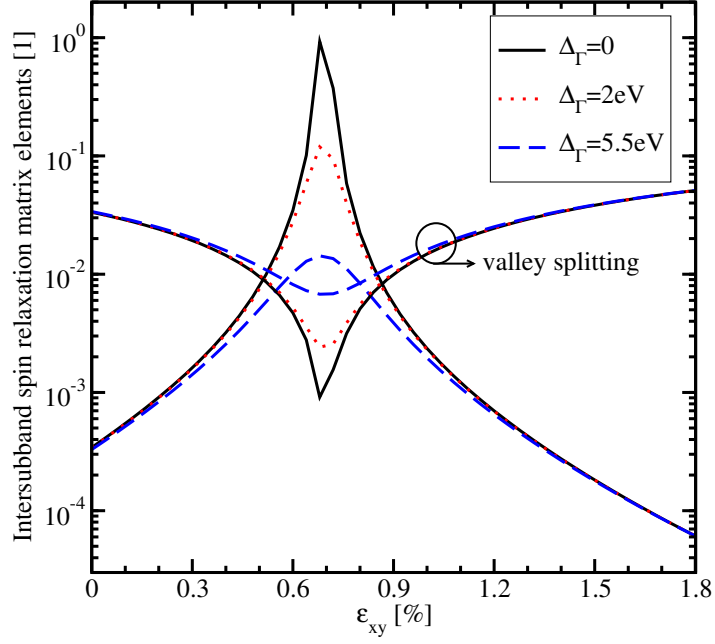


Figure 4.23: The variation of the normalized and squared intersubband spin relaxation matrix elements as function of ε_{xy} is depicted, where $k_x=0.3\text{nm}^{-1}$, $k_y=1\text{nm}^{-1}$, and for different values of Δ_Γ ($t=2.72\text{nm}$).

- $\Delta_\Gamma=5.5\text{eV}$ for the tight-binding model,

one can reproduce the corresponding data. Both methods reproduce the features of the conduction and valence band equally well, but require additional experimental verification at higher energies where discrepancies appear.

Once Λ_Γ is known, one can modify the dispersion equation Equation 3.5 as shown below.

$$E(k) = \frac{\hbar^2 k_z^2}{2m_l} + \frac{\hbar^2 (k_x^2 + k_y^2)}{2m_t} \pm \sqrt{\left(\frac{\hbar^2 k_z k_0}{m_l}\right)^2 + \delta_c^2}, \quad (4.46)$$

with

$$\delta_c = \sqrt{\delta^2 + \left(\frac{k_0}{k_{0\Gamma}}\right)^6 \Delta_\Gamma^2}, \quad (4.47)$$

where δ is given as in Equation 3.6.

4.6.1 Spin Relaxation Matrix Elements

The surface roughness induced normalized and squared intersubband spin relaxation matrix element $|M_S|^2$, with and without the Δ_Γ term, are compared in Figure 4.23. It is noted that the spin relaxation hot spot peaks are greatly diminished to become

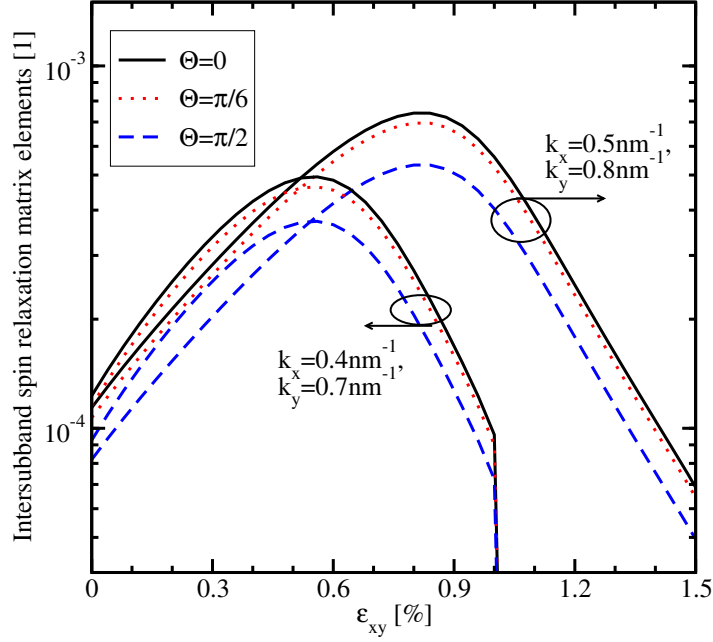


Figure 4.24: The variation of the normalized and squared intersubband spin relaxation matrix elements with ε_{xy} is shown, when the spin injection direction is taken as a parameter ($\Delta_\Gamma=5.5\text{eV}$, $t=1.36\text{nm}$).

smoother with increasing values of Δ_Γ . It has also been mentioned that the difference in the matrix elements' values calculated with and without the Δ_Γ term can reach two orders of magnitude [150]. As like before, the peaks can be correlated with the unprimed subband splitting minima. However, the peaks remain well pronounced, and still attain the maximum at the spin hot spots. Figure 4.23 also depicts how the minimum of the valley splitting increases when the Δ_Γ term increases.

Figure 4.24 describes how $|M_S|^2$ is reduced with increasing spin injection angle Θ , for any pair of (k_x, k_y) . This behavior is consistent with Equation 4.4, indicating that this equation is general and it is applied in both bulk silicon and thin silicon films (with or without presence of the unstrained subband splitting term Δ_Γ). Therefore, the spin relaxation rate can be suppressed with increasing Θ .

4.6.2 Spin Lifetime Calculations

The variation of the surface roughness (SR) and the phonon (Ph) mediated spin relaxation components of the total spin lifetime τ_s with the shear strain ε_{xy} , for different Δ_Γ is shown in Figure 4.25. One can observe that the increase of τ_s is less pronounced, when the value of Δ_Γ increases. However, even when Δ_Γ is taken to be 5.5eV , the value of τ_s increases by two orders of magnitude. It can also be seen that at high ε_{xy} ,

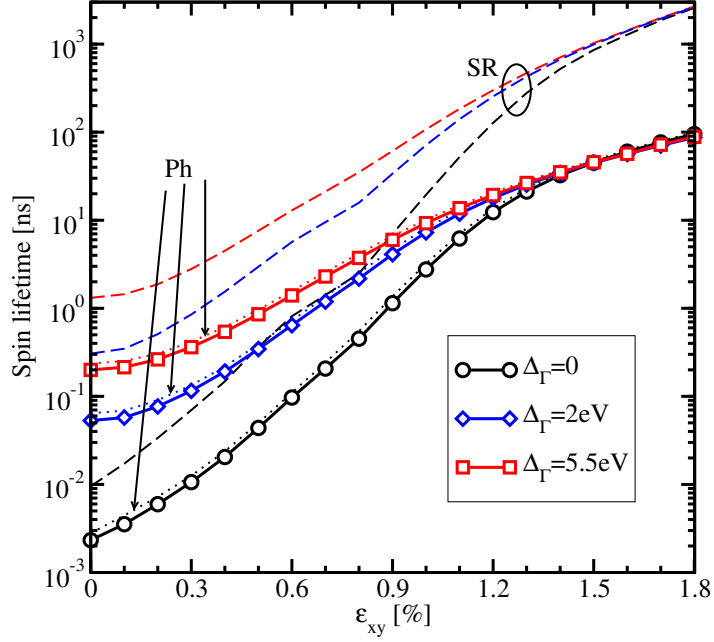


Figure 4.25: The variation of the surface roughness (*SR*) and the phonon (*Ph*) mediated spin lifetime with ε_{xy} is shown, when all possible values for Δ_Γ (c.f. Equation 4.45) are considered. The sample thickness is $t=2.72\text{nm}$, $T=300\text{K}$, and the electron concentration is $N_S=10^{12}\text{cm}^{-2}$.

the total spin lifetime and its components converge to the same value independent of Δ_Γ [171].

In order to understand this behavior, the spin-flip caused by the intra- and intervalley transitions needs to be analyzed. Figure 4.26 shows the energy levels of the two lowest unprimed subbands, which are primarily responsible for the spin relaxation at the different Δ_Γ values. The unprimed subbands are degenerate at zero strain without the Δ_Γ term. The Δ_Γ term lifts the degeneracy even at zero strain. The figure also shows how the increasing ε_{xy} inflicts the subband splitting between the unprimed valley pair. With increasing ε_{xy} , the influence of Δ_Γ vanishes as is obvious from Equation 4.46. Figure 4.27 depicts the inter- and intrasubband scattering components of τ_s at two distinct temperatures. The intersubband spin-flip process remains dominant in determining the total spin lifetime τ_s . However, with increasing strain its influence becomes weaker, in accordance with Figure 4.26. At high valley splitting, the spin relaxation is determined by intrasubband scattering which does not depend on Δ_Γ .

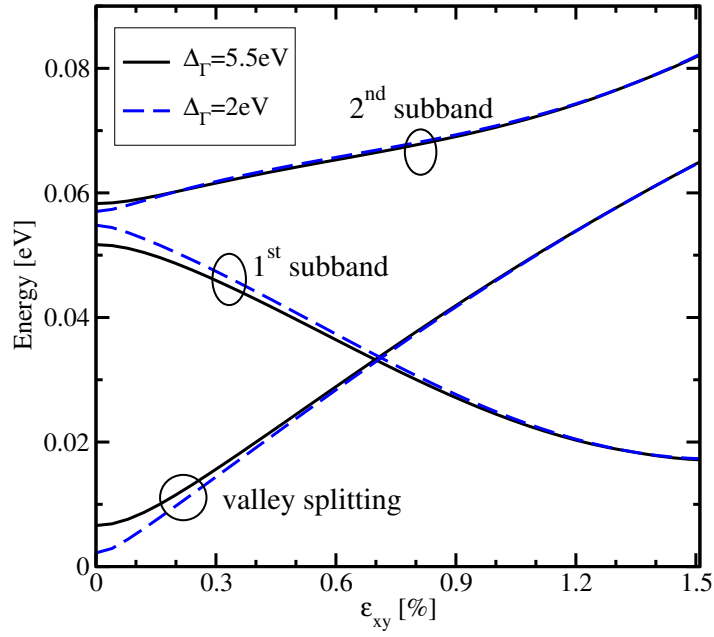


Figure 4.26: The energies of the two lowest unprimed subbands with ε_{xy} at two distinct Δ_{Γ} values are shown. The sample thickness is $t=2.72\text{nm}$, $T=300\text{K}$, and the electron concentration is $N_S=10^{12}\text{cm}^{-2}$.

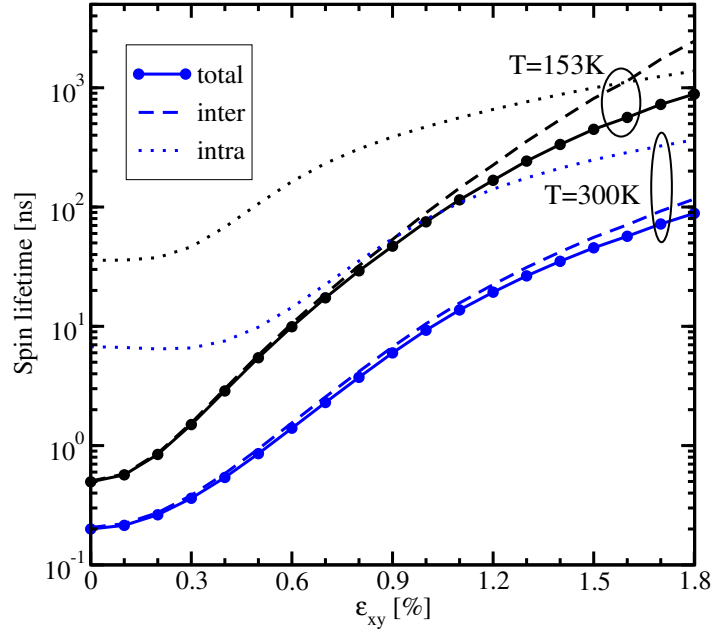


Figure 4.27: The variation of the spin lifetime and its inter- and intrasubband components with ε_{xy} are depicted, when $t=2.72\text{nm}$, the electron concentration $N_S=10^{12}\text{cm}^{-2}$, and $\Delta_{\Gamma}=5.5\text{eV}$.

4.7 Primed Subbands and f-Processes

4.7.1 Primed $\mathbf{k} \cdot \mathbf{p}$ Hamiltonian

A shear strain component in the [110] direction does not affect the primed valleys along [100] and [010] directions. If a quantization along OX -axis is assumed, the following Hamiltonian governing the primed subbands can be written as [72, 146],

$$H' = \begin{bmatrix} H'_1 & H'_3 \\ H'_3 & H'_2 \end{bmatrix}, \quad (4.48)$$

where the individual components are represented as,

$$H'_{j=1,2} = \left[\frac{\hbar^2 k_z^2}{2m_l} + \frac{\hbar^2(k_x^2 + k_y^2)}{2m_t} + (-1)^j \frac{\hbar^2 k_x k_y}{M} + \tilde{U}(z) \right] I, \quad (4.49)$$

and

$$H'_3 = \begin{bmatrix} \frac{\hbar^2 k_z k_0}{m_l} & 0 \\ 0 & \frac{\hbar^2 k_z k_0}{m_l} \end{bmatrix}. \quad (4.50)$$

4.7.2 Optical Phonon Limited Spin Relaxation Rate

The intervalley f-processes are responsible for spin relaxation in bulk silicon which involves the primed subbands [53]. The spin relaxation rate is calculated by [69]

$$\begin{aligned} \frac{1}{\tau_{i,(fp)}(\mathbf{k}_1)} &= \frac{4\pi 3d_0^2}{\hbar \rho a^2 \omega_{op}} \sum_j \int_0^{2\pi} \frac{d\varphi}{2\pi} \int_{-\infty}^{\infty} \frac{dq_z}{(2\pi)^2} \cdot \frac{|\mathbf{k}_2|}{\left| \frac{\partial E(\mathbf{k}_2)}{\partial \mathbf{k}_2} \right|} \\ &\cdot \left[1 - \frac{\left| \frac{\partial E(\mathbf{k}_2)}{\partial \mathbf{k}_2} \right| f(E(\mathbf{k}_2))}{\left| \frac{\partial E(\mathbf{k}_1)}{\partial \mathbf{k}_1} \right| f(E(\mathbf{k}_1))} \right] \left(n_{op} + \frac{1}{2} \pm \frac{1}{2} \right) \\ &\cdot \sum_{\alpha_1} \left| \varrho_{\alpha_1}^{op}(q) \sum D_{\alpha_1 \alpha_2} \int_0^t dz \Psi_{j\mathbf{k}_2-\sigma}^*(z) \exp(-iq_z z) \Psi_{i\mathbf{k}_1\sigma}(z) \right|^2 \\ &\cdot \theta(E_j(\mathbf{k}_2) - E_j^{(0)} \pm \hbar\omega_{op}), \end{aligned} \quad (4.51)$$

where d_0 is the optical deformation potential, a is the silicon lattice constant, ω_{op} denotes the frequency of the optical phonons, and n_{op} describes the Bose occupation factor

$$n_{op} = \frac{1}{\exp\left(\frac{\hbar\omega_{op}}{K_B T}\right) - 1}. \quad (4.52)$$

The $+(-)$ sign refers to phonon emission (absorption). The relaxation rate for the transition between primed and unprimed subbands is given by [69]

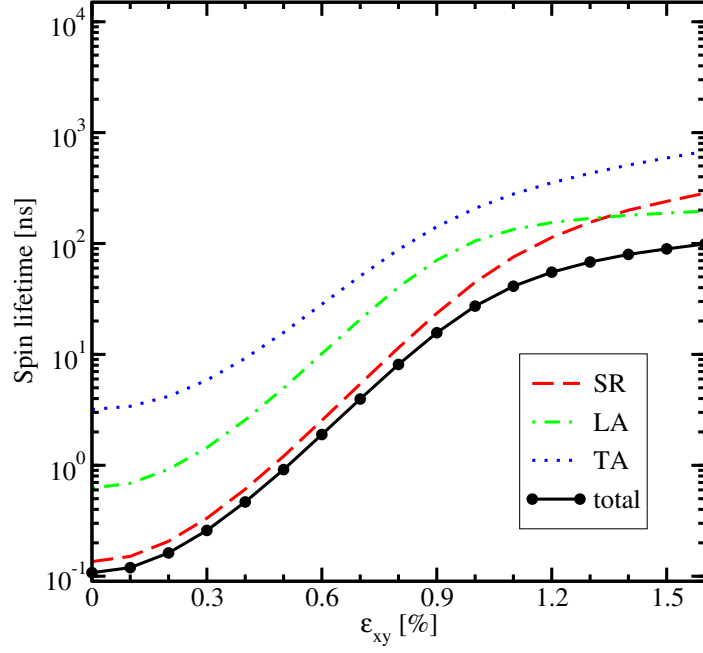


Figure 4.28: The variation of the spin lifetime and its surface roughness (*SR*), the longitudinal (*LA*) and the transversal (*TA*) acoustic phonon mediated components with ε_{xy} is shown. $\Delta_{\Gamma}=5.5\text{eV}$ (c.f. Equation 4.45), the sample thickness $t=1.36\text{nm}$, $T=300\text{K}$, and the electron concentration $N_S=10^{12}\text{cm}^{-2}$ are used.

$$\frac{1}{\tau_{i,OP}(\mathbf{k}_1)} = \frac{2\pi}{\rho\omega_{op}} \sum_j \rho_j(E_i \mp \hbar\omega_{op}) \int_0^t \left| \psi_{j\mathbf{k}_2}^\dagger(z) M^{OP} \psi_{i\mathbf{k}_1}(z) \right|^2 dz \quad (4.53)$$

$$\cdot \frac{1 - f(E_i \mp \hbar\omega_{op})}{1 - f(E_j)} \left(n_{op} + \frac{1}{2} \pm \frac{1}{2} \right),$$

where $\rho_j(E)$ is the density of states for subband j , and M^{OP} is given by

$$M^{OP} = \begin{bmatrix} 0 & D_{OP} & 0 & D_{OP} \\ D_{OP} & 0 & D_{OP} & 0 \\ 0 & D_{OP} & 0 & D_{OP} \\ D_{OP} & 0 & D_{OP} & 0 \end{bmatrix} \quad (4.54)$$

with $D_{OP}=6.5\text{meV}\frac{2\pi}{a}$ [53].

4.7.3 Optical Phonons in Spin Lifetime

Figure 4.28 describes the total spin lifetime τ_s and its components for a film thickness of $t=1.36\text{nm}$. It is observed that the surface roughness *SR* induced component plays

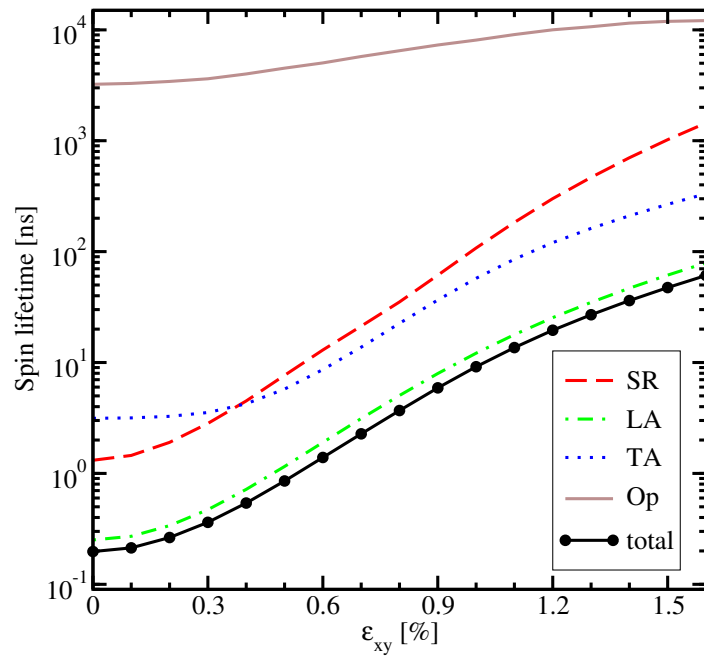


Figure 4.29: The variation of the spin lifetime and its components (along with the optical phonon Op mediated component) with ε_{xy} is shown when $t=2.72\text{nm}$ and the other parameters are as given in Figure 4.28.

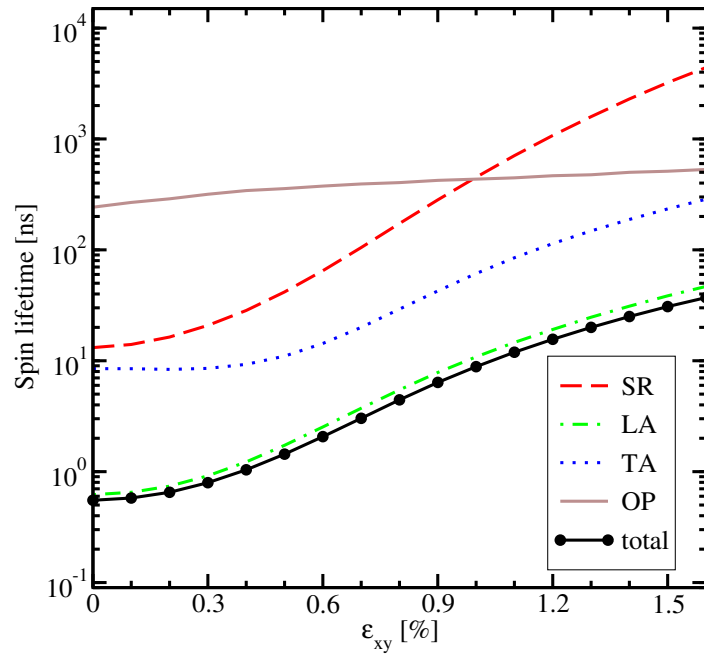


Figure 4.30: The variation of the spin lifetime and its components with ε_{xy} is shown when $t=4.34\text{nm}$ and the other parameters are as given in Figure 4.28.

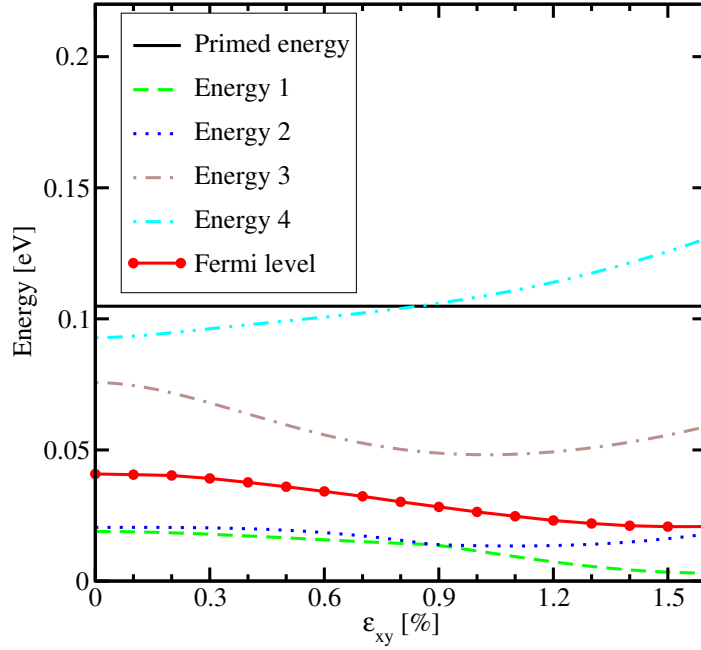


Figure 4.31: The dependence of the minimum energies for primed and unprimed subbands as well as the Fermi energy on strain is shown for Figure 4.30.

the major role in determining τ_s for such a thin film, although the longitudinal acoustic LA phonon mediated part becomes non-negligible when $\varepsilon_{xy} > 1.3\%$. The transversal acoustic TA phonon mediated component remains non-significant throughout a wide stress range. One has to mention that for such a low thickness, the lowest unprimed subbands are solely responsible for determining τ_s due to their low quantization energy [149].

Figure 4.29 describes the variation of the total spin lifetime τ_s and its components on ε_{xy} for a thickness of $t=2.72\text{nm}$. The longitudinal acoustic LA phonon induced part of the spin lifetime turns out to be prominent over a wide range of stress at the increased film thickness. For this case the spin-flip rate due to the surface roughness SR is not as pronounced as before whereas the transversal acoustic TA phonon mediated component has no significant effect as found earlier. For the sake of completeness the optical phonon Op induced part is shown as well, even though it does not impact τ_s . The Op phonon mediated spin flip, which occurs between non-equivalent valleys, does not show high orders of magnitude enhancement with ε_{xy} [172]. Due to the rather high energies of the primed subbands in relation to the unprimed subbands, the Op phonon transitions are rare, which is reflected in their non-significant contribution in τ_s . However, their influence gradually becomes prominent when sample thickness is increased (i.e. Figure 4.30), especially at higher strain. This behavior is explained in Figure 4.31 where the dependence of minimum energies for primed and unprimed subbands on strain with the parameters as in Figure 4.30 together with the Fermi en-

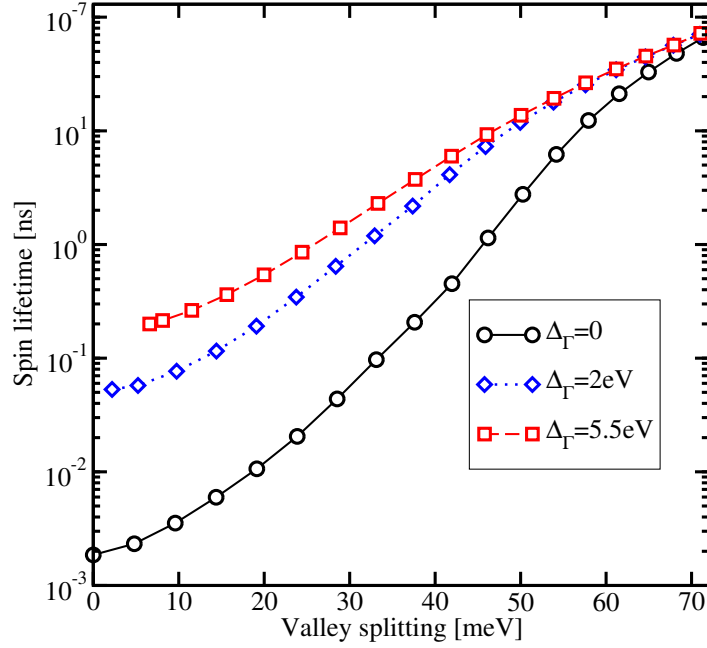


Figure 4.32: The prediction of the spin lifetime with the valley splitting results (c.f. Figure 4.26) is highlighted.

ergy is described. The minimum energy of the primed subband is located at the point $k_z=k_0$, and $k_y=0$, and the unprimed subband is at $k_x=0$, and $k_y=0$ [172]. Energy 1 and Energy 2 stand for the lowest subbands of the two opposite valleys along [001] direction. Energy 3 and Energy 4 stand for the second unprimed subbands. The increasing importance of the f-process comes from the fact that the distance between the Fermi energy and the lowest energy in the primed subband decreases with increasing thickness. Moreover at the film thickness of $t=4.34\text{nm}$, the LA phonon induced part still remains pivotal in determining the total spin lifetime τ_s .

Thus, one can conclude in the following way.

- The total spin lifetime is highly sensitive to the film thickness.
- The surface roughness mediated component completely loses its significance for a film thickness of more than 3nm.
- The longitudinal acoustic phonon induced part is the dominant mechanism for a film thickness of more than 2nm.
- The effect of a several orders of magnitude increase of the spin lifetime in strained films is mitigated for thicker films (thickness larger than 7nm).

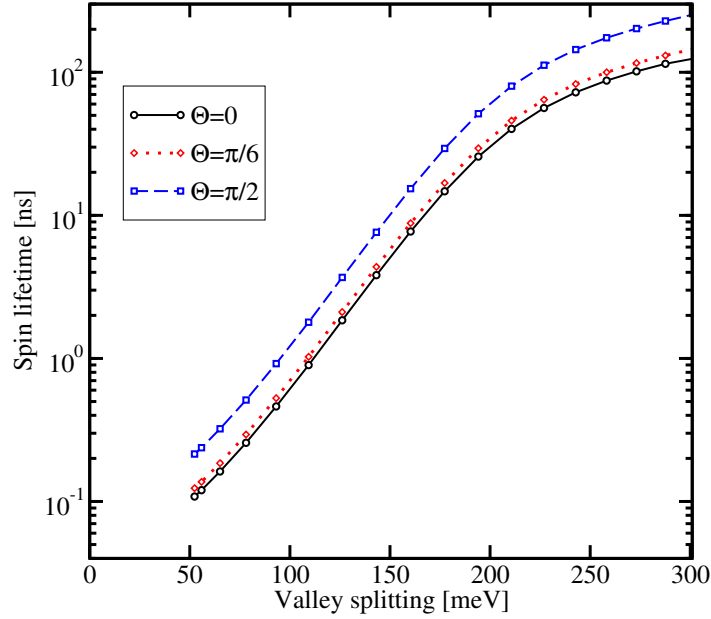


Figure 4.33: The variation of the spin lifetime with the valley splitting is described, when $\Delta_{\Gamma}=5.5\text{eV}$. The sample thickness is $t=1.36\text{nm}$, $T=300\text{K}$, and the electron concentration is $N_S=10^{12}\text{cm}^{-2}$. The spin injection orientation is used as a parameter.

Spin Lifetime with Valley Splitting

In Figure 4.32 the enhancement of the total spin lifetime τ_s considering the total valley splitting (c.f. Figure 4.26) is calculated for a film thickness of $t=2.72\text{nm}$. One observes the strong dependence of τ_s on the Δ_{Γ} , particularly at the lower range of the valley splitting. This behavior can be correlated with the suppression of the spin hot spots with increasing Δ_{Γ} as explained earlier (c.f. Figure 4.23). However, for all cases the spin lifetime is boosted by several orders of magnitude.

Effect of Spin Injection Orientation

The spin relaxation time τ_s increases when the spin injection orientation is drawn towards in-plane, if one incorporates the Δ_{Γ} value into the calculations. The enhancement of τ_s including the valley splitting for different spin injection angles Θ is shown in Figure 4.33. Consistent with the analysis from the section 4.4.3, one observes that τ_s is increased by a factor of two once injected in-plane compared to the perpendicular-plane, even though one includes the Δ_{Γ} term. Therefore, one can conclude that the result Equation 4.38 is more general as it is applied in both bulk silicon and thin silicon films.

5 Spin Diffusion in Silicon

"I keep six honest serving men, They
taught me all I knew: Their names
are What and Why and When and
How and Where and Who."

Rudyard Kipling

In order to design and fabricate high-performance silicon-based spintronic devices, a comprehensive understanding of the spin transport properties of a semiconducting channel ($\sim \mu\text{m}$) is needed. In this chapter, the spin injection in silicon from a ferromagnetic semiconductor (FMS) by electrical means is investigated, when spin is injected from a charge neutral source. Even though a sufficient analysis of the spin transport under charge neutrality is available in literature [173, 174, 175], the attention there has been on the magnetoresistance. Thus, it becomes mandatory to also investigate the spin signal when the charge neutrality condition is violated. In such a case, one has to solve the spin drift-diffusion equations coupled with the Poisson equation. This is done because from the Poisson equation one can derive the electric potential (and hence the electric field) in the conducting channel, which prominently influences the spin diffusion [173]. In fact, experiments have shown that electric fields can severely affect spin diffusion in semiconductors [176, 177].

At first the fundamental charge transport equations [178] will be discussed. Afterwards it will be shown how to extend those equations for spin transport.

5.1 Semi-Classical Model of Charge Transport

5.1.1 Poisson's Equation

The Poisson equation correlates the electrostatic potential V to a given charge distribution $\hat{\rho}$. If the permittivity tensor is expressed as $\tilde{\epsilon}$, one can write the Poisson equation as

$$\nabla \cdot \tilde{\epsilon} \cdot \nabla V = -\hat{\rho}. \quad (5.1)$$

The charge distribution can be expressed as $\hat{\rho} = q(p - n + C)$, where n (p) represents the electron (hole) concentration per unit volume, q is the fundamental charge unit,

and the concentrations of ionized impurities and the dopant are added up as the fixed charge concentration C . These fixed charges can originate from charged impurities of donor (N_D) and acceptor (N_A) type and from trapped electrons (C_1) and holes (C_2)

$$C = N_D - N_A - C_1 + C_2 . \quad (5.2)$$

The electric field ($\tilde{\mathbf{E}}$) is related to V by

$$\tilde{\mathbf{E}} = -\nabla V . \quad (5.3)$$

5.1.2 Continuity Equations

The charge transport model is derived from the continuity equation which takes care of mass conservation (time is represented by \tilde{t})

$$\nabla \cdot \mathbf{J} + q \frac{\partial \hat{\rho}}{\partial \tilde{t}} = 0 . \quad (5.4)$$

The total current density is \mathbf{J} . One can decompose the contributions of the current $\mathbf{J} = \mathbf{J}_n + \mathbf{J}_p$, where \mathbf{J}_n (\mathbf{J}_p) denotes the electron (hole) current density. Assuming all immobile charges as fixed with respect to time, $\frac{\partial \hat{\rho}}{\partial \tilde{t}} = q \frac{\partial(p-n)}{\partial \tilde{t}}$ as $\frac{\partial C}{\partial \tilde{t}} = 0$. Then, the continuity equation (Equation 5.4) can be separated into an electron and a hole related parts,

$$\nabla \cdot (\mathbf{J}_n + \mathbf{J}_p) + q \frac{\partial(p-n)}{\partial \tilde{t}} = 0 . \quad (5.5)$$

This step enables to write the electron and hole related contributions as two independent equations,

$$\nabla \cdot \mathbf{J}_n - q \frac{\partial n}{\partial \tilde{t}} = qR , \quad (5.6a)$$

$$\nabla \cdot \mathbf{J}_p + q \frac{\partial p}{\partial \tilde{t}} = -qR . \quad (5.6b)$$

where the net generation-recombination rate is represented as R .

5.1.3 Drift-Diffusion Equations

As the Poisson equation (Equation 5.1) and the two continuity equations (Equation 5.6a and Equation 5.6b) involve five unknown quantities (viz. V , n , p , \mathbf{J}_n , and \mathbf{J}_p), one needs two more conditions to make the equation system complete. Now, there are two major effects which lead to current flow in semiconductors (e.g. silicon). First, the drift of charged carriers due to the influence of an electric field, and second, the diffusion current due to a concentration gradient of the carriers. It is hereby mentioned that the drift-diffusion model considers the temperature to be constant throughout the device [179], both for the charge carriers and the lattice.

The charged carriers in a semiconductor subjected to an electric field are accelerated and acquire a certain drift velocity. The orientation depends on the charge state, holes are accelerated in direction of the electric field and electrons in the opposite direction. The magnitude of the drift velocity depends on the probability of scattering events. At low impurity concentration, the carriers mainly collide with the crystal lattice. When the impurity concentration is increased the collision probability with the charged dopants through Coulomb interaction becomes more and more likely, thus reducing the drift velocity with increasing doping concentration [180].

The drift component is expressed using the concept of carrier mobility, which is the proportionality factor between the electric field strength ($\tilde{\mathbf{E}}$) and the average carrier velocity. If one denotes μ_n (μ_p) as the electron (hole) mobilities (assumed isotropic in the channel under investigation), in the low electric field range one can write the corresponding average carrier velocities as $\mathbf{v}_n = -\mu_n \tilde{\mathbf{E}}$ and $\mathbf{v}_p = \mu_p \tilde{\mathbf{E}}$. Then the drift current density for the electrons and the holes can be expressed as $\mathbf{J}_n^{\text{Drift}} = -qn\mathbf{v}_n = qn\mu_n \tilde{\mathbf{E}}$ and $\mathbf{J}_p^{\text{Drift}} = qp\mathbf{v}_p = qp\mu_p \tilde{\mathbf{E}}$. The signs are justified as electrons (holes) move against (with) the field direction. One can express the conductivities as $\sigma_n = qn\mu_n$ for the electrons and $\sigma_p = qp\mu_p$ for the holes, then $\mathbf{J}_n^{\text{Drift}} = \sigma_n \tilde{\mathbf{E}}$ and $\mathbf{J}_p^{\text{Drift}} = \sigma_p \tilde{\mathbf{E}}$.

A concentration gradient of carriers leads to carrier diffusion. This is because of their random thermal motion which is more probable in the direction of the lower concentration. The electron current contribution due to the concentration gradient is written as $\mathbf{J}_n^{\text{Diffusion}} = qD_n \nabla n$ and the hole current as $\mathbf{J}_p^{\text{Diffusion}} = -qD_p \nabla p$, where D_n and D_p are the diffusion coefficients for electrons and holes. For the non-degenerate semiconductors and in thermal equilibrium, one can relate the diffusion coefficient with the mobility by using Einstein's relation

$$D_n = \left(\frac{K_B T}{q} \right) \mu_n, \quad (5.7a)$$

$$D_p = \left(\frac{K_B T}{q} \right) \mu_p, \quad (5.7b)$$

where K_B is the Boltzmann's constant, and T is the temperature. The thermal voltage (V_T) is described as

$$V_T = \frac{K_B T}{q}. \quad (5.8)$$

Thus, the diffusion coefficient can be written as $D_n = \mu_n V_T$. Here, the non-degenerate semiconductors are defined as semiconductors for which the Fermi energy is at least $3K_B T$ away from both the conduction and the valence band edges [117, 179]. One can assume the considered semiconductor to be lightly doped and thus non-degenerate, as it is the case in spintronic applications [173]. However, when the doping becomes very high, the Fermi level rises more and more towards the conduction band and the transport becomes degenerate. In such a case, the transport equations must be expressed in the language of chemical potentials of the carriers instead of their concentrations [173, 181].

Combining the current contributions of the drift and the diffusion effect one gets

$$\mathbf{J}_n = qn\mu_n\tilde{\mathbf{E}} + qD_n\nabla n, \quad (5.9a)$$

$$\mathbf{J}_p = qp\mu_p\tilde{\mathbf{E}} - qD_p\nabla p. \quad (5.9b)$$

By inserting Equation 5.9a into Equation 5.6a and Equation 5.9b into Equation 5.6b one obtains

$$\nabla \cdot (\mu_n n \nabla V - \mu_n V_T \nabla n) + \frac{\partial n}{\partial t} = -R, \quad (5.10a)$$

$$\nabla \cdot (\mu_p p \nabla V + \mu_p V_T \nabla p) - \frac{\partial p}{\partial t} = R. \quad (5.10b)$$

From the equations Equation 5.1, Equation 5.10a, and Equation 5.10b, one can obtain the unknown parameters n , p , and V . Despite the clear limitations for the description of state-of-the-art devices, these set of equations are still widely used in TCAD applications due to their least qualitative results and their computational inexpensiveness.

5.1.4 Quasi-Fermi Levels

The thermal equilibrium does not demand a position-independent potential. For instance

$$E_C(\mathbf{r}) = E_{C,0}(\mathbf{r}) - qV(\mathbf{r}), \quad (5.11a)$$

$$E_V(\mathbf{r}) = E_{V,0}(\mathbf{r}) - qV(\mathbf{r}), \quad (5.11b)$$

$$E_i(\mathbf{r}) = E_{i,0}(\mathbf{r}) - qV(\mathbf{r}), \quad (5.11c)$$

denoting the conduction band edge energy E_C , the valence band edge energy E_V , and the intrinsic Fermi level energy E_i , respectively. Treating the situation away from thermal equilibrium complicates the matter. One can reformulate Equation 5.9a with Equation 5.3 as

$$\begin{aligned} \mathbf{J}_n &= q\mu_n V_T \nabla n - qn\mu_n \nabla V \\ &= q\mu_n n \left(V_T \left(\frac{n_i}{n} \right) \nabla \left(\frac{n}{n_i} \right) - \nabla V \right) \\ &= q\mu_n n \nabla \left(\underbrace{V_T \ln \left(\frac{n}{n_i} \right) - V}_{-\phi_n} \right), \end{aligned} \quad (5.12)$$

where n_i is the intrinsic carrier concentration. This shows that the drift and the diffusive contribution can be merged into one quantity. This quantity can be related to the quasi-Fermi level as follows [182] $-q\phi_n = E_{F,n} - E_{i,0}$. Therefore, the current depends on the gradient of the quasi-Fermi levels

$$\mathbf{J}_n = n\mu_n \nabla E_{F,n}, \quad (5.13a)$$

$$\mathbf{J}_p = n\mu_p \nabla E_{F,p}, \quad (5.13b)$$

The drift-diffusion current relations consider position dependent band edge energies, $E_C(\mathbf{r})$ for the conduction band and $E_V(\mathbf{r})$ for the valence band, and position dependent effective masses, which are included in the effective density of states N_C for the electrons and N_V for the holes, can be expressed as [183, 184]

$$\mathbf{J}_n = qn\mu_n \left(\nabla \left(\frac{E_C}{q} - V \right) + V_T \left(\frac{N_C}{n} \right) \nabla \left(\frac{n}{N_C} \right) \right), \quad (5.14a)$$

$$\mathbf{J}_p = qp\mu_p \left(\nabla \left(\frac{E_V}{q} - V \right) - V_T \left(\frac{N_V}{p} \right) \nabla \left(\frac{p}{N_V} \right) \right). \quad (5.14b)$$

5.2 Spin Transport Equations

If the spin degree of freedom of the electrons and the holes is considered, one can write the same set of transport equations (as was mentioned in the section 5.1) for the corresponding up(down)-spin in silicon [173, 174, 134]. In this work the analysis for only the electron spin is discussed, as the analysis for the holes can be performed in an analogous way. Thus, the acceptor doping is neglected and the Poisson equation Equation 5.1 can be rewritten as

$$\nabla \cdot \tilde{\epsilon} \cdot \nabla V = q(n_\uparrow + n_\downarrow - N_D), \quad (5.15)$$

where the up(down)-spin concentration is expressed as $n_\uparrow(n_\downarrow)$. The electron concentration n and the spin density s can be expressed as

$$n = n_\uparrow + n_\downarrow, \quad (5.16a)$$

$$s = n_\uparrow - n_\downarrow. \quad (5.16b)$$

5.2.1 Spin Continuity Equation

The continuity equations for the up(down)-spin electrons in the channel including the spin-flip term [173] is revealed below. An additional electron generation-recombination process can be neglected because the considered system is n -doped only (unipolar).

$$\frac{1}{q} \nabla \cdot \mathbf{J}_\uparrow - \frac{\delta n_\uparrow}{\tau_{\uparrow\downarrow}} + \frac{\delta n_\downarrow}{\tau_{\downarrow\uparrow}} = \frac{\partial \delta n_\uparrow}{\partial t}, \quad (5.17a)$$

$$\frac{1}{q} \nabla \cdot \mathbf{J}_\downarrow - \frac{\delta n_\downarrow}{\tau_{\downarrow\uparrow}} + \frac{\delta n_\uparrow}{\tau_{\uparrow\downarrow}} = \frac{\partial \delta n_\downarrow}{\partial t}. \quad (5.17b)$$

Here, $\mathbf{J}_\uparrow(\mathbf{J}_\downarrow)$ represents the up(down)-spin current density, $\tau_{\uparrow\downarrow}^{-1}$ is the rate at which up-spin flips to down-spin, and $\tau_{\downarrow\uparrow}^{-1}$ is the rate at which down-spin flips to up-spin.

δn_{\uparrow} (δn_{\downarrow}) represents the up(down)-spin density deviation from its thermal equilibrium value, denoted by n_{\uparrow}^{eq} (n_{\downarrow}^{eq}).

The structure under scrutiny consists of a ferromagnetic semiconductor (FMS), which inherently has an effective spin polarization, sharing a junction with silicon which does not. Therefore, one must introduce a non-zero bulk spin polarization P in the FMS. The total electron concentration at the thermal equilibrium is $n = N_D$ by considering all the dopants to be ionized. The equilibrium up(down)-spin concentration can thus be expressed as $n_{\uparrow(\downarrow)}^{eq} = 0.5(1 + (-)P)N_D$ in the FMS, and $n_{\uparrow(\downarrow)}^{eq} = 0.5N_D$ in Si. Then the up(down)-spin and the total spin density deviation (δs) can be expressed as

$$\delta n_{\uparrow} = n_{\uparrow} - n_{\uparrow}^{eq}, \quad (5.18a)$$

$$\delta n_{\downarrow} = n_{\downarrow} - n_{\downarrow}^{eq}, \quad (5.18b)$$

$$\delta s = \delta n_{\uparrow} - \delta n_{\downarrow}. \quad (5.18c)$$

The expressions for the electron (carrier) current density (\mathbf{J}_n) and the spin current density (\mathbf{J}_s) are given by [173]

$$\mathbf{J}_n = \mathbf{J}_{\uparrow} + \mathbf{J}_{\downarrow}, \quad (5.19a)$$

$$\mathbf{J}_s = \mathbf{J}_{\uparrow} - \mathbf{J}_{\downarrow}, \quad (5.19b)$$

One can relate the spin-flip rates $\tau_{\uparrow\downarrow}^{-1}$ and $\tau_{\downarrow\uparrow}^{-1}$ with the total spin relaxation time by using the Matthiessen rule

$$\tau_s^{-1} = \tau_{\uparrow\downarrow}^{-1} + \tau_{\downarrow\uparrow}^{-1}. \quad (5.20)$$

The continuity equation for the spin current density is obtained by subtracting Equation 5.17b from Equation 5.17a and can be expressed as

$$\frac{1}{q} \nabla \cdot \mathbf{J}_s - \frac{\delta s}{\tau_s} = \frac{\partial \delta s}{\partial t}. \quad (5.21)$$

5.2.2 Spin Drift-Diffusion

In accordance with Equation 5.14a, the up(down)-spin current density can be expressed as

$$\mathbf{J}_{\uparrow} = qn_{\uparrow}\mu_{\uparrow}\nabla\left(\frac{E_{C,\uparrow}}{q} - V\right) + qD_{\uparrow}N_C\nabla\left(\frac{\delta n_{\uparrow}}{N_C}\right), \quad (5.22a)$$

$$\mathbf{J}_{\downarrow} = qn_{\downarrow}\mu_{\downarrow}\nabla\left(\frac{E_{C,\downarrow}}{q} - V\right) + qD_{\downarrow}N_C\nabla\left(\frac{\delta n_{\downarrow}}{N_C}\right). \quad (5.22b)$$

Here, the up(down)-spin diffusion coefficient is D_{\uparrow} (D_{\downarrow}), and the corresponding mobility is μ_{\uparrow} (μ_{\downarrow}). These are related by $D_{\uparrow} = V_T\mu_{\uparrow}$ ($D_{\downarrow} = V_T\mu_{\downarrow}$). $E_{C,\uparrow}$ ($E_{C,\downarrow}$) represents the conduction band edge for the up(down)-spin.

5.2.3 Discretized Form

In order to discretize the in general multi-dimensional transport equations the following steps are used.

Poisson Equation

To solve the partial differential equations numerically, they must be discretized. For that reason, the domain \mathcal{V} where the equations are posed has to be partitioned into a finite number of sub-domains \mathcal{V}_i , which are usually obtained by a Voronoi tessellation. In order to obtain the solution with a desired accuracy, the equation system is approximated in each of these sub-domains by algebraic equations. The unknowns of this system are approximations of the continuous solutions at the discrete grid points in the domain [182]. It has been found to be advantageous to apply the finite boxes discretization scheme for semiconductor device simulation [182] [185]. This method considers the integral form of the equation for each sub-domain, which is the so-called control volume \mathcal{V}_i associated with the node the point i .

One can rewrite the Poisson equation (c.f. Equation 5.15) by using the Gauss' integral theorem.

$$\begin{aligned} \int_{\mathcal{V}} \nabla \cdot (\tilde{\epsilon} \nabla V) d\tilde{V} &= \int_{\mathcal{V}} q(n - N_D) d\tilde{V}, \\ \int_{\partial\mathcal{V}} (\tilde{\epsilon} \nabla V) \cdot \hat{\mathbf{n}} d\tilde{A} &= \int_{\mathcal{V}} q(n - N_D) d\tilde{V}. \end{aligned} \quad (5.23)$$

where $\hat{\mathbf{n}}$ is the outward pointing local normal vector of the enclosing surface \tilde{A} .

Finally, the discretized equation for point i with neighbor points j can be written implicitly as

$$\sum_{j \in N_i} -\tilde{\epsilon}_{ij} \left(\frac{V_j - V_i}{d_{i,j}} \right) A_{i,j} = q(n_i - N_{D,i}) \tilde{V}_i, \quad (5.24)$$

where $V_i(V_j)$ is the potential at the $i^{th}(j^{th})$ node, $N_{D,i}$ is the doping at the i^{th} node, $d_{i,j}$ is the distance between i^{th} and j^{th} node points, and $A_{i,j}$ is the interface area between the domains \mathcal{V}_i and \mathcal{V}_j . \tilde{V}_i is the volume of the domain \mathcal{V}_i . For a position dependent permittivity, one can use an average, e.g. $\tilde{\epsilon}_{ij} = \frac{\tilde{\epsilon}_i + \tilde{\epsilon}_j}{2}$, where $\tilde{\epsilon}_i$ ($\tilde{\epsilon}_j$) is the permittivity at the node point i (j).

A two-dimensional realization of the above mentioned box integration process can be found in Figure 5.1. In this case, \tilde{V}_i represents the area surrounding the i^{th} node, $d_{i,j}$ represents the distance between i^{th} and an adjacent j^{th} node point, and $A_{i,j}$ is the interface length as shown.

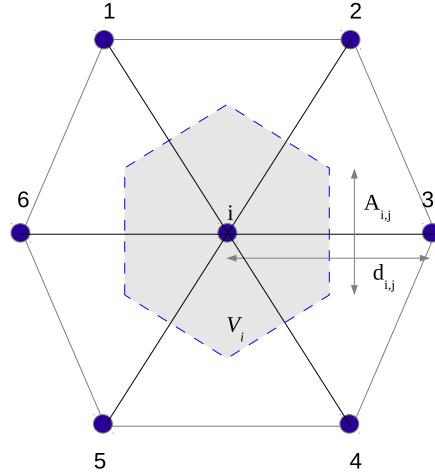


Figure 5.1: The two-dimensional representation of the Voronoi box is shown. The domain \tilde{V}_i contains the mesh point i and is surrounded by six adjacent mesh points. $A_{i,j}$ represents the boundary between the box around the i^{th} node and its neighbor j . $d_{i,j}$ implies the distance between the i^{th} and the j^{th} nodes.

Spin Continuity Equation

One can also apply the Gauss' integral theorem to rewrite the continuity equations Equation 5.17a and Equation 5.17b. If steady-state analysis is under investigation, $\frac{\partial n_{\uparrow(\downarrow)}}{\partial t} = 0$. Again, in order to derive a rather simplified analytical solution for the spin density later in this chapter to make comparisons with the simulated results, $\tau_{\uparrow\downarrow} = \tau_{\downarrow\uparrow} = 2\tau_s$ is considered (c.f. Equation 5.20). Because each spin flip contributes to relaxation of both up- and down-spin, the spin relaxation becomes twice as fast.

$$\begin{aligned} \int_{\mathcal{V}} (\nabla \cdot \mathbf{J}_{\uparrow}) d\tilde{V} &= q \int_{\mathcal{V}} \left(\frac{\delta n_{\uparrow} - \delta n_{\downarrow}}{2\tau_s} \right) d\tilde{V}, \\ \int_{\partial\mathcal{V}} (\mathbf{J}_{\uparrow} \cdot \hat{\mathbf{n}}) d\tilde{A} &= q \int_{\mathcal{V}} \left(\frac{\delta n_{\uparrow} - \delta n_{\downarrow}}{2\tau_s} \right) d\tilde{V}. \end{aligned} \quad (5.25a)$$

$$\begin{aligned} \int_{\mathcal{V}} (\nabla \cdot \mathbf{J}_{\downarrow}) d\tilde{V} &= q \int_{\mathcal{V}} \left(\frac{\delta n_{\downarrow} - \delta n_{\uparrow}}{2\tau_s} \right) d\tilde{V}, \\ \int_{\partial\mathcal{V}} (\mathbf{J}_{\downarrow} \cdot \hat{\mathbf{n}}) d\tilde{A} &= q \int_{\mathcal{V}} \left(\frac{\delta n_{\downarrow} - \delta n_{\uparrow}}{2\tau_s} \right) d\tilde{V}. \end{aligned} \quad (5.25b)$$

Then, considering the same Voronoi box around the i^{th} node,

$$\sum_{j \in N_i} J_{\uparrow,i,j} A_{i,j} = q \left(\frac{\delta n_{\uparrow,i} - \delta n_{\downarrow,i}}{2\tau_s} \right) \tilde{V}_i, \quad (5.26a)$$

$$\sum_{j \in N_i} J_{\downarrow,i,j} A_{i,j} = -q \left(\frac{\delta n_{\uparrow,i} - \delta n_{\downarrow,i}}{2\tau_s} \right) \tilde{V}_i. \quad (5.26b)$$

Here, $J_{\uparrow,i,j}$ ($J_{\downarrow,i,j}$) represents the up(down)-spin current density flowing from i^{th} to j^{th} node. $\delta n_{\uparrow,i}$ ($\delta n_{\downarrow,i}$) represents the up(down)-spin density deviation at the i^{th} node.

Spin Drift-Diffusion

The Scharfetter-Gummel (SG) discretization scheme for the carrier current density provides an optimum way to discretize the drift-diffusion equation for particle transport [186]. This discretization scheme can be applied as well to rewrite the expression for the up(down)-spin current densities (c.f. Equation 5.22a and Equation 5.22b) into their discretized form. One can discretize the spin drift-diffusion equations by following the steps as explained in [187, 183]. In the non-degenerate transport regime, the diffusion constant, the mobility, and the conduction band edge are spin-independent [174]. Therefore, $D_{\uparrow} = D_{\downarrow}$, $\mu_{\uparrow} = \mu_{\downarrow}$, and $E_{C,\uparrow} = E_{C,\downarrow}$. For simplicity one can assume a homogeneous position-independent electronic conduction band edge in the channel. Again, the bulk spin polarization P term can be inserted in the SG discretization scheme via the expressions of n_{\uparrow}^{eq} and n_{\downarrow}^{eq} .

$$J_{\uparrow,i,j} = \frac{q\bar{\mu}_{n,i,j}V_T}{d_{i,j}} (n_{\uparrow,j}B(\Delta_{i,j}^{(1)}) - n_{\uparrow,i}B(-\Delta_{i,j}^{(1)})) - \left(\frac{q\bar{\mu}_{n,i,j}V_T}{d_{i,j}} \right) (0.5\bar{N}_{D,i,j})(P_j - P_i), \quad (5.27a)$$

$$J_{\downarrow,i,j} = \frac{q\bar{\mu}_{n,i,j}V_T}{d_{i,j}} (n_{\downarrow,j}B(\Delta_{i,j}^{(1)}) - n_{\downarrow,i}B(-\Delta_{i,j}^{(1)})) - \left(\frac{q\bar{\mu}_{n,i,j}V_T}{d_{i,j}} \right) (0.5\bar{N}_{D,i,j})(P_j - P_i), \quad (5.27b)$$

with

$$\Delta_{i,j}^{(1)} = \Delta_{i,j} + \ln \left(\frac{N_{c,i}}{N_{c,j}} \right), \quad (5.28a)$$

$$\Delta_{i,j} = \frac{V_j - V_i}{V_T}. \quad (5.28b)$$

Here, P_i is the bulk spin polarization at the i^{th} node ($=P$ for the FMS, $=0$ for silicon), $\bar{\mu}_{n,i,j}$ represents the average mobility between i^{th} and j^{th} node, and a good approximation is $\bar{\mu}_{n,i,j} = \frac{\mu_{n,i} + \mu_{n,j}}{2}$. The effective density of states of electrons (N_C) in i^{th} (j^{th}) node is represented as $N_{c,i}$ ($N_{c,j}$). The average equilibrium electron concentration (i.e. the donor concentration) between two neighboring points i and j is represented by $\bar{N}_{D,i,j}$, and thus the average equilibrium up(down)-spin concentration

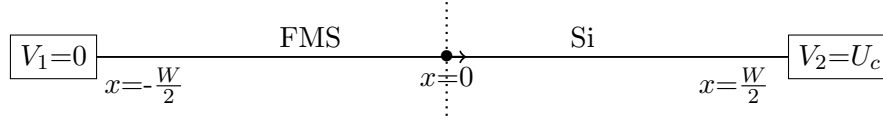


Figure 5.2: The schematic shows the simulation set up for the spin injection in Si from a ferromagnetic semiconductor (FMS). The left boundary ($x = -\frac{W}{2}$) is grounded, and the right boundary ($x = \frac{W}{2}$) is under the voltage bias (U_c). The interface is shown as a dotted line. The doping (effective density of states) in the Si side is N_D (N_C), and in the FMS is $K_1 N_D$ ($K_2 N_C$).

can be considered as $0.5\bar{N}_{D,i,j}$. The expression for the term $\bar{N}_{D,i,j}$ is described in the next section. B denotes the Bernoulli function

$$B(x) = \frac{x}{\exp(x) - 1}. \quad (5.29)$$

When spin transport only in a silicon bar is considered, the electron density of states N_C becomes position-independent, and thus $\Delta_{i,j}^{(1)} = \Delta_{i,j}$.

5.2.4 Transport Channel

In order to predict the impact of a space-charge layer on the spin transport in silicon, a one-dimensional transport channel is assumed. However, the same predictions will be valid for a multi-dimensional structure as well. The semiconducting channel of length W contains a semiconductor ferromagnet (FMS, $-\frac{W}{2} < x < 0$) and silicon (Si, $0 < x < \frac{W}{2}$), sharing a junction at $x=0$ (c.f. Figure 5.2). Now, to enable a violated or restored charge neutral source of spin injection in silicon, the following two assumptions are under consideration in this work.

- The ferromagnetic semiconductor FMS can be considered to be doped to a concentration, which is a factor K_1 of the value in Si. Thus, when $K_1 > 1$ ($K_1 < 1$), one can introduce a charge accumulated (depleted) source of spin injection into Si (c.f. text in Figure 5.2). Indeed when $K_1 = 1$, the charge neutrality condition is restored.
- One can consider a homogeneous electronic density of states in the FMS, which is a factor K_2 of the homogeneous density of states in Si. Thus, when $K_2 > 1$ ($K_2 < 1$), one can introduce a charge depleted (accumulated) source of spin injection into Si.

For a one-dimensional channel $\tilde{V}_i = \frac{d_{i,i-1} + d_{i,i+1}}{2}$, where $d_{i,j}$ is the distance between i^{th} and j^{th} nodes, and $A_{i,j} = 1$. As the space-charge effect on the spin transport is under scrutiny the charge screening length, also known as the Debye length (λ_D), puts a strict limitation on the choice of the mesh size near the interface in both the ferromagnetic and silicon sides [188]. The Debye length relates to the measure of a charge

carrier's net electrostatic effect, and it is the length over which the carrier density in a semiconductor changes by a factor $\frac{1}{q}$ [189]. λ_D in an n -doped semiconductor can be expressed as

$$\lambda_D = \sqrt{\frac{\epsilon_{Si} V_T}{q N_D}}, \quad (5.30)$$

where ϵ_{Si} is the silicon permittivity. The value of λ_D is 40nm for the parameters listed in Table 5.1. Thus, a good approximation is to use a step value (i.e. $d_{i,j}$) of 10nm near the interface in this particular simulation set up. In such a case, the node points i and j are close enough and $\bar{N}_{D,i,j} = \frac{N_{D,i} + N_{D,j}}{2}$ can be considered. The mobility is assumed to be homogeneous in the channel.

5.3 Solution

5.3.1 Solution with Charge Neutrality Constraint

Analytical Approach

When the charge current flows through the interface, the spin accumulation in the semiconductor appears. When $K_1=K_2=1$ (c.f. Table 5.1), the charge neutrality is restored. To solve the spin transport equations analytically for the structure shown in Figure 5.2, the general solution for the spin density deviation δs in both the FMS and the Si sides must be assumed according to [173, 190]

$$\delta s^{FMS} = a_1 N_D \exp\left(\frac{-x - \frac{W}{2}}{L_d}\right) + a_2 N_D \exp\left(\frac{x + \frac{W}{2}}{L_u}\right), \quad (5.31a)$$

$$\delta s^{Si} = b_1 N_D \exp\left(\frac{-x - \frac{W}{2}}{L_d}\right) + b_2 N_D \exp\left(\frac{x + \frac{W}{2}}{L_u}\right), \quad (5.31b)$$

Parameters	Values
Electron mobility in Si	$\mu_n=1400\text{cm}^{-2}\text{V}^{-1}\text{s}^{-1}$ [50]
Donor doping in Si	$N_D=10^{16}\text{cm}^{-3}$
Intrinsic spin diffusion length	$L_i=1\mu\text{m}$ [181]
Temperature	$T=300\text{K}$
Doping ratio between the ferromagnetic semiconductor and Si	K_1
Ratio between the electronic density of states among the ferromagnetic semiconductor and Si	K_2

Table 5.1: The simulation parameters for the spin drift-diffusion equations are listed.

where $a_1(a_2)$ and $b_1(b_2)$ are the constants. The spin density can be expressed as $s = \delta s + (n_{\uparrow}^{eq} - n_{\downarrow}^{eq})$ (c.f. Equation 5.18a to Equation 5.18c). The electron concentration is $n = N_D$. Based on these two, one can derive the up- and down-spin concentrations and the spin current density (\mathbf{J}_s) as well from Equation 5.22a and Equation 5.22b.

The external electric field (\tilde{E}) modifies the intrinsic spin diffusion length L_i in any semiconductor [173]. Two distinct spin diffusion lengths (L_u is the up-stream, and L_d is the down-stream) characterize the spin motion, and those strongly depend on \tilde{E}

$$L_u = \frac{1}{\frac{q|\tilde{E}|}{2K_B T} + \sqrt{\left(\frac{q|\tilde{E}|}{2K_B T}\right)^2 + \frac{1}{L_i^2}}}, \quad (5.32a)$$

$$L_d = \frac{1}{-\frac{q|\tilde{E}|}{2K_B T} + \sqrt{\left(\frac{q|\tilde{E}|}{2K_B T}\right)^2 + \frac{1}{L_i^2}}}, \quad (5.32b)$$

which is related to the intrinsic spin diffusion length L_i by

$$L_i^2 = L_u L_d. \quad (5.33)$$

L_i is related to the spin relaxation time via [173]

$$L_i = \sqrt{D_n \tau_s}. \quad (5.34)$$

In order to solve the transport equations, one can formulate the boundary conditions as elucidated below.

- In a doped semiconductor with homogeneous carrier concentration the up(down)-spin chemical potential [173, 174, 181], represented by M_{\uparrow} (M_{\downarrow}), is related to its concentration. The spin chemical potential remains continuous at the interface, hence [173]

$$\underbrace{\ln\left(\frac{n_{\uparrow}^{0-}}{0.5(1+P)N_D}\right)}_{\text{Chem. pot. (FMS)}} = \underbrace{\ln\left(\frac{n_{\uparrow}^{0+}}{0.5N_D}\right)}_{\text{Chem. pot. (Si)}} - \frac{G}{V_T}, \quad (5.35a)$$

$$\underbrace{\ln\left(\frac{n_{\downarrow}^{0-}}{0.5(1-P)N_D}\right)}_{\text{Chem. pot. (FMS)}} = \underbrace{\ln\left(\frac{n_{\downarrow}^{0+}}{0.5N_D}\right)}_{\text{Chem. pot. (Si)}} - \frac{G}{V_T}. \quad (5.35b)$$

Here, G is a constant describing as the spin chemical potential drop at the interface, and is responsible for spin injection from the FMS to the Si side. Therefore, G must depend on both the bulk spin polarization P and the electric field \tilde{E} .

- In the language of chemical potentials, the expression for the up(down)-spin current density can be reformulated as [173, 190]

$$J_{\uparrow} = q\mu_n n_{\uparrow} \frac{dM_{\uparrow}}{dx}, \quad (5.36a)$$

$$J_{\downarrow} = q\mu_n n_{\downarrow} \frac{dM_{\downarrow}}{dx}. \quad (5.36b)$$

As the up(down)-spin current density J_{\uparrow} (J_{\downarrow}) is continuous at the interface, the above equations yield to

$$q\mu_n n_{\uparrow}^{0-} \frac{dM_{\uparrow}^{0-}}{dx} = q\mu_n n_{\uparrow}^{0+} \frac{dM_{\uparrow}^{0+}}{dx}, \quad (5.37a)$$

$$q\mu_n n_{\downarrow}^{0-} \frac{dM_{\downarrow}^{0-}}{dx} = q\mu_n n_{\downarrow}^{0+} \frac{dM_{\downarrow}^{0+}}{dx}. \quad (5.37b)$$

- The spin density deviation δs is zero at the left and the right boundary, maintaining the thermal equilibrium. Hence,

$$\delta s\left(x = -\frac{W}{2}\right) = \delta s\left(x = \frac{W}{2}\right) = 0. \quad (5.38)$$

In order to derive the solution for the spin deviation and the spin current density, one must solve for 5 unknown parameters viz. a_1 , a_2 , b_1 , b_2 , and G . The spin injection efficiency can be formulated from two different approaches [173], one by the polarization of the spin current density (α) and the other by the polarization of the spin density (β)

$$\alpha = \frac{J_s}{J_n}, \quad (5.39)$$

$$\beta = \frac{s}{n}. \quad (5.40)$$

Therefore, at the junction, $\alpha_0 = \frac{J_s(0+)}{J_n}$ and $\beta_0 = \frac{s(0+)}{n(0+)}$.

The analytical expressions for α_0 and β_0 are cumbersome. The simplified expressions, valid for lower values of the bulk spin polarization P are [190]

$$\alpha_0 = P \frac{L_d}{L_d + (1 - P^2)L_u}, \quad (5.41)$$

$$\beta_0 = \left(1 - \frac{L_u}{L_d}\right) \alpha_0. \quad (5.42)$$

The expression for constant G is

$$G = V_T \ln(1 + \beta_0 P). \quad (5.43)$$

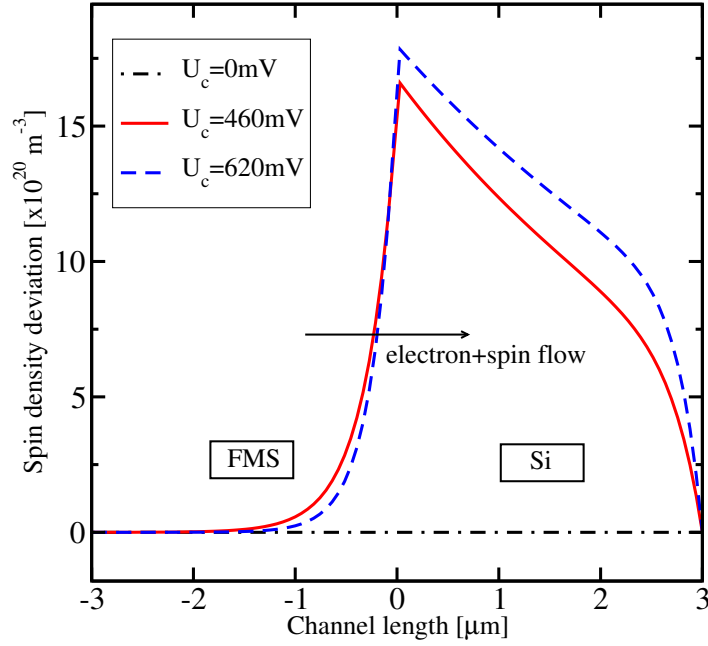


Figure 5.3: The analytically calculated spin densities in the channel are shown, when the applied voltage (U_c) is used as a parameter. The bulk spin polarization in the ferromagnetic semiconductor (FMS) is $P=20\%$.

Equation 5.42 indicates that α_0 is always larger than β_0 irrespective of the value of the applied field. If the electric field is very small, both the up- and down-spin diffusion lengths L_u and L_d tend to the intrinsic value and hence from Equation 5.41, $\alpha_0 \rightarrow \frac{P}{2-P^2}$. This also means $\beta_0=0$ and from Equation 5.43 $G=0$. At the strong field limit, the electrons move with the drift velocity and so does the spin polarization [173]. L_d is simply the distance over which the carriers move within the spin lifetime. Thus, when the electric field increases, $L_d \rightarrow (\frac{q|\tilde{E}|}{K_B T})L_i^2$, $L_u \rightarrow (\frac{K_B T}{q|\tilde{E}|})$ [173]. This makes the ratio $(\frac{L_u}{L_d}) \rightarrow 0$ as $\tilde{E} \rightarrow \infty$, and both α_0 and β_0 tend to reach a saturation value fixed by the bulk spin polarization P at the ferromagnetic semiconductor. The maximum and minimum values of the mentioned parameters are listed in Table 5.2. Therefore, for small values of P , the spin injection efficiency in Si can be predicted analytically.

Parameters	Minimum value	Maximum value
α_0	$\frac{P}{2-P^2}$	P
β_0	0	P
G	0	$V_T(1+P^2)$

Table 5.2: The spin injection parameters with their optimum values are shown.

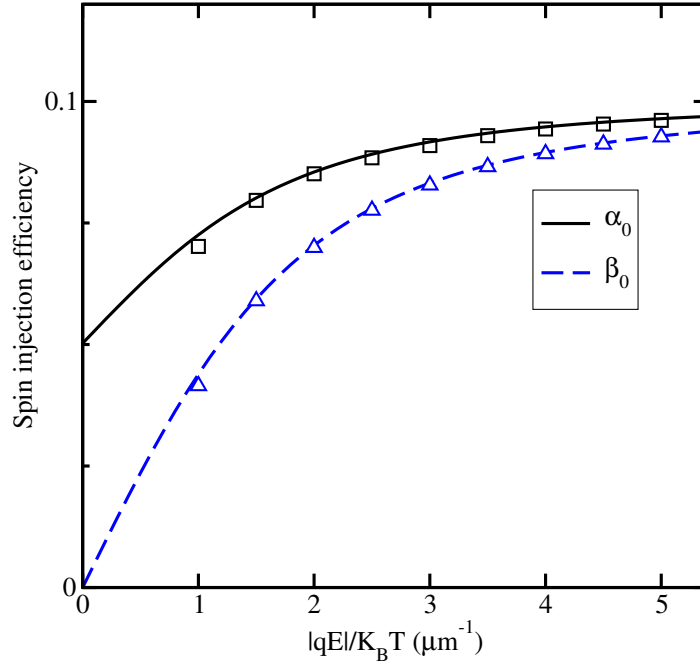


Figure 5.4: The spin current density (α_0) and spin density (β_0) injection efficiencies at the Si interface are shown as a function of the applied electric field \vec{E} . Lines \rightarrow theory and dots \rightarrow simulation ($P=10\%$).

Comparison between Analytical and Simulated Results

Figure 5.3 shows how spin piles up at the junction with the applied voltage U_c , when $K_1 = K_2=1$ (c.f. Table 5.1), and the bulk polarization P value is low ($P = 20\%$). The figure depicts how the applied bias improves the spin injection efficiency.

Even though for low values of bulk polarization P the analytical model for the spin current density (spin density) injection efficiency α_0 (β_0) is quite precise (c.f. Figure 5.4), as soon as the value of P increases the analytical solution is no longer accurate enough and the error increases significantly (c.f. Figure 5.5). Therefore, it is also important to solve the drift-diffusion equation set numerically to lift the restriction to high values of P . It is noted in Figure 5.5 that the α_0 and β_0 values remain upper limited by P . Nevertheless, once up(down)-spin concentration is calculated from the simulations, the spin chemical potential drop G (c.f. Equation 5.35a and Equation 5.35b) can be obtained as described in Figure 5.6.

5.3.2 Solutions without Charge Neutrality Constraint

By varying K_1 , K_2 (c.f. Table 5.1), one can remove the charge neutrality constraint. Charge injection to silicon or charge release always cause a non-zero current (hence the

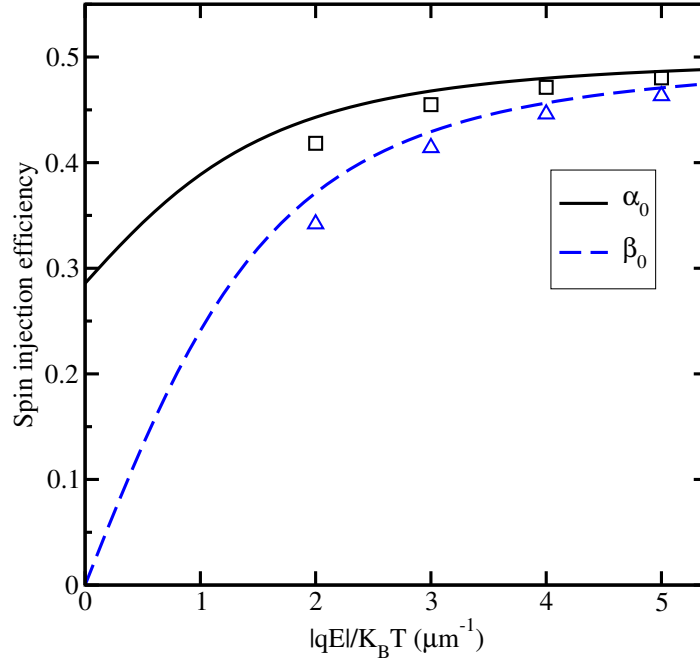


Figure 5.5: The spin current density (α_0) and spin density (β_0) injection efficiencies at the Si interface as a function of the applied electric field \vec{E} (c.f. Figure 5.4) is shown ($P=50\%$).

flow of charge) through the junction, even at the absence of an external electric field. This flow of charge causes spin accumulation/depletion at the junction. Therefore, using current as the external control parameter, rather than the applied voltage, is more convenient, because the current is always constant throughout the channel. On the other hand, if one uses voltage as the control parameter, one has to consider the potential profile in different parts of the conducting channel.

A constant current can be maintained in the channel by tuning the applied voltage U_c at certain values for K_1, K_2 . At a constant current the distribution for the spin density deviation, the spin current density, and also the potential profile are now analyzed. Strong nonlinear effects due to the conductivity variation in the space-charge layer close to the interface cause deviations of the compensating voltage, which has to be properly considered.

It is noticed that the spin density deviation δs behaves differently at the interface and in the bulk of silicon, c.f. Figure 5.7. When $K_1 > 1$, δs gradually piles up in the bulk FMS and drops down in the bulk silicon, compared to the charge neutrality condition. On the other hand when $K_1 < 1$, δs gradually drops down in the FMS bulk and piles up in the Si bulk. This phenomenon happens due to the differences in the material conductivities (proportional to the doping concentration) and the electric field \vec{E} at the bulk, which eventually alters the spin diffusion lengths both in the FMS and Si part of

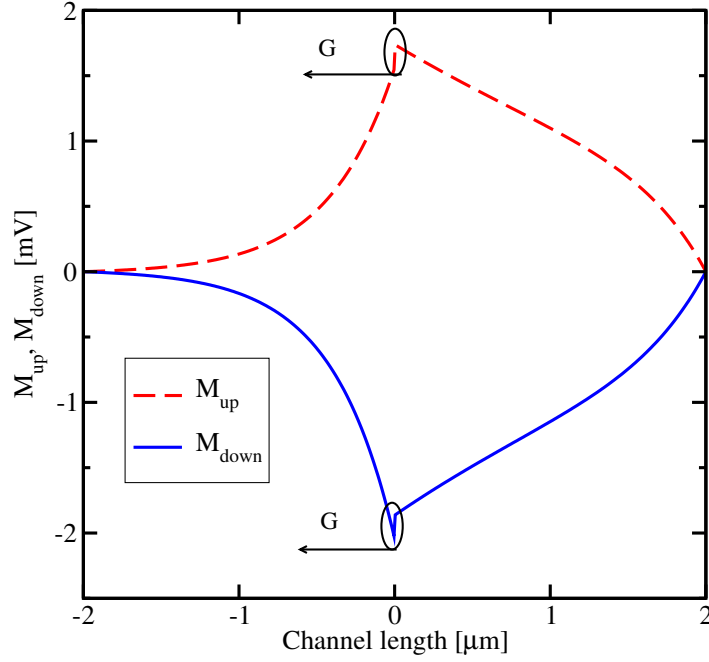


Figure 5.6: A plot of $M_{up} = V_T \ln \left(\frac{n_{\uparrow}}{n_{\uparrow}^{eq}} \right)$ and $M_{down} = V_T \ln \left(\frac{n_{\downarrow}}{n_{\downarrow}^{eq}} \right)$ through the bar ($P=10\%$, $\frac{|q\tilde{E}|}{K_B T} = 2 \mu\text{m}^{-1}$ where \tilde{E} is the applied electric field) is depicted, showing a discontinuity at the junction, which gives the term G (c.f. Equation 5.35a and Equation 5.35b). n_{\uparrow}^{eq} (n_{\downarrow}^{eq}) is the up(down)-spin concentration at the thermal equilibrium.

the channel. However, the behavior at the interface is noted to be completely different. When $K_1 > 1$ ($K_1 < 1$), δs develops a dip (peak) at the FMS interface followed by a sharp peak (dip) at Si interface. These features can be correlated with the presence of charge depletion (accumulation) at the ferromagnetic/nonmagnetic interface, which results in the formation of a potential profile with a barrier for electrons (c.f. Figure 5.8). Indeed, these interface effects give rise to a very small alteration in the spin current density J_s (particularly for $K_1 = 5$) as observed in Figure 5.9. Nonetheless, the interface effects only persist up to the classical charge screening length λ_D (c.f. Equation 5.30), and completely vanish beyond that limit.

In order to investigate if the alteration of K_2 has an additional effect on the observed results, one can look into Figure 5.10. It is observed that under the constraint $K_1 = K_2$ the charge neutrality condition is restored. This is the reason why the additional interface effects on the spin density deviation δs is noted to be absent compared to Figure 5.7. When $K_1 \neq K_2$, the charge neutrality condition is violated at the interface. It is noted that when $K_2 < 1$ ($K_2 > 1$), δs develops a sharp dip (peak) in the FMS side and sharp peak (dip) in the silicon side for $K_1 = 1$. However, Figure 5.10 also depicts

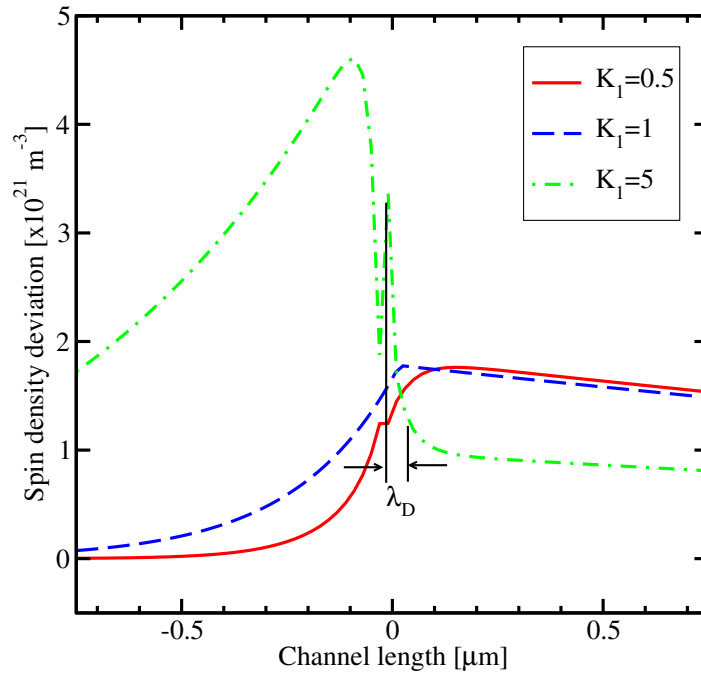


Figure 5.7: The spin density accumulation near the junction over a channel of $4\mu\text{m}$ is shown, when the current density (J_n) is fixed to $23.4\text{MA}/\text{m}^2$ with $P=20\%$. K_1 is used as a parameter (c.f. Table 5.1). λ_D represents the Debye length (c.f. Equation 5.30).

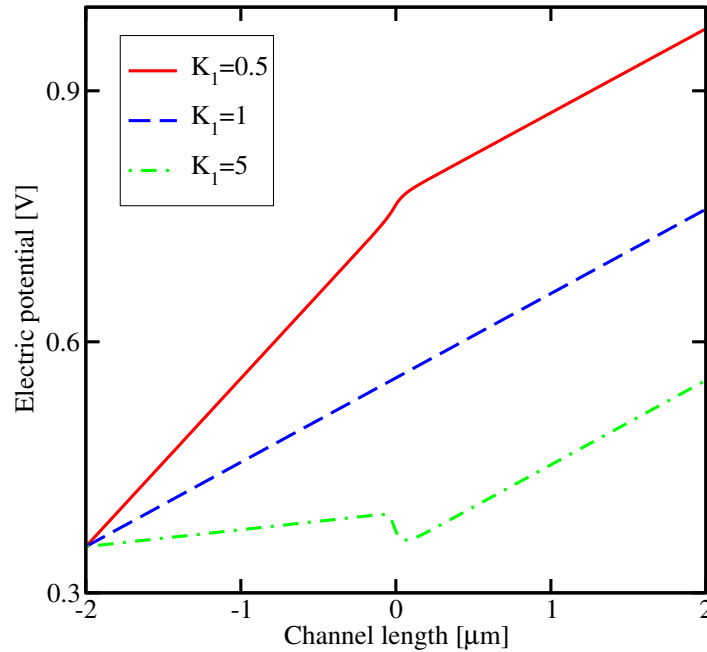


Figure 5.8: The variation of the electric potential through the channel is described, related to Figure 5.7.

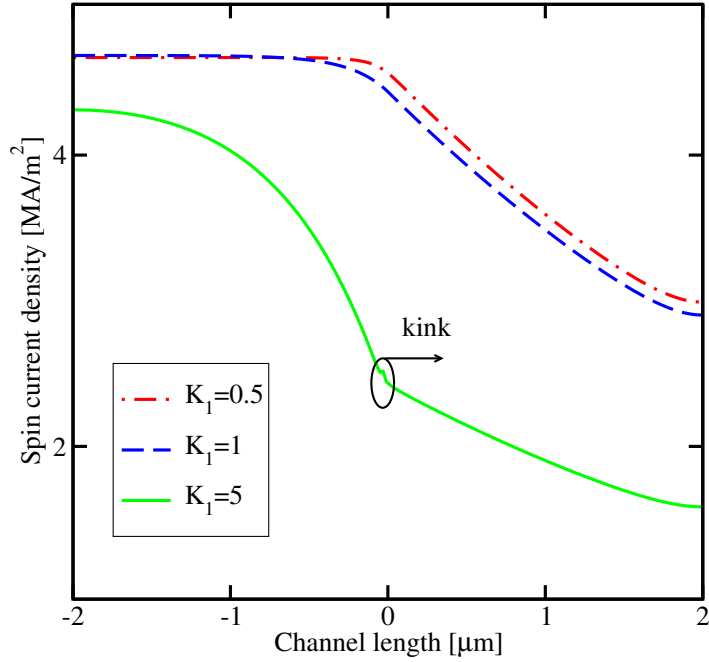


Figure 5.9: The spin current density through the channel is shown, with the same conditions as in Figure 5.7. With the notations as described in Equation 5.16b and Equation 5.19b, the direction of the spin current is from the ferromagnetic semiconductor FMS towards Si.

how the spin signal remains unaltered in the silicon bulk if the value of K_1 is kept fixed and the value of K_2 is varied. This confirms that the tuning of the parameter K_2 does not impact the bulk spin signal in silicon.

The estimated values of α_D and β_D , which are corresponding α and β at a distance λ_D away from the interface in silicon, are shown in Figure 5.11. It is revealed that α_D remains greater than β_D , and both are enhanced when spin is injected from a charge depleted ferromagnetic semiconductor compared to the charge neutral one. However, both α_D and β_D are always upper limited by the bulk spin polarization P .

5.4 Spin Diffusion from a Space-Charge Layer

Since the spin injection efficiency's upper limit is the polarization in the ferromagnetic semiconductor, one needs to further investigate the peculiarities of the spin signal in silicon if the spin is injected through only a charge neutral or space-charge layer. One can solve the same set of spin transport equations either by adjusting the up- and down-spin concentrations or up- and down-spin current densities at one of the boundaries (i.e. left boundary), to impose a charge-neutral; a charge-accumulated; and a charge depleted source. The schematic is shown in Figure 5.12.

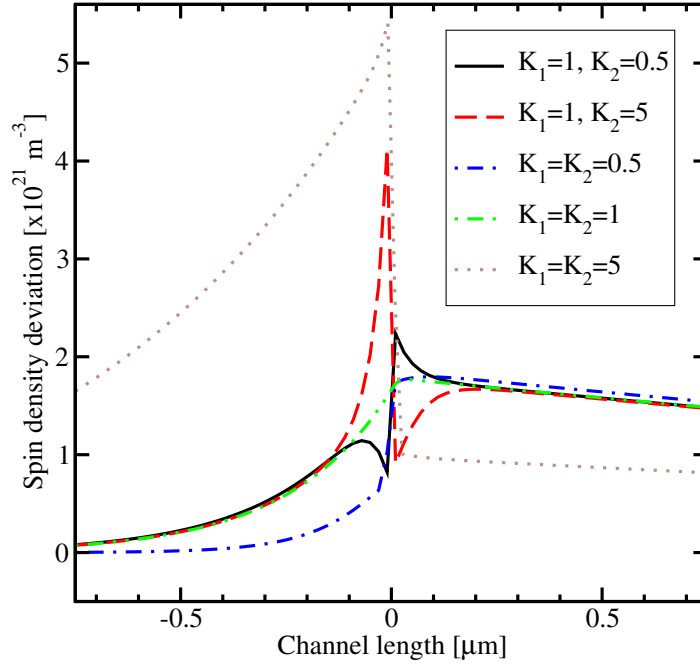


Figure 5.10: The spin density accumulation through the channel is depicted, with the same conditions as in Figure 5.7. Both K_1 and K_2 are used as parameters (c.f. Table 5.1).

5.4.1 Solution with Charge Neutrality Constraint

The general solution for the spin density in the bar (c.f. Figure 5.12) can be considered to be in the form [173]

$$s = A_1 \exp\left(\frac{-x}{L_d}\right) + A_2 \exp\left(\frac{x}{L_u}\right). \quad (5.44)$$

Here, the constants A_1 and A_2 are defined by the boundary conditions. One can fix the up(down)-spin concentrations $n_\uparrow(x=0) = n_{\uparrow 0}$, and $n_\downarrow(x=0) = n_{\downarrow 0}$ at the spin injection boundary. Then the corresponding electron concentration, the spin density, and the spin current density can be written as

$$n(x=0) = n_0 = n_{\uparrow 0} + n_{\downarrow 0}, \quad (5.45a)$$

$$s(x=0) = s_0 = n_{\uparrow 0} - n_{\downarrow 0}. \quad (5.45b)$$

$$J_s(x=0) = J_{s0} = J_{\uparrow 0} - J_{\downarrow 0}. \quad (5.45c)$$

The polarizations for the spin current density and the spin density at the injection boundary are $\alpha_0 = \frac{J_{s0}}{J_n}$ and $\beta_0 = \frac{s_0}{n_0}$ respectively. The channel length W is assumed to be several times larger than the intrinsic spin diffusion length L_i , thus one can suppose

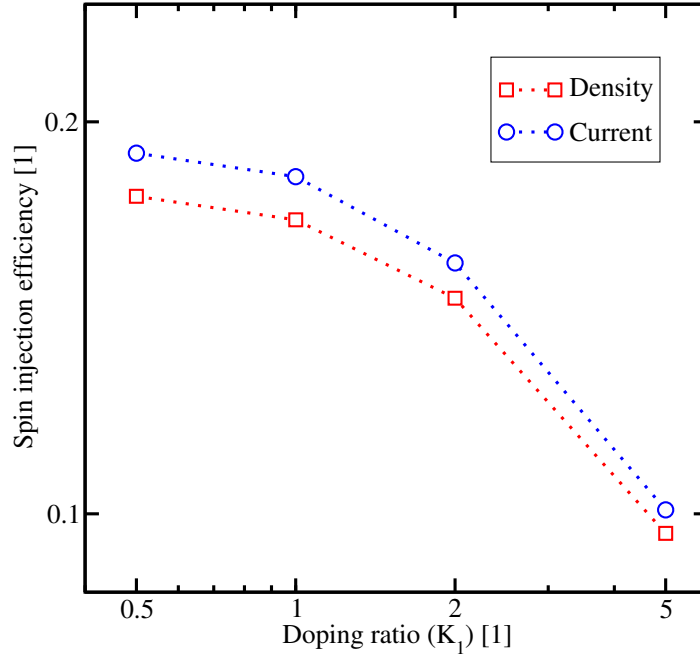


Figure 5.11: The spin density and the spin current density injection efficiencies (β_D and α_D respectively) are shown, taken at a Debye length away from the interface towards Si, with the same conditions as in Figure 5.7.

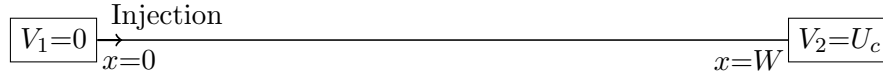


Figure 5.12: The schematic portrays the simulation set up for the spin injection in a Si bar. The left boundary ($x=0$) is grounded, and the right boundary ($x = W$) is under a voltage bias (U_c).

that the up(down)-spin is in thermodynamic equilibrium at the right boundary of the channel (i.e. $n_{\uparrow}(x = W) = n_{\downarrow}(x = W) = 0.5N_D$, $s(x = W) = 0$).

The expression for the spin current density can be obtained from Equation 5.22a and Equation 5.22b

$$J_s = \underbrace{qs\mu_n\tilde{E}}_{\text{spin drift}} + \underbrace{qD_n\frac{ds}{dx}}_{\text{spin diffusion}}. \quad (5.46)$$

Thus, by using Equation 5.44 one can write

$$J_s = q\mu_n\tilde{E} \left[\left(1 + \frac{V_T}{\tilde{E}L_u} \right) A_2 \exp\left(\frac{x}{L_u}\right) + \left(1 - \frac{V_T}{\tilde{E}L_d} \right) A_1 \exp\left(\frac{-x}{L_d}\right) \right]. \quad (5.47)$$

The spin density distribution s in the channel is shown in Figure 5.13, with the parameters as listed in Table 5.1. When the applied bias is positive (negative), the electric

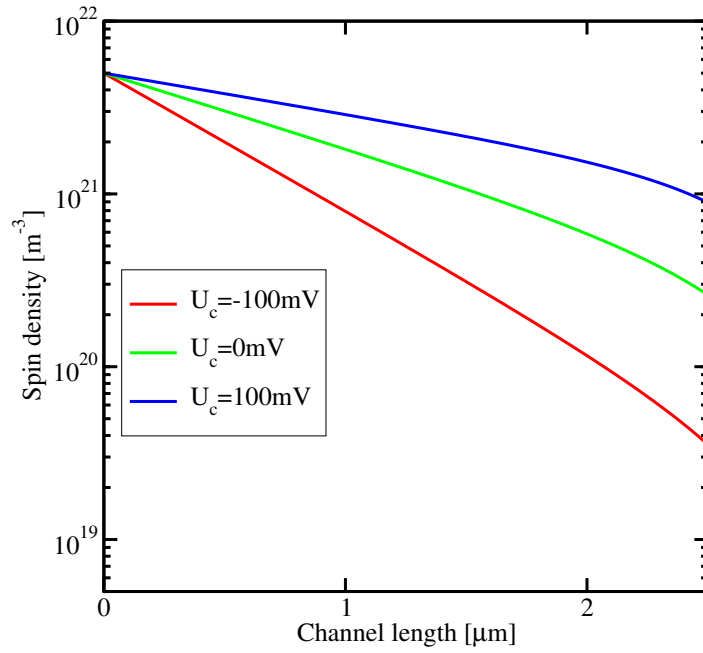


Figure 5.13: The analytically (c.f. Equation 5.44) calculated spin densities through the channel are shown. The boundary spin density polarization $\beta_0=50\%$. The channel length is $3\mu\text{m}$.

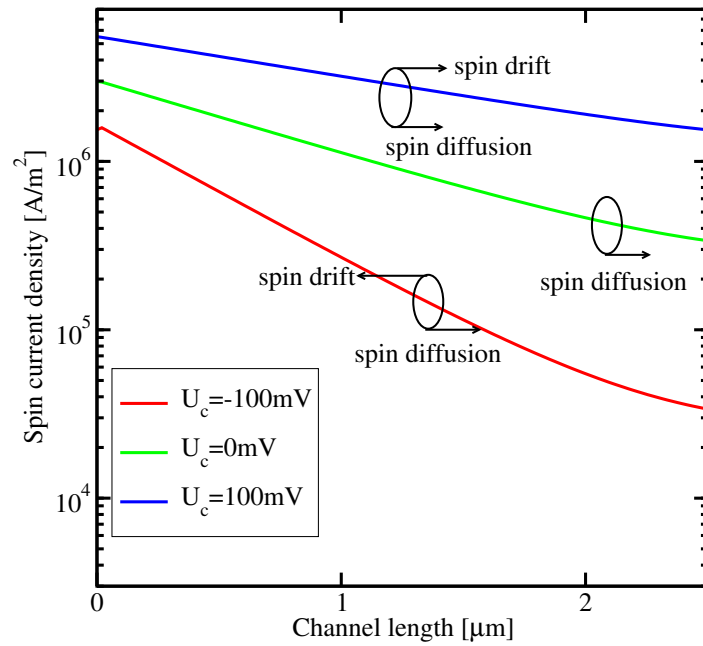


Figure 5.14: The analytically (c.f. Equation 5.47) calculated spin current densities are shown, corresponding to Figure 5.13. The directions of the drift and the diffusive components of the spin current density are highlighted.

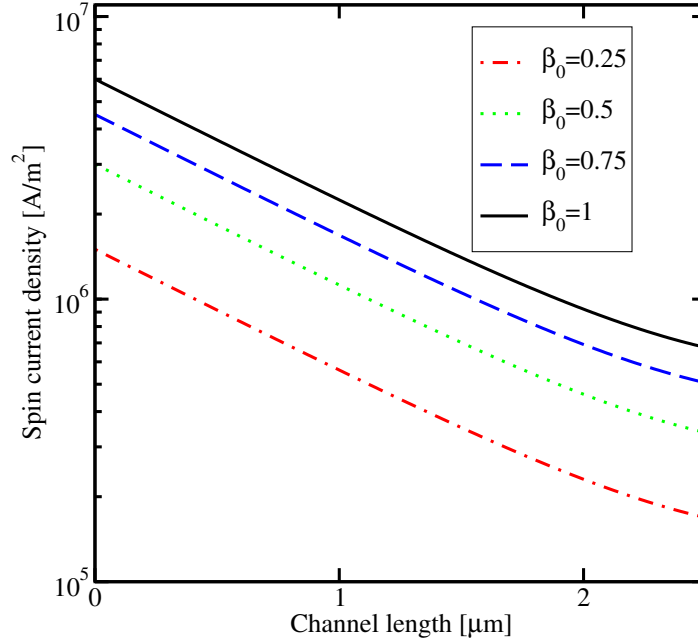


Figure 5.15: The variation of the spin current density in the channel with the boundary spin density polarization β_0 is shown, when no voltage is applied.

field increases (decreases) the effective spin diffusion length [173]. This is why the signal s is high in the channel when $U_c > 0$. For the same conditions, the spin current density J_s through the channel is shown in Figure 5.14. With the notations as described in Equation 5.16b and Equation 5.19b, the direction of the spin current is towards the positive x -axis (c.f. Figure 5.12). The figure also depicts the direction of the drift and diffusion components of J_s , and it is observed that J_s is higher when the spin flow is in the direction of the electron (charge) flow (i.e. $U_c > 0$). In contrast to Figure 5.3 one observes the non-vanishing value of s (and hence J_s) in the channel even when $U_c = 0$. This signifies that the spin flow due to its diffusive component is still possible in this structure, even when \vec{E} is absent.

Figure 5.15 examines the variation of the spin current density J_s for different values of the spin density polarization at the injecting point (β_0), when no voltage is applied (i.e. $U_c = 0$, and thus the carrier current is absent). J_s through the channel increases with β_0 proportionally, reaching its maximum when β_0 is maximum (i.e. $\beta_0 = 1$). Thus from the above discussions it is confirmed that the spin behavior is completely decoupled from charge, and the spin diffusion lengths (L_u and L_d) are solely determined by the intrinsic spin diffusion length L_i and the electric field \vec{E} .

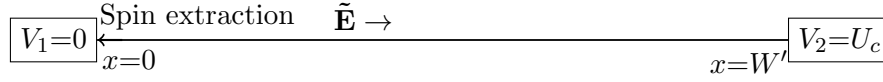


Figure 5.16: The schematic depicts the spin extraction phenomenon from the Si bar towards the left boundary ($x=0$). The left boundary is under zero-bias, and the right boundary ($x = W'$, where $W' \gg L_i$ with L_i as the intrinsic spin diffusion length) is under a negative bias ($U_c < 0$). The direction of the electric field is also shown.

Spin Extraction and Critical Current Density

A functional spintronic device also involves the reverse process of spin injection, i.e. the extraction of spin-polarized electrons from the semiconductor to a ferromagnetic structure. One can investigate spin extraction from a non-magnetic semiconductor like silicon into the ferromagnet in the regime where the degree of spin polarization is very high. For the analysis of the spin extraction phenomenon, the detailed structure of the interface is not very important, and one can solve the spin transport equations for the semiconductor region instead [191]. The electrons, flowing from the silicon side and entering in the magnet, are supposed to be unpolarized. Now, if the structure is a ferromagnetic half-metal [103], then it accepts only one spin orientation (e.g. up-spin electrons). In such a case, a cloud of down-spin electrons is formed in silicon near the relevant boundary, as those can not enter in the ferromagnet unless undergoing a spin flip. The current in the bar increases the cloud, and eventually reaches its maximum, when the silicon region near the junction becomes completely depleted of the electrons with the same direction of spins (i.e. up-spins) as in the ferromagnet. This phenomenon is known as spin-blockade [191]. This signifies that a further increase of the steady-state current through the junction will not be possible.

In order to estimate this critical current density represented as $J_{c,cr}$, one can use the general solution of the spin density from Equation 5.44. The spin extraction scheme is portrayed in Figure 5.16. For the simplicity of analytical calculations one can assume the bar to be long enough to negate the impact of the right boundary. In such a case and for the structure as depicted in Figure 5.16, the up-stream diffusion length given by $L' = \frac{2V_T}{\tilde{E} + \sqrt{\tilde{E}^2 + \frac{4V_T}{\mu_n \tau_s}}}$ solely determines the transport [191]. Then, one can assume the spin density for the spin extraction model in the form of [191] $s = -A_1 \exp\left(\frac{-x}{L'}\right)$, where A_1 is a positive quantity. Then from Equation 5.46,

$$J_s = q\mu_n \tilde{E} \left[\left(1 - \frac{V_T}{\tilde{E}L'}\right) (-A_1) \exp\left(\frac{-x}{L'}\right) \right]. \quad (5.48)$$

Henceforth at the spin extraction boundary,

$$J_{s0} = -q\mu_n \tilde{E} \left[\left(1 - \frac{V_T}{\tilde{E}L'}\right) A_1 \right]. \quad (5.49)$$

The spin current density and the charge current density are related by

$$\begin{aligned} J_{s0} &= \alpha_0 \cdot J_n \\ &= \alpha_0 q \mu_n \tilde{E} N_D . \end{aligned} \quad (5.50)$$

Because the electric field \tilde{E} is homogeneous and linearly coupled to the total current density, it can be assumed that, the polarization for the spin current density α_0 is fixed by the ferromagnet and thus does not depend on the channel current. Then,

$$-q\mu_n \tilde{E} \left[\left(1 - \frac{V_T}{\tilde{E} L'} \right) A_1 \right] = \alpha_0 q \mu_n \tilde{E} N_D , \quad (5.51)$$

which eventually yields to

$$\left[\left(\frac{V_T}{\tilde{E} L'} - 1 \right) A_1 \right] = \alpha_0 N_D , \quad (5.52)$$

and therefore,

$$A_1 = \frac{\alpha_0 \tilde{E} N_D}{\frac{V_T}{L'} - \tilde{E}} . \quad (5.53)$$

If the expression for the up-stream diffusion length is put in Equation 5.53, A_1 can be estimated as $A_1 = \frac{2\alpha_0 N_D}{\sqrt{1 + \frac{4V_T}{\mu_n \tau_s \tilde{E}^2} - 1}}$. Since the maximum possible spin polarization can only be 100%, the maximum possible value for A_1 is the doping concentration N_D , and one can write

$$\tilde{E}^2 = \frac{V_T}{\alpha_0 \cdot (\alpha_0 + 1) \mu_n \tau_s} . \quad (5.54)$$

Finally, one can write the expression for the critical current density

$$\begin{aligned} J_{c,cr} &= q N_D \sqrt{\frac{\mu_n V_T}{\alpha_0 \cdot (\alpha_0 + 1) \tau_s}} \\ &= q N_D \cdot \left(\frac{D_n}{L_i} \right) \cdot (\alpha_0^2 + \alpha_0)^{-0.5} . \end{aligned} \quad (5.55)$$

A fully polarized (unpolarized) spin current pertains to $\alpha_0=1$ (0). In this range, $J_{c,cr}$ decreases with increasing α_0 . Equation 5.55 also reveals that spin-blockade of the current is more important in materials with long spin relaxation times (particularly Si), hence this phenomenon must be considered in order to design efficient silicon-based spintronic devices.

Figure 5.17 depicts the critical current density at the spin-blockade. $J_{c,cr}$ increases slowly by decreasing α_0 from 1 to around 0.3. Therefore, the spin-blockade phenomenon is also important in junctions with ordinary ferromagnets.

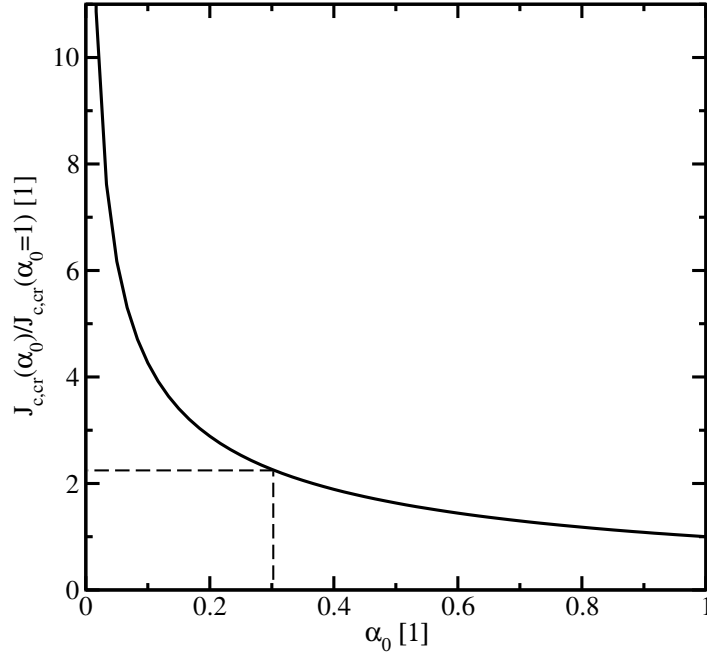


Figure 5.17: The normalized critical current density is shown for spin-blockade as a function of the boundary current density spin polarization.

5.4.2 Solution without Charge Neutrality Constraint

In order to lift the charge neutrality constraint, one can adjust the up(down)-spin concentrations $n_{\uparrow 0}$ and $n_{\downarrow 0}$ in such a manner that the net electron concentration at the left boundary $n_0 \neq N_D$. It is hereby mentioned that by tuning up- and down-spin current densities $J_{\uparrow 0}$ and $J_{\downarrow 0}$ one can lift the charge neutrality constraint as well. For simplicity of analysis the former method is adopted. One can fix the charge density with the single parameter M_{Ch} (this term can be attributed to the charge chemical potential) as given below.

$$M_{Ch} = V_T \ln \left(\frac{n_0}{N_D} \right). \quad (5.56)$$

Now, if the maximum value for the spin density polarization $\beta_0=1$ (i.e. $n_0=s_0$) is considered

$$\begin{bmatrix} n_{\uparrow 0} \\ n_{\downarrow 0} \end{bmatrix} = N_D \begin{bmatrix} \exp \left(\frac{M_{Ch}}{V_T} \right) \\ 0 \end{bmatrix}, \quad (5.57)$$

and thus making

$$M_{Ch} = V_T \ln \left(\frac{s_0}{N_D} \right). \quad (5.58)$$

Therefore, one can inject (release) up-spin and hence charge at the same time. This way it is possible to describe

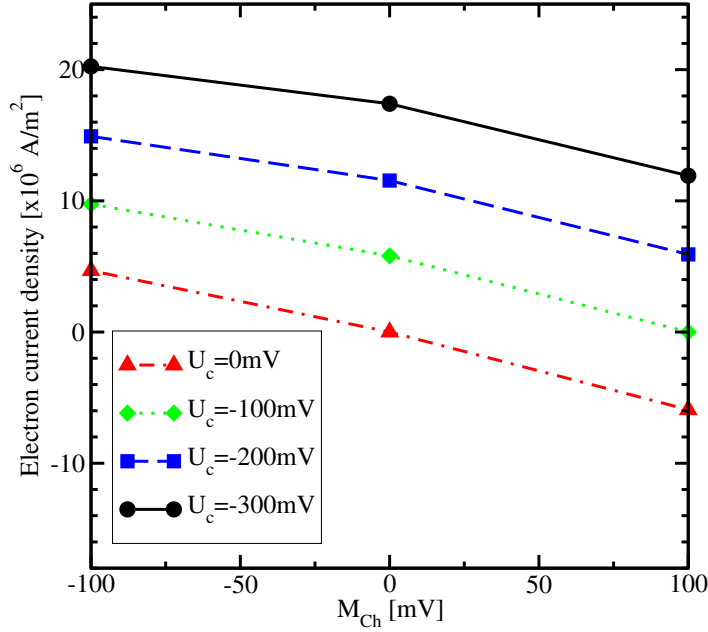


Figure 5.18: The variation of the electron current density with M_{Ch} (c.f. Equation 5.57) and the bias voltage U_c is depicted, when the channel length is $4\mu\text{m}$.

- spin injection from a charge accumulated source ($M_{Ch} > 0$),
- spin injection from a charge depleted source ($M_{Ch} < 0$),
- restore charge neutrality ($M_{Ch} = 0$).

Via Equation 5.57 a considerable spin and charge accumulation (depletion) at the interface can be introduced and spin will diffuse out of this region. Non-zero values of M_{Ch} always cause a flow of charge even though the applied voltage is zero. The carrier current density J_n , the spin density s , and the spin current density J_s in the channel can be tuned by varying both M_{Ch} and the applied voltage U_c . One can set any non-zero value for M_{Ch} and adjust U_c to keep a fixed charge flow ($J_n = \text{constant}$) in the channel as described in Figure 5.18.

Figure 5.19 depicts how the charge accumulation (depletion) causes the pile up (reduction) of the carriers near the left boundary and through the channel. As found previously, this pile up persists only up to the screening region characterized by the Debye length λ_D (c.f. Equation 5.30). The spin carriers follow a similar profile, which is shown in Figure 5.20 and illustrates that an abundance of spin carriers during the accumulation enhances the spin current density J_s only close to the interface, while in contrast a lack of spin carriers in depletion causes a very strong diminution of the same, both at the interface and the bulk. In order to complete the comparison, the charge neutrality condition is also shown. Figure 5.20 reveals that under charge accumulation J_s shows an upper threshold [181]. The amount of J_s which leaks from the

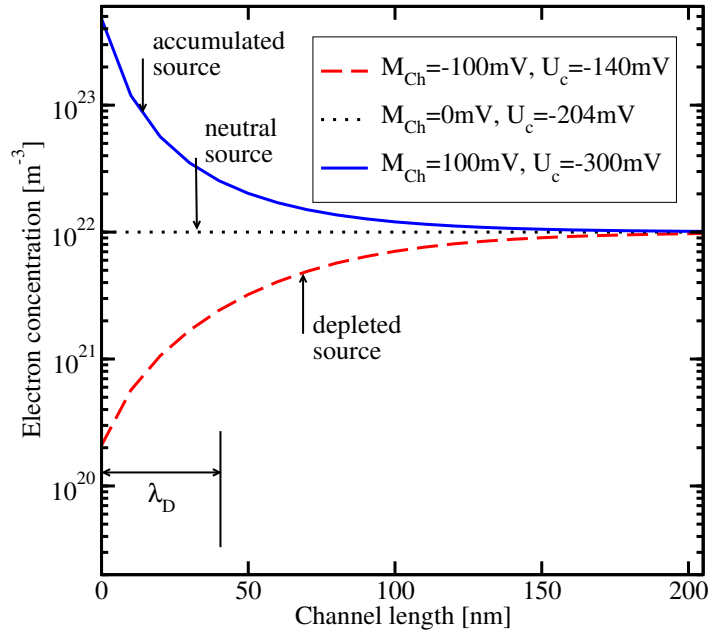


Figure 5.19: The electron concentration is shown near the charge injection boundary (c.f. Equation 5.57). The current density is 11.9MAm^{-2} , and the channel length $4 \mu\text{m}$. λ_D represents the Debye length.

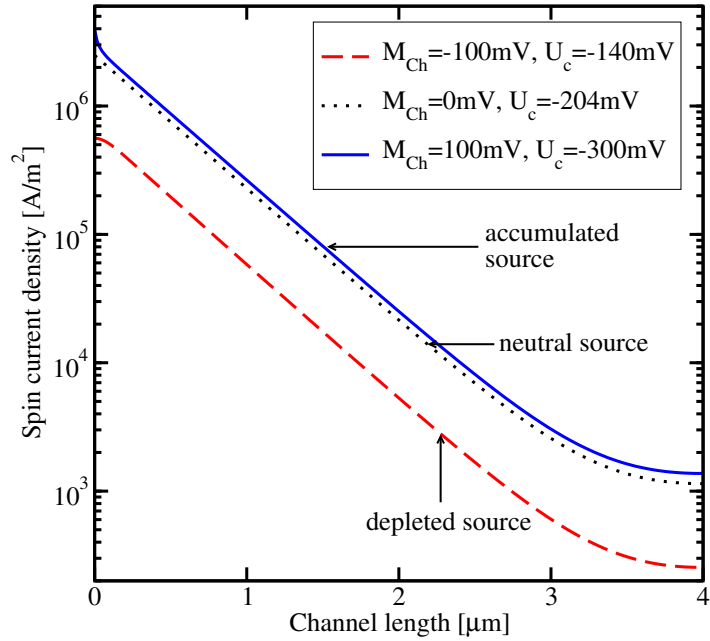


Figure 5.20: The variation of the spin current density is delineated with the same conditions as in Figure 5.19.

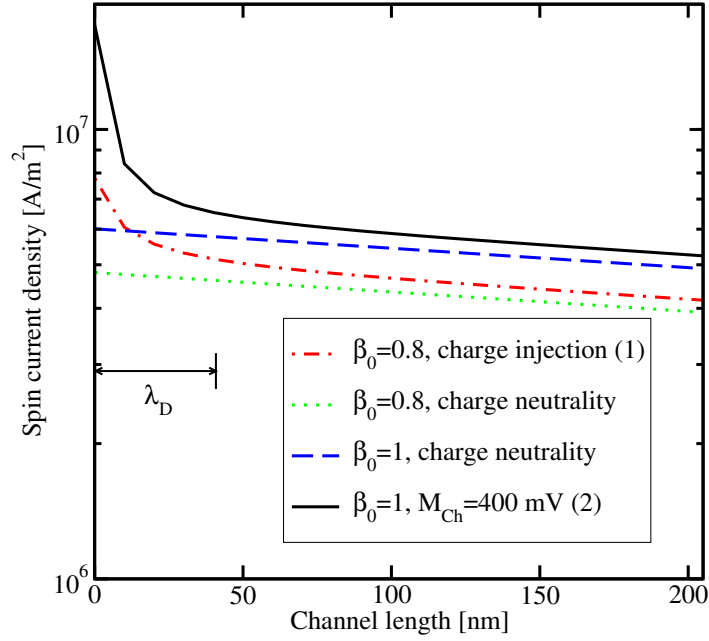


Figure 5.21: The spin current density is shown for up to 5 times the Debye length λ_D from the left boundary, when spin is injected from a charge neutral and charge accumulated source. The carrier current is absent. The left boundary for (1) is set with $n_{\uparrow 0}=900N_D$ and $n_{\downarrow 0}=100N_D$, and for (2) c.f. Equation 5.57.

accumulation region almost does not change in high accumulation, regardless of the high values of the spin density s and J_s near the interface. This means that an effort to boost J_s by increasing the boundary spin density s_0 to inject more spin polarized electrons does not result in a substantial increment of J_s in the bulk [192].

To scrutinize any further enhancement in the spin current density J_s at the injection boundary or in the bulk due to a charge accumulation, the variation of J_s for different values of spin density polarization β_0 at the injection boundary is shown in Figure 5.21. Indeed for $\beta_0=1$, J_s close to the spin injection interface is significantly higher at charge accumulation compared to charge neutrality. In contrast, at a distance of about one Debye length from the interface, J_s becomes the same to that at the interface under the charge neutrality conditions. Now, one must check the behavior of J_s near the boundary and the bulk, when $\beta_0 < 1$. Figure 5.21 also shows if $\beta_0=0.8$, it is not possible to obtain a value for J_s in the bulk as high as for $\beta_0=1$, even under higher charge accumulation at the left interface and the current is close to that under the charge neutrality condition [192].

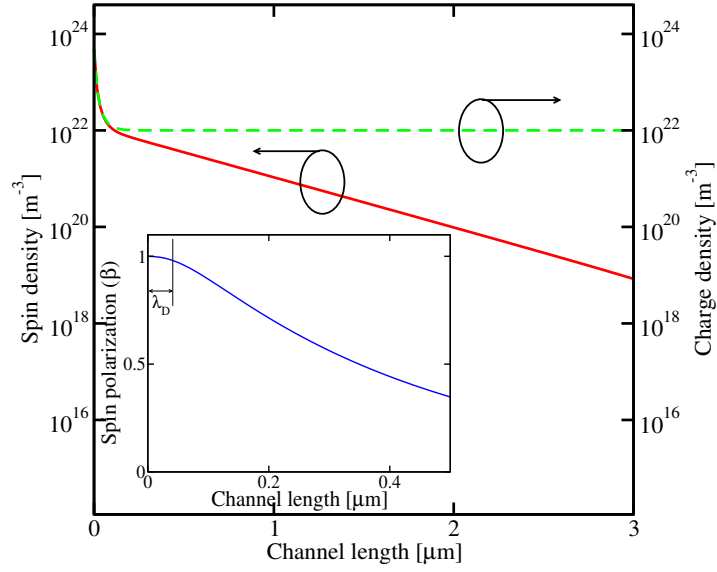


Figure 5.22: The charge and the spin distribution over the channel are shown under the charge accumulation and with the boundary condition Equation 5.57 ($M_{Ch}=100\text{mV}$, $U_c=-300\text{mV}$). The inset figure shows the spin density polarization β near the spin injecting interface. The current density 11.9MAm^{-2} is maintained over a $4\mu\text{m}$ channel.

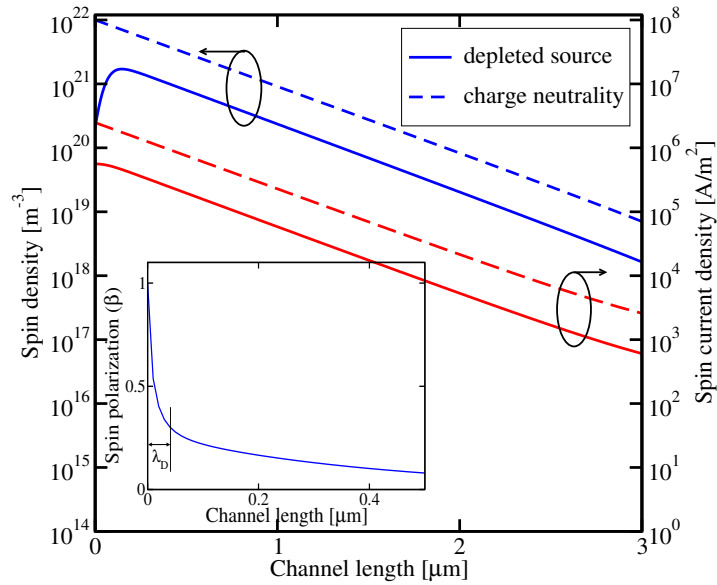


Figure 5.23: The spin and spin current densities in depletion ($M_{Ch}=-100\text{mV}$, $U_c=-140\text{mV}$) and for charge neutrality ($U_c=-204\text{mV}$) with the boundary as in Equation 5.57 are shown. The inset figure shows the spin density polarization β . The current density 11.9MAm^{-2} is maintained over a $4\mu\text{m}$ channel.

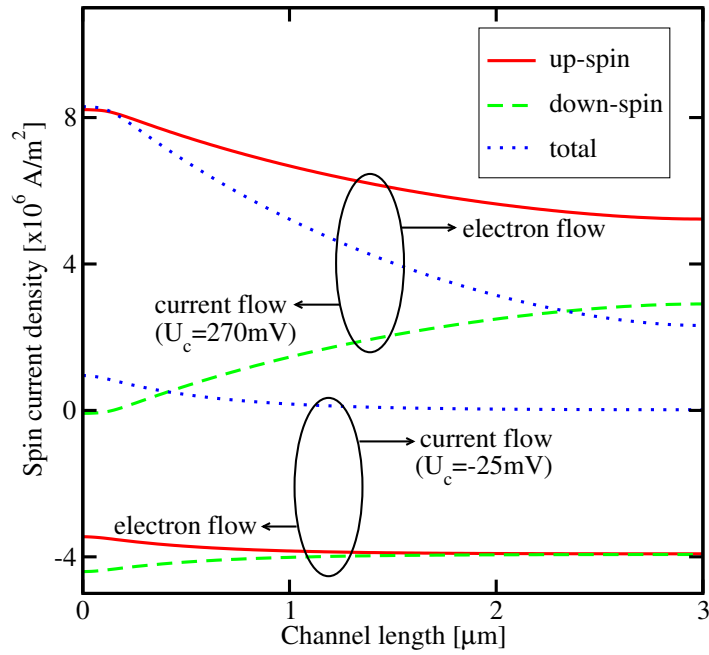


Figure 5.24: The spin current densities with their up(down)-spin components are depicted, when the channel is in depletion ($M_{Ch}=-100\text{mV}$) with the boundary as in Equation 5.57. The current density 7.9MAm^{-2} is maintained.

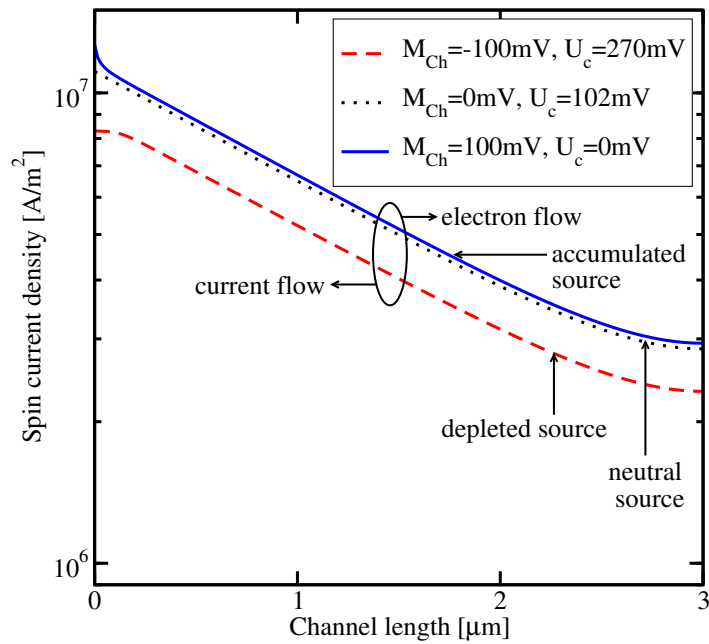


Figure 5.25: The spin current density for accumulation, charge neutrality, and depletion with the boundary condition Equation 5.57 are shown. The current density 7.9MAm^{-2} is maintained.

Behavior of the Spin Density Polarization

Up to now it has been predicted that at a fixed boundary spin density polarization β_0 and at a fixed charge current, the spin density s and the spin current density J_s show an increment at the spin injection interface by injecting more charge, but the bulk signals are determined by the charge neutrality condition. On the contrary, the spin signals are diminished dramatically both at the interface and the bulk when spin is injected from a charge depleted source. One must examine the peculiarities of the spin density polarization β , the electron concentration n , and the spin density s close to the left boundary in order to explain this behavior.

- Figure 5.22 shows both n and s in the same scale to allow a comparison. One can notice that β remains approximately constant through the accumulation layer, while the charge decrease from its high value at the interface to the equilibrium value determined by the donor concentration N_D . Therefore, s also decreases substantially within the accumulation region. Thus, J_s in the bulk is determined by the value of s at the end of the accumulation layer, where the charge neutrality condition is restored, and is thus determined by J_s at the charge neutrality condition with the same spin density polarization at the injection boundary β_0 .
- Figure 5.23 highlights s and J_s in the same plot in order to make a comparison, when spin is injected from a charge depleted source. When the spin diffusion is along the current like in Figure 5.23, a substantial decrease of s and hence J_s is noticed, both at the interface and the bulk as compared to their values at the charge neutrality condition. This behavior can be correlated with a significant increase of the minority (down-spin) spin current density (J_{\downarrow}) in the depletion layer (c.f. Figure 5.24). This current is due to two contributions, drift and diffusion, which add constructively in this case and cause β to decrease substantially over a very short distance close to the interface. At the same time, J_s is noticed to be nearly constant through the depletion layer. Indeed, in this case the spin diffusion length is increased due to the high value of the electric field \tilde{E} at the depletion region. At the end of the space-charge layer β is thus significantly smaller than at the interface [193], explaining the degradation of J_s in the bulk as compared to the charge neutrality condition. The sharp decrease of β is due to the high spin minority current close to the interface. Should this current be reduced, for instance by applying a voltage of opposite polarity and inverting the current (c.f. Figure 5.24), J_s in the bulk is enhanced, but still remains below the level determined by the charge neutrality condition (c.f. Figure 5.25).

6 Summary and Outlook

”Try not to become a man of success, but rather try to become a man of value.”

Albert Einstein

The $\mathbf{k} \cdot \mathbf{p}$ model is a powerful tool which allows to obtain the subband wave functions and the eigenenergies of stationary states in confined electron systems. The spin degree of freedom is incorporated in a two-band $\mathbf{k} \cdot \mathbf{p}$ model which is in turn developed at the vicinity of the X -point in the Brillouin zone including the uniaxial shear tensile stress in $[110]$ direction. This allows to find the electron subband energies and the corresponding spin-wave functions in thin silicon films under strain. The expressions of the wave functions are then obtained analytically, when their spin is parallel to the injection orientation.

In (001) oriented silicon films the degeneracy of the unprimed subbands is lifted by strain, which leads to a transport effective mass dependence on strain. The momentum relaxation time is observed to be increasing with strain but not significantly. The unprimed subbands degeneracy lifting turns out to be the most important effect for spin transport properties in silicon, because intervalley processes between equivalent valleys (g -processes) are dominant for spin relaxation. This is in contrast to the momentum relaxation time which is solely determined by the intravalley scattering. The minimum value of the unprimed subbands splitting, or the valley splitting, is determined by the strength of the spin-orbit interaction alone. The strongest mixing between the up-spin and down-spin states from the two unprimed subbands is observed, when the valley splitting reaches its minimum, which in turn results in the formation of the spin hot spots characterized by strong spin relaxation. For higher strain values the hot spots are pushed to higher energies away from the subband minima, causing a strong increase of the spin lifetime. The calculations are performed by considering surface roughness and electron-phonon interaction mediated spin relaxation. The transversal and longitudinal acoustic phonons are included. It turns out that strain routinely used to enhance mobility can also be used to boost the spin lifetime.

Including the primed subband into consideration, the evaluation of the spin lifetime due to the optical phonon induced scattering between non-equivalent valleys (f -processes) has been investigated. In thin films of less than 4nm the contributions

from the optical phonons can be neglected, whereas the spin lifetime in bulk is primarily determined by them. In addition, the [001] equivalent valley coupling through the Γ -point results in a subband splitting even in the absence of strain, which in turn softens the spin hot spots. This eventually results in the less pronounced nature of the spin lifetime dependence on strain, although almost two orders of magnitude enhancement is predicted.

The spin relaxation is also sensitive to the spin injection orientation, and its inter- and intrasubband components are equally sensitive to it. The surface roughness, the acoustic, and the optical phonon mediated spin lifetimes increase, when the injection direction is drawn from the perpendicular-plane ([001] direction) towards the in-plane (i.e. [100] direction) of the sample, by a factor of two. The long lifetime in such a film is essential to build spin interconnects for all-spin logic devices and the developed direction sensitive model can be used as an extra degree of freedom for designing such circuits.

The spin drift-diffusion model is widely used to describe the classical transport of charge carriers and their spins in a semiconductor. The spin injection from a semiconductor ferromagnet into silicon is analyzed for charge neutrality and means to improve the injection efficiency by an electric field. When the charge neutrality condition is violated, the additional interface charge screening is noted to impact the spin density near the interface. The bulk spin injection efficiency is increased (decreased), when injected from a charge-depleted (accumulated) source. However, the injection efficiency is always limited by the bulk spin polarization in the ferromagnetic side.

By investigating spin injection in silicon from only a space-charge layer, one finds substantial differences in the spin signals. At a fixed interface spin polarization and fixed charge current, the interface spin current is enhanced through injecting more charge, but the bulk spin current is almost unchanged from that obtained at the charge neutrality condition. In contrast, the spin current (and the spin density) in both interface and the bulk is reduced, when spin is injected from a charge depletion region. This is an important phenomenon which implies that the observation of a spin current reduction serves as a signature of the injection of spins from a charge and spin depleted layer. In a broader perspective, these results will have consequences in the spin control in the mesoscopic devices.

Bibliography

- [1] G. E. Moore. Cramming More Components Onto Integrated Circuits. *Electronics*, pages 114–117, 1965.
- [2] International Technology Roadmap for Semiconductors: 2013 Edition. <http://www.itrs.net>, 2013.
- [3] G. I. Bourianoff, P. A. Gargini, and D. E. Nikonov. Research Directions in beyond CMOS Computing. *Solid-State Electronics*, 51:1426–1431, 2007.
- [4] M. Bohr. The Evolution of Scaling from the Homogeneous Era to the Heterogeneous Era. In *2011 IEEE International Electron Devices Meeting (IEDM)*, pages 1.1.1–1.1.6, 2011.
- [5] N. S. Kim, T. Austin, D. Blaauw, T. Mudge, K. Flautner, J. S. Hu, M. J. Irwin, M. Kandemir, and V. Narayanan. Leakage Current: Moore’s Law Meets Static Power. *Computer*, 36:68–75, 2003.
- [6] K. Rupp and S. Selberherr. The Economic Limit to Moore’s Law. *Proceedings of the IEEE*, 98:351–353, 2010.
- [7] S. A. Wolf, A. Y. Chtchelkanova, and D. M. Treger. Spintronics - A Retrospective and Perspective. *IBM Journal of Research and Development*, 50:101, 2006.
- [8] I. Appelbaum, B. Huang, and D. J. Monsma. Electronic Measurement and Control of Spin Transport in Silicon. *Nature*, 447:295–298, 2007.
- [9] F. J. Jedema, H. B. Heersche, A. T. Filip, J. J. A. Baselmans, and B. J. van Wees. Electrical Detection of Spin Precession in a Metallic Mesoscopic Spin Valve. *Nature*, 416:713–716, 2002.
- [10] S. O. Valenzuela and M. Tinkham. Direct Electronic Measurement of the Spin Hall Effect. *Nature*, 442:176–179, 2006.
- [11] D. E. Nikonov and I. A. Young. Overview of Beyond-CMOS Devices and a Uniform Methodology for their Benchmarking. *Proceedings of the IEEE*, 101:1–36, 2013.
- [12] S. A. Wolf, D. D. Awschalom, R. A. Buhrman, J. M. Daughton, S. von Molnár, M. L. Roukes, A. Y. Chtchelkanova, and D. M. Treger. Spintronics: A Spin-Based Electronics Vision for the Future. *Science*, 294:1488–1495, 2001.

-
- [13] D. D. Awschalom, D. Loss, and N. Samarth. *Semiconductor Spintronics and Quantum Computation*. Springer-Verlag Berlin Heidelberg, 2002.
- [14] A. Fert. Nobel Lecture: Origin, Development, and Future of Spintronics. *Reviews of Modern Physics*, 80:1517–1530, 2008.
- [15] M. Johnson. Bipolar Spin Switch. *Science*, 260:320–323, 1993.
- [16] J. Sinova and I. Zutic. New Moves of the Spintronics Tango. *Nature Materials*, 11:368–371, 2012.
- [17] M. N. Baibich, J. M. Broto, A. Fert, F. Nguyen Van Dau, F. Petroff, P. Etienne, G. Creuzet, A. Friederich, and J. Chazelas. Giant Magnetoresistance of (001)Fe/(001)Cr Magnetic Superlattices. *Physical Review Letters*, 61:2472–2475, 1988.
- [18] H. Fujimori, S. Mitani, and S. Ohnuma. Tunnel-type GMR in Metal-Nonmetal Granular Alloy Thin Films. *Materials Science and Engineering: B*, 31:219–223, 1995.
- [19] S. Yuasa, T. Nagahama, A. Fukushima, Y. Suzuki, and K. Ando. Giant Room-Temperature Magnetoresistance in Single-Crystal Fe/MgO/Fe Magnetic Tunnel Junctions. *Nature Materials*, 3:868–871, 2004.
- [20] S. S. P. Parkin, C. Kaiser, A. Panchula, P. M. Rice, and B. Hughes. Giant Tunneling Magnetoresistance at Room Temperature with MgO (100) Tunnel Barriers. *Nature Materials*, 3:862–867, 2004.
- [21] B. E. Kane. A Silicon-Based Nuclear Spin Quantum Computer. *Nature*, 393:133–137, 1998.
- [22] D. Loss and D. P. DiVincenzo. Quantum Computation with Quantum Dots. *Physical Review A*, 57:120–126, 1998.
- [23] W. Gerlach and O. Stern. Der Experimentelle Nachweis der Richtungsquantelung im Magnetfeld. *Zeitschrift für Physik*, 9:349–352, 1922.
- [24] P. M. Tedrow and R. Meservey. Spin Polarization of Electrons Tunneling from Films of Fe, Co, Ni, and Gd. *Physical Review B*, 7:318–326, 1973.
- [25] M. I. D'yakonov and V. I. Perel'. Spin Relaxation of Conduction Electrons in Noncentrosymmetric Semiconductors. *Fizika Tverdogo Tela*, 13:1382–1397, 1971.
- [26] L. Vorob'ev, E. L. Ivchenko, G. Pikus, I. I. Farbshtein, V. A. Shalygin, and A. V. Shturbin. Optical Activity in Tellurium Induced by a Current. *Journal of Experimental and Theoretical Physics Letters*, 29:441, 1979.
- [27] M. Julliere. Tunneling between Ferromagnetic Films. *Physics Letters A*, 54:225–226, 1975.

- [28] A. G. Aronov and G. E. Pikus. Spin Injection in Semiconductors. *Fizika i Tekhnika Poluprovodnikov*, 10:1177–1180, 1976.
- [29] P. Grünberg and A. Fert. The Discovery of Giant Magnetoresistance (Scientific Background on the Nobel Prize in Physics). http://www.kva.se/Documents/Priser/Nobel/2007/sciback_fy_en_07.pdf, 2007.
- [30] T. Shinjo. *Nanomagnetism and Spintronics*. Elsevier insights. Elsevier Science, 2013.
- [31] L. Zhu. *Spin Injection and Transport in Semiconductor and Metal Nanostructures*. PhD thesis, Department of Physics, University of California, San Diego, USA, 2009.
- [32] J. Mathon and A. Umerski. Theory of Tunneling Magnetoresistance in a Junction with a Nonmagnetic Metallic Interlayer. *Physics Letters B*, 60:1117–1121, 1999.
- [33] J. S. Moodera, L. R. Kinder, T. M. Wong, and R. Meservey. Large Magnetoresistance at Room Temperature in Ferromagnetic Thin Film Tunnel Junctions. *Physical Review Letters*, 74:3273–3276, 1995.
- [34] T. Miyazaki and N. Tezuka. Giant Magnetic Tunneling Effect in Fe/Al₂O₃/Fe Junction. *Journal of Magnetism and Magnetic Materials*, 139:L231–L234, 1995.
- [35] J.C. Slonczewski. Current-Driven Excitation of Magnetic Multilayers. *Journal of Magnetism and Magnetic Materials*, 159:L1–L7, 1996.
- [36] L. Berger. Emission of Spin Waves by a Magnetic Multilayer Traversed by a Current. *Physical Review B*, 54:9353–9358, 1996.
- [37] W. H. Kautz. Cellular Logic-in-Memory Arrays. *IEEE Transactions on Computers*, C-18:719–727, 1969.
- [38] H. Ohno, T. Endoh, T. Hanyu, N. Kasai, and S. Ikeda. Magnetic Tunnel Junction for Nonvolatile CMOS Logic. In *2010 IEEE International Electron Devices Meeting (IEDM)*, pages 9.4.1–9.4.4, 2010.
- [39] M. Natsui, D. Suzuki, N. Sakimura, R. Nebashi, Y. Tsuji, A. Morioka, T. Sugibayashi, S. Miura, H. Honjo, K. Kinoshita, S. Ikeda, T. Endoh, H. Ohno, and T. Hanyu. Nonvolatile Logic-in-Memory Array Processor in 90nm MTJ/MOS Achieving 75% Leakage Reduction Using Cycle-Based Power Gating. In *2013 IEEE International Solid-State Circuits Conference Digest of Technical Papers (ISSCC)*, pages 194–195, 2013.
- [40] H. Mahmoudi. *Devices and Circuits for Stateful Logic and Memristive Sensing Applications*. PhD thesis, Fakultät für Elektrotechnik und Informationstechnik, Technischen Universität Wien, Austria, 2014.

- [41] S. Datta and B. Das. Electronic Analog of the Electro-Optic Modulator. *Applied Physics Letters*, 56:665–667, 1990.
- [42] S. Sugahara and J. Nitta. Spin-Transistor Electronics: An Overview and Outlook. *Proceedings of the IEEE*, 98:2124–2154, 2010.
- [43] M.K. Hudait, G. Dewey, S. Datta, J.M. Fastenau, J. Kavalieros, W.K. Liu, D. Lubyshev, R. Pillarisetty, W. Rachmady, M. Radosavljevic, T. Rakshit, and R. Chau. Heterogeneous Integration of Enhancement Mode $\text{In}_{0.7}\text{Ga}_{0.3}\text{As}$ Quantum Well Transistor on Silicon Substrate using Thin ($\leq 2\mu\text{m}$) Composite Buffer Architecture for High-Speed and Low-Voltage (0.5V) Logic Applications. In *2007 IEEE International Electron Devices Meeting (IEDM)*, pages 625–628, 2007.
- [44] R. Jansen. Silicon Spintronics. *Nature Materials*, 11:400–408, 2012.
- [45] F. Jelezko, T. Gaebel, I. Popa, A. Gruber, and J. Wrachtrup. Observation of Coherent Oscillations in a Single Electron Spin. *Physical Review Letters*, 92:076401, 2004.
- [46] A. Honig and J. Combrisson. Paramagnetic Resonance in As-Doped Silicon. *Physical Review*, 102:917–918, 1956.
- [47] G. Feher. Electron Spin Resonance Experiments on Donors in Silicon. I. Electronic Structure of Donors by the Electron Nuclear Double Resonance Technique. *Physical Review*, 114:1219–1244, 1959.
- [48] G. Lancaster, J. A. van Wyk, and E. E. Schneider. Spin-Lattice Relaxation of Conduction Electrons in Silicon. *Proceedings of the Physical Society*, 84, 1964.
- [49] I. Žutić, J. Fabian, and S. C. Erwin. Spin Injection and Detection in Silicon. *Physical Review Letters*, 97:026602, 2006.
- [50] Electrical Properties of Silicon (Si). <http://www.ioffe.rssi.ru/SVA/NSM/Semicond/Si/electric.html>, 2015.
- [51] S. Bandyopadhyay and M. Cahay. Electron Spin for Classical Information Processing: a Brief Survey of Spin-Based Logic Devices, Gates and Circuits. *Nanotechnology*, 20(41):412001, 2009.
- [52] P. Mavropoulos. Spin Injection from Fe into Si(001): Ab initio Calculations and Role of the Si Complex Band Structure. *Physical Review B*, 78:054446, 2008.
- [53] Y. Song and H. Dery. Analysis of Phonon-Induced Spin Relaxation Processes in Silicon. *Physical Review B*, 86:085201, 2012.
- [54] B. Behin-Aein, D. Datta, S. Salahuddin, and S. Datta. Proposal for an All-Spin Logic Device with Built-in Memory. *Nature Nanotechnology*, 5:266–270, 2010.
- [55] V. Sverdlov and S. Selberherr. Silicon Spintronics: Progress and Challenges. *Physics Reports*, 585:15–17, 2015.

- [56] D. J. Lépine. Spin Resonance of Localized and Delocalized Electrons in Phosphorus-Doped Silicon between 20 and 30 °K. *Physical Review B*, 2:2429–2439, 1970.
- [57] B. Huang, D. J. Monsma, and I. Appelbaum. Coherent Spin Transport through a 350 Micron Thick Silicon Wafer. *Physical Review Letters*, 99:177209, 2007.
- [58] S. P. Dash, S. Sharma, R. S. Patel, M. P. de Jong, and R. Jansen. Electrical Creation of Spin Polarization in Silicon at Room Temperature. *Nature*, 462:491–494, 2009.
- [59] C. H. Li, O. M. J. van ’t Erve, and B. T. Jonker. Electrical Injection and Detection of Spin Accumulation in Silicon at 500 K with Magnetic Metal/Silicon Dioxide Contacts. *Nature communications*, 2:245, 2011.
- [60] J. Li and I. Appelbaum. Modeling Spin Transport in Electrostatically-Gated Lateral-Channel Silicon Devices: Role of Interfacial Spin Relaxation. *Physical Review B*, 84:165318, 2011.
- [61] J. Li and I. Appelbaum. Lateral Spin Transport through Bulk Silicon. *Applied Physics Letters*, 100:162408, 2012.
- [62] I. Žutić, J. Fabian, and S. Das Sarma. Spintronics: Fundamentals and Applications. *Review Modern Physics*, 76:323–410, 2004.
- [63] R. J. Elliott. Theory of the Effect of Spin-Orbit Coupling on Magnetic Resonance in Some Semiconductors. *Physical Review*, 96:266–279, 1954.
- [64] Y. Yafet. Conduction Electron Spin Relaxation in the Superconducting State. *Physics Letters A*, 98:287–290, 1983.
- [65] M. D’yakonov and V. Perel’. Spin Relaxation of Conduction Electrons in Noncentrosymmetric Semiconductors. *Soviet Physics Solid State, USSR*, 13:3023–3026, 1972.
- [66] A. W. Overhauser. Paramagnetic Relaxation in Metals. *Physical Review*, 89:689–700, 1953.
- [67] J. L. Cheng, M. W. Wu, and J. Fabian. Theory of the Spin Relaxation of Conduction Electrons in Silicon. *Physical Review Letters*, 104:016601, 2010.
- [68] J. M. Tang, B. T. Collins, and M. E. Flatte. Electron Spin-Phonon Interaction Symmetries and Tunable Spin Relaxation in Silicon and Germanium. *Physical Review B*, 85:045202, 2012.
- [69] M. V. Fischetti, Z. Ren, P. M. Solomon, M. Yang, and K. Rim. Six-Band $\mathbf{k} \cdot \mathbf{p}$ Calculation of the Hole Mobility in Silicon Inversion Layers: Dependence on Surface Orientation, Strain, and Silicon Thickness. *Journal of Applied Physics*, 94:1079–1095, 2003.

- [70] D. Osintsev, V. Sverdlov, and S. Selberherr. Reduction of Momentum and Spin Relaxation Rate in Strained Thin Silicon Films. In *Proceedings of the European Solid-State Device Research Conference (ESSDERC)*, pages 334–337, 2013.
- [71] P. Li and H. Dery. Spin-Orbit Symmetries of Conduction Electrons in Silicon. *Physical Review Letters*, 107:107203, 2011.
- [72] V. Sverdlov. *Strain-Induced Effects in Advanced MOSFETs*. Wien - New York: Springer, 2011.
- [73] C. S. Smith. Piezoresistance Effect in Germanium and Silicon. *Physical Review*, 94:42–49, 1954.
- [74] H. H. Hall, J. Bardeen, and G. L. Pearson. The Effects of Pressure and Temperature on the Resistance of $p - n$ Junctions in Germanium. *Physical Review*, 84:129–132, 1951.
- [75] J. Bardeen and W. Shockley. Deformation Potentials and Mobilities in Non-Polar Crystals. *Physical Review*, 80:72–80, 1950.
- [76] C. Herring and E. Vogt. Transport and Deformation-Potential Theory for Many-Valley Semiconductors with Anisotropic Scattering. *Physical Review*, 101:944–961, 1956.
- [77] K. Rim, J. Chu, H. Chen, K.A. Jenkins, T. Kanarsky, K. Lee, A. Mocuta, H. Zhu, R. Roy, J. Newbury, J. Ott, K. Petrarca, P. Mooney, D. Lacey, S. Koester, K. Chan, D. Boyd, M. Jeong, and H.-S. Wong. Characteristics and Device Design of sub-100 nm Strained Si N- and PMOSFETs. In *Digest of Technical Papers. 2002 Symposium on VLSI Technology, 2002*, pages 98–99, 2002.
- [78] S. E. Thompson, M. Armstrong, C. Auth, M. Alavi, M. Buehler, R. Chau, S. Cea, T. Ghani, G. Glass, T. Hoffman, Chia-Hong Jan, C. Kenyon, J. Klaus, K. Kuhn, Zhiyong Ma, B. McIntyre, K. Mistry, A. Murthy, B. Obradovic, R. Nagisetty, Phi Nguyen, S. Sivakumar, R. Shaheed, L. Shifren, B. Tufts, S. Tyagi, M. Bohr, and Y. El-Mansy. A 90-nm Logic Technology Featuring Strained-Silicon. *IEEE Transactions on Electron Devices*, 51:1790–1797, 2004.
- [79] K. Rim, K. Chan, L. Shi, D. Boyd, J. Ott, N. Klymko, F. Cardone, L. Tai, S. Koester, M. Cobb, D. Canaperi, B. To, E. Duch, I. Babich, R. Carruthers, P. Saunders, G. Walker, Y. Zhang, M. Steen, and M. Jeong. Fabrication and Mobility Characteristics of Ultra-thin Strained Si Directly on Insulator (SS-DOI) MOSFETs. In *2003 IEEE International Electron Devices Meeting (IEDM)*, pages 3.1.1–3.1.4, 2003.
- [80] F. Andrieu, T. Ernst, O. Faynot, O. Rozeau, Y. Bogumilowicz, J.-M. Hartmann, L. Brévard, A. Toffoli, D. Lafond, B. Ghyselen, F. Fournel, G. Ghibaudo, and S. Deleonibus. Performance and Physics of sub-50 nm Strained Si on $\text{Si}_{1-x}\text{Ge}_x$ -on-insulator SGOI nMOSFETs. *Solid-State Electronics*, 50:566–572, 2006.

-
- [81] D. Esseni. On the Modeling of Surface Roughness Limited Mobility in SOI MOS-FETs and its Correlation to the Transistor Effective Field. *IEEE Transactions on Electron Devices*, 51:394–401, 2004.
- [82] F. Seitz. The Theoretical Constitution of Metallic Lithium. *Physical Review*, 47:400–412, 1935.
- [83] J. M. Luttinger and W. Kohn. Motion of Electrons and Holes in Perturbed Periodic Fields. *Physical Review*, 97:869–883, 1955.
- [84] E. O. Kane. Energy Band Structure in p-type Germanium and Silicon. *Journal of Physics and Chemistry of Solids*, 1:82–99, 1956.
- [85] M. Cardona and F. H. Pollak. Energy-Band Structure of Germanium and Silicon: The $\mathbf{k} \cdot \mathbf{p}$ Method. *Physical Review*, 142:530–543, 1966.
- [86] G.L. Bir and G.E. Pikus. *Symmetry and Strain-Induced Effects in Semiconductors*. New York/Toronto: J. Wiley & Sons, 1974.
- [87] T. Ando, Alan B. Fowler, and F. Stern. Electronic Properties of Two-Dimensional Systems. *Reviews of Modern Physics*, 54:437–672, 1982.
- [88] G. Lampel. Nuclear Dynamic Polarization by Optical Electronic Saturation and Optical Pumping in Semiconductors. *Physical Review Letters*, 20:491–493, 1968.
- [89] F. Nastos, J. Rioux, M. Strimas-Mackey, Bernardo S. Mendoza, and J. E. Sipe. Full Band Structure LDA and $\mathbf{k} \cdot \mathbf{p}$ Calculations of Optical Spin-Injection. *Physical Review B*, 76:205113, 2007.
- [90] M. Johnson and R. H. Silsbee. Interfacial Charge-Spin Coupling: Injection and Detection of Spin Magnetization in Metals. *Physical Review Letters*, 55:1790–1793, 1985.
- [91] M. Johnson and R. H. Silsbee. Thermodynamic Analysis of Interfacial Transport and of the Thermomagnetolectric System. *Physical Review B*, 35:4959–4972, 1987.
- [92] M. Johnson and R. H. Silsbee. Electron Spin Injection and Detection at a Ferromagnetic/Paramagnetic Interface (invited). *Journal of Applied Physics*, 63:3934–3939, 1988.
- [93] T. Koga, J. Nitta, H. Takayanagi, and S. Datta. Spin-Filter Device Based on the Rashba Effect Using a Nonmagnetic Resonant Tunneling Diode. *Physical Review Letters*, 88:126601, 2002.
- [94] M. Shen, S. Saikin, and M. Cheng. Monte Carlo Modeling of Spin Injection Through a Schottky Barrier and Spin Transport in a Semiconductor Quantum Well. *Journal of Applied Physics*, 96:4319–4325, 2004.

- [95] G. Schmidt, D. Ferrand, L. W. Molenkamp, A. T. Filip, and B. J. van Wees. Fundamental Obstacle for Electrical Spin Injection from a Ferromagnetic Metal into a Diffusive Semiconductor. *Physical Review B*, 62:R4790–R4793, 2000.
- [96] E. I. Rashba. Theory of Electrical Spin Injection: Tunnel Contacts as a Solution of the Conductivity Mismatch Problem. *Physical Review B*, 62:R16267–R16270, 2000.
- [97] A. Fert and H. Jaffrès. Conditions for Efficient Spin Injection from a Ferromagnetic Metal into a Semiconductor. *Physical Review B*, 64:184420, 2001.
- [98] A. T. Filip, B. H. Hoving, F. J. Jedema, B. J. van Wees, B. Dutta, and S. Borghs. Experimental Search for the Electrical Spin Injection in a Semiconductor. *Physical Review B*, 62:9996–9999, 2000.
- [99] B. C. Min, K. Motohashi, C. Lodder, and R. Jansen. Tunable Spin-Tunnel Contacts to Silicon using Low-Work-Function Ferromagnets. *Nature Materials*, 5:871–822, 2006.
- [100] B. T. Jonker, G. Kioseoglou, A. T. Hanbicki, C. H. Li, and P. E. Thompson. Electrical Spin-Injection into Silicon from a Ferromagnetic Metal/Tunnel Barrier Contact. *Nature Physics*, 3:542–546, 2007.
- [101] V. P. LaBella, D. W. Bullock, Z. Ding, C. Emery, A. Venkatesan, W. F. Oliver, G. J. Salamo, P. M. Thibado, and M. Mortazavi. Spatially Resolved Spin-Injection Probability for Gallium Arsenide. *Science*, 292:1518–1521, 2001.
- [102] T. Nie, J. Tang, and K. L. Wang. Quest for High-Curie Temperature $\text{Mn}_x\text{Ge}_{1-x}$ Diluted Magnetic Semiconductors for Room-Temperature Spintronics Applications. *Journal of Crystal Growth*, 425:279–282, 2015.
- [103] Y. Takamura, K. Hayashi, Y. Shuto, and S. Sugahara. Fabrication of High-Quality CO_2 $\text{FeSi}/\text{SiO}_x\text{N}_y/\text{Si}(100)$ Tunnel Contacts Using Radical-Oxynitridation-Formed SiO_xN_y Barrier for Si-Based Spin Transistors. *Journal of Electronic Materials*, 41:954–958, 2012.
- [104] T. Suzuki, T. Sasaki, T. Oikawa, M. Shiraishi, Y. Suzuki, and K. Noguchi. Room-Temperature Electron Spin Transport in a Highly Doped Si Channel. *Applied Physics Express*, 4:023003, 2011.
- [105] Y. Song and H. Dery. Magnetic-Field-Modulated Resonant Tunneling in Ferromagnetic-Insulator-Nonmagnetic Junctions. *Physical Review Letters*, 113:047205, 2014.
- [106] K. R. Jeon, H. Saito, S. Yuasa, and R. Jansen. Energy Dispersion of Tunnel Spin Polarization Extracted from Thermal and Electrical Spin Currents. *Physical Review B*, 91:155305, 2015.

- [107] H. Saito, S. Watanabe, Y. Mineno, S. Sharma, R. Jansen, S. Yuasa, and K. Ando. Electrical Creation of Spin Accumulation in p-type Germanium. *Solid-State Communications*, 151:1159–1161, 2011.
- [108] K. R. Jeon, B. C. Min, Y. H. Jo, H. S. Lee, I. J. Shin, C. Y. Park, S. Y. Park, and S. C. Shin. Electrical Spin Injection and Accumulation in CoFe/MgO/Ge Contacts at Room Temperature. *Physical Review B*, 84:165315, 2011.
- [109] A. Jain, L. Louahadj, J. Peiro, J. C. Le Breton, C. Vergnaud, A. Barski, C. Beign, L. Notin, A. Marty, V. Baltz, S. Auffret, E. Augendre, H. Jaffrs, J. M. George, and M. Jamet. Electrical Spin Injection and Detection at Al₂O₃/n-type Germanium Interface using Three Terminal Geometry. *Applied Physics Letters*, 99:162102, 2011.
- [110] M. Tran, H. Jaffrès, C. Deranlot, J.-M. George, A. Fert, A. Miard, and A. Lemaître. Enhancement of the Spin Accumulation at the Interface Between a Spin-Polarized Tunnel Junction and a Semiconductor. *Physical Review Letters*, 102:036601, 2009.
- [111] O. M. J. van 't Erve, A. L. Friedman, E. Cobas, C. H. Li, J. T. Robinson, and B. T. Jonker. Low-Resistance Spin Injection into Silicon using Graphene Tunnel Barriers. *Nature Nanotechnology*, 7:737–742, 2012.
- [112] O. Txoperena, Y. Song, L. Qing, M. Gobbi, L. E. Hueso, H. Dery, and F. Casanova. Impurity-Assisted Tunneling Magnetoresistance under a Weak Magnetic Field. *Physical Review Letters*, 113:146601, 2014.
- [113] M. R. Sears and W. M. Saslow. Spin Accumulation at Ferromagnet/Nonmagnetic Material Interfaces. *Physical Review B*, 85:014404, 2012.
- [114] R. Hull and INSPEC (Information service). *Properties of Crystalline Silicon*. EMIS datareviews series. INSPEC, the Institution of Electrical Engineers, 1999.
- [115] The ABC of DFT. <http://dft.uci.edu/doc/g1.pdf>, 2007.
- [116] S. Datta. Nanoscale Device Modeling: The Green's Function Method. *Superlattices and Microstructures*, 28(4):253–259, 2000.
- [117] C. Kittel. *Introduction to Solid State Physics*. Wiley, 2004.
- [118] M. A. Omar. *Elementary Solid State Physics: Principles and Applications*. Addison-Wesley Publishing Company, 2007.
- [119] T. B. Boykin, G. Klimeck, R. C. Bowen, and R. Lake. Effective-Mass Reproducibility of the Nearest-Neighbor sp^3s^* Models: Analytical Results. *Physical Review B*, 61(7):4102–4107, 1997.
- [120] T. B. Boykin, L. J. Gamble, G. Klimeck, and R. C. Bowden. Valence-Band Warping in Tight-Binding Models. *Physical Review B*, 59(11):7301–7304, 1999.

-
- [121] D. Helmholz and L. C. Lew Yan Voon. Warping in the Valence Band of Silicon. *Physical Review B*, 65(23):233204, 2002.
- [122] J. P. Loehr and D. N. Talwar. Exact Parameter Relations and Effective Masses Within sp^3s Zinc-blende Tight-Binding Models. *Physical Review B*, 55(7):4353–4359, 1997.
- [123] T. B. Boykin, G. Klimeck, and F. Oyafuso. Valence Band Effective-Mass Expressions in the $sp^3d^5s^*$ Empirical Tight-Binding Model Applied to a Si and Ge Parametrization. *Physical Review B*, 69:115201, 2004.
- [124] E. Wigner and F. Seitz. On the Constitution of Metallic Sodium. *Physical Review*, 43:804–810, 1933.
- [125] J. C. Slater. An Augmented Plane Wave Method for the Periodic Potential Problem. *Physical Review*, 92:603–608, 1937.
- [126] C. Herring. A New Method for Calculating Wave Functions in Crystals. *Physical Review*, 57:1169–1177, 1940.
- [127] Empirical Pseudopotential Method: Theory and Implementation. <https://nanohub.org/resources/8999>, 2010.
- [128] P. Yu and M. Cardona. *Fundamentals of Semiconductors*. Springer-Verlag Berlin Heidelberg, 2003.
- [129] D. Osintsev. *Modeling Spintronic Effects in Silicon*. PhD thesis, Fakultät für Elektrotechnik und Informationstechnik, Technischen Universität Wien, Austria, 2014.
- [130] Solving the Effective Mass Schrödinger Equation in State-of-the Art Devices. https://nanohub.org/resource_files/lm/SCHRED/schred_theoretical_background.pdf, 2006.
- [131] J. Fabian. *Semiconductor Spintronics*. Institute of Physics, Slovak Academy of Sciences, 2007.
- [132] C. Galeriu. $\mathbf{k} \cdot \mathbf{p}$ Theory of Semiconductor Nanostructures. PhD thesis, Faculty of the Worcester Polytechnic Institute, USA, 2005.
- [133] V. Borisenko and S. Ossicini. *What is What in the Nanoworld: A Handbook on Nanoscience and Nanotechnology*. Wiley, 2013.
- [134] C. C. Lo. *Electrical Detection of Spin-Dependent Transport in Silicon*. PhD thesis, EECS Department, University of California, Berkeley, USA, 2011.
- [135] G. Dresselhaus. Spin-Orbit Coupling Effects in Zinc Blende Structures. *Physical Review*, 100:580–586, 1955.

- [136] Y. A. Bychkov and E. I. Rashba. Oscillatory Effects and the Magnetic Susceptibility of Carriers in Inversion Layers. *Journal of Physics C: Solid State Physics*, 17:6039, 1984.
- [137] P. Boross, B. Dra, A. Kiss, and F. Simon. A Unified Theory of Spin-Relaxation due to Spin-Orbit Coupling in Metals and Semiconductors. *Scientific Reports*, 3:580–586, 2013.
- [138] V. Sverdlov, J. Ghosh, H. Mahmoudi, A. Makarov, D. Osintsev, T. Windbacher, and S. Selberherr. Modeling Spin-based Electronic Devices. In *Proceedings of the 29th International Conference on Microelectronics*, pages 27–34, 2014.
- [139] J. H. Davies. *The Physics of Low-Dimensional Semiconductors*. Cambridge University Press, 1998.
- [140] S. E. Ungersboeck. *Advanced Modeling of Strained CMOS Technology*. PhD thesis, Fakultät für Elektrotechnik und Informationstechnik, Technischen Universität Wien, Austria, 2007.
- [141] S. Dhar. *Analytical Mobility Modeling for Strained Silicon-Based Devices*. PhD thesis, Fakultät für Elektrotechnik und Informationstechnik, Technischen Universität Wien, Austria, 2007.
- [142] K. Uchida, A. Kinoshita, and M. Saitoh. Carrier Transport in (110) nMOS-FETs: Subband Structures, Non-Parabolicity, Mobility Characteristics, and Uniaxial Stress Engineering. In *2006 IEEE International Electron Devices Meeting (IEDM)*, pages 1–3, 2006.
- [143] S. Dhar, H. Kosina, V. Palankovski, E. Ungersböck, and S. Selberherr. Modeling of Electron Mobility in Strained Si Devices. In *Proceedings of the Semiconductor Advances for Future Electronics (SAFE)*, pages 793–796, 2004.
- [144] M. E. Kurdi, G. Fishman, S. Sauvage, and P. Boucaud. Comparison Between 6-band and 14-band $\mathbf{k} \cdot \mathbf{p}$ Formalisms in SiGe/Si Heterostructures. *Physical Review B*, 68:165333.1–165333.16, 2003.
- [145] D. Rideau, M. Feraille, L. Ciampolini, M. Minondo, C. Tavernier, H. Jaouen, and A. Ghetti. Strained Si, Ge, and $\text{Si}_{1-x}\text{Ge}_x$ Alloys Modeled with a First-Principles-Optimized Full-Zone $\mathbf{k} \cdot \mathbf{p}$ Method. *Physical Review B*, 74:195208, 2006.
- [146] T. Windbacher. *Engineering Gate Stacks for Field-Effect Transistors*. PhD thesis, Fakultät für Elektrotechnik und Informationstechnik, Technischen Universität Wien, Austria, 2010.
- [147] Y. Song. *Theory of Intrinsic Spin-Dependent Transport in Semiconductors and Two-Dimensional Membranes*. PhD thesis, Dept. of Physics and Astronomy, University of Rochester, USA, 2013.

- [148] T. Windbacher, V. Sverdlov, O. Baumgartner, and S. Selberherr. Electron Subband Structure in Strained Silicon UTB Films from the Hensel-Hasegawa-Nakayama Model - Part 1 Analytical Consideration and Strain-Induced Valley Splitting. *Solid-State Electronics*, 54:137–142, 2010.
- [149] J. Ghosh, D. Osintsev, V. Sverdlov, and S. Selberherr. Injection Direction Sensitive Spin Lifetime Model in a Strained Thin Silicon Film. In *Proceedings of the International Conference on Simulation of Semiconductor Processes and Devices (SISPAD)*, pages 277–280, 2015.
- [150] D. Osintsev, V. Sverdlov, N. Neophytou, and S. Selberherr. Valley Splitting and Spin Lifetime Enhancement in Strained Thin Silicon Films. In *Proceedings of the 17th International Workshop on Computational Electronics (IWCE)*, pages 1–4, 2014.
- [151] D. Osintsev, O. Baumgartner, Z. Stanojevic, V. Sverdlov, and S. Selberherr. Subband Splitting and Surface Roughness Induced Spin Relaxation in (001) Silicon SOI MOSFETs. *Solid-State Electronics*, 90:34–38, 2013.
- [152] V. Sverdlov, J. Ghosh, D. Osintsev, and S. Selberherr. Modeling Silicon Spintronics. *Recent Advances in Mathematical Methods in Applied Sciences*, 32:195–198, 2014.
- [153] J. Ghosh, D. Osintsev, V. Sverdlov, and S. Selberherr. Dependence of Spin Lifetime on Spin Injection Orientation in Strained Silicon Films. In *Proceedings of the Joint International EUROSOI Workshop and International Conference on Ultimate Integration on Silicon (EUROSOI-ULIS)*, pages 285–288, 2015.
- [154] J. Ghosh, D. Osintsev, V. Sverdlov, and S. Selberherr. Variation of Spin Lifetime with Spin Injection Orientation in Strained Thin Silicon Films. *ECS Transactions*, 66:233–240, 2015.
- [155] J. M. Ziman. *Electrons and Phonons: The Theory of Transport Phenomena in Solids*. Oxford University Press, 2001.
- [156] H. Ehrenreich and A. W. Overhauser. Scattering of Holes by Phonons in Germanium. *Physical Review*, 104:331–342, 1956.
- [157] J. M. Hinckley and J. Singh. Monte Carlo Studies of Ohmic Hole Mobility in Silicon and Germanium: Examination of the Optical Phonon Deformation Potential. *Journal of Applied Physics*, 76:4192–4200, 1994.
- [158] C. Jacoboni and L. Reggiani. The Monte Carlo Method for the Solution of Charge Transport in Semiconductors with Applications to Covalent Materials. *Reviews of Modern Physics*, 55:645–705, 1983.
- [159] H. Jang and I. Appelbaum. Spin Polarized Electron Transport near the Si/SiO₂ Interface. *Physical Review Letters*, 103:117202, 2009.

- [160] D. Osintsev, V. Sverdlov, and S. Selberherr. Influence of Surface Roughness Scattering on Spin Lifetime in Silicon. In *Book of Abstracts of the 16th International Workshop on Computational Electronics (IWCE 2013)*, pages 76–77, 2013.
- [161] J. Ghosh, D. Osintsev, V. Sverdlov, and S. Selberherr. Intersubband Spin Relaxation Reduction and Spin Lifetime Enhancement by Strain in SOI Structures. *Microelectronic Engineering*, 147:89–91, 2015.
- [162] H. Dery, Y. Song, P. Li, and I. Žutić. Silicon Spin Communication. *Applied Physics Letters*, 99:082502, 2011.
- [163] D. Osintsev, V. Sverdlov, and S. Selberherr. Influence of the Valley Degeneracy on Spin Relaxation in Thin Silicon Films. In *Proceedings of the 14th International Conference on Ultimate Integration on Silicon (ULIS)*, pages 221–224, 2013.
- [164] E. Ungersboeck, S. Dhar, G. Karlowatz, V. Sverdlov, H. Kosina, and S. Selberherr. The Effect of General Strain on the Band Structure and Electron Mobility of Silicon. *IEEE Transactions on Electron Devices*, 54:2183–2190, 2007.
- [165] M. V. Fischetti and S. E. Laux. Band Structure, Deformation Potentials, and Carrier Mobility in Strained Si, Ge, and SiGe Alloys. *Journal of Applied Physics*, 80(4):2234–2252, 1996.
- [166] J. Shah. *Hot Carriers in Semiconductor Nanostructures: Physics and Applications*. Academic Press, 1992.
- [167] D. Rideau, M. Feraille, M. Michailat, Y. M. Niquet, C. Tavernier, and H. Jaouen. On the Validity of the Effective Mass Approximation and the Luttinger $\mathbf{k} \cdot \mathbf{p}$ Model in Fully Depleted SOI MOSFETs. *Solid-State Electronics*, 53:452–461, 2009.
- [168] T. B. Boykin, G. Klimeck, M. A. Eriksson, M. Friesen, S. N. Coppersmith, P. von Allmen, F. Oyafuso, and S. Lee. Valley Splitting in Strained Silicon Quantum wells. *Applied Physics Letters*, 84:115–117, 2004.
- [169] M. O. Nestoklon, L. E. Golub, and E. L. Ivchenko. Spin and Valley-Orbit Splittings in SiGe/Si Heterostructures. *Physical Review B*, 73:235334, 2006.
- [170] D. Osintsev, V. Sverdlov, N. Neophytou, and S. Selberherr. Valley Splitting and Spin Lifetime Enhancement in Strained Silicon Heterostructures. *Proceedings of the International Winterschool on New Developments in Solid State Physics*, pages 88–89, 2014.
- [171] J. Ghosh, D. Osintsev, V. Sverdlov, and S. Selberherr. Spin Lifetime Dependence on Valley Splitting in Thin Silicon Films. In *Book of Abstracts of the 18th International Workshop on Computational Electronics (IWCE)*, pages 35–36, 2015.

-
- [172] D. Osintsev, V. Sverdlov, T. Windbacher, and S. Selberherr. Increasing Mobility and Spin Lifetime with Shear Strain in Thin Silicon Films. In *Proceedings of the International Conference on Simulation of Semiconductor Processes and Devices (SISPAD)*, pages 193–196, 2014.
- [173] Z. G. Yu and M. E. Flatté. Electric-field Dependent Spin Diffusion and Spin Injection into Semiconductors. *Physical Review B*, 66:201202, 2002.
- [174] Y. Song and H. Dery. Spin Transport Theory in Ferromagnet/Semiconductor Systems with Noncollinear Magnetization Configurations. *Physical Review B*, 81:045321, 2010.
- [175] A. M. Roy, D. E. Nikonov, and K. C. Saraswat. Simulation of Spin MOSFETs. *Proc. SPIE*, 8100:81001J–81001J–6, 2011.
- [176] J. M. Kikkawa and D. D. Awschalom. Lateral Drag of Spin Coherence in Gallium Arsenide. *Nature (London)*, 397:139, 1999.
- [177] I. Malaajovich, J. J. Berry, N. Samarth, and D. D. Awschalom. Persistent Sourcing of Coherent Spins for Multifunctional Spintronics. *Nature (London)*, 411:770, 2001.
- [178] W. V. Roosbroeck. Theory of the Flow of Electrons and Holes in Germanium and Other Semiconductors. *Bell System Technical Journal*, 29:560–607, 1950.
- [179] B. V. Zeghbroeck. Principles of Semiconductor Devices. http://ecee.colorado.edu/~bart/book/book/chapter2/ch2_6.htm, 2011.
- [180] B. V. Zeghbroeck. Principles of Semiconductor Devices. http://ecee.colorado.edu/~bart/book/book/chapter2/ch2_7.htm, 2011.
- [181] V. Zayets. Spin and Charge Transport in Materials with Spin-Dependent Conductivity. *Physical Review B*, 86:174415, 2012.
- [182] S. Selberherr. *Analysis and Simulation of Semiconductor Devices*. Springer Vienna, 1984.
- [183] T. Simlinger. *Simulation von Heterostruktur-Feldeffekttransistoren*. PhD thesis, Fakultät für Elektrotechnik, Technischen Universität Wien, Austria, 1996.
- [184] T. Ayalew. *SiC Semiconductor Devices Technology, Modeling, and Simulation*. PhD thesis, Fakultät für Elektrotechnik und Informationstechnik, Technischen Universität Wien, Austria, 2004.
- [185] M. Pourfath. *Numerical Study of Quantum Transport in Carbon Nanotube Based Transistors*. PhD thesis, Fakultät für Elektrotechnik und Informationstechnik, Technischen Universität Wien, Austria, 2007.
- [186] D. L. Scharfetter and H. K. Gummel. Large-Signal Analysis of a Silicon Read Diode Oscillator. *IEEE Transactions on Electron Devices*, 16:64–77, 1969.

- [187] C. Fischer. *Bauelementsimulation in einer Computergestützten Entwurfsumgebung*. PhD thesis, Fakultät für Elektrotechnik, Technischen Universität Wien, Austria, 1994.
- [188] D. Vasileska, S. M. Goodnick, and G. Klimeck. *Computational Electronics: Semiclassical and Quantum Device Modeling and Simulation*. CRC Press Online, 2010.
- [189] B. V. Zeghbroeck. Principles of Semiconductor Devices. <http://ecee.colorado.edu/~bart/book/glossary.htm>, 2011.
- [190] J. Ghosh, V. Sverdlov, and S. Selberherr. Spin Diffusion and the Role of Screening Effects in Semiconductors. In *Proceedings of the 17th International Workshop on Computational Electronics (IWCE)*, pages 1–4, 2014.
- [191] Y. V. Pershin and M. D. Ventra. Spin Blockade at Semiconductor/Ferromagnet Junctions. *Physical Review B*, 75:193301, 2007.
- [192] J. Ghosh, V. Sverdlov, T. Windbacher, and S. Selberherr. Spin Injection and Diffusion in Silicon Based Devices from a Space Charge Layer. *Journal of Applied Physics*, 115(17):17C503–1–17C503–3, 2014.
- [193] J. Ghosh, T. Windbacher, V. Sverdlov, and S. Selberherr. Spin Injection in a Semiconductor Through a Space-Charge Layer. *Solid-State Electronics*, 101:116–121, 2014.

Own Publications

- [1] J. Ghosh, D. Osintsev, V. Sverdlov, and S. Selberherr. Enhancement of Electron Spin Relaxation Time in Thin SOI Films by Spin Injection Orientation and Uniaxial Stress. *Journal of Nano Research*, 39:34–42, 2016.
- [2] J. Ghosh, D. Osintsev, V. Sverdlov, and S. Selberherr. Intersubband Spin Relaxation Reduction and Spin Lifetime Enhancement by Strain in SOI Structures. *Microelectronic Engineering*, 147:89–91, 2015.
- [3] T. Windbacher, J. Ghosh, A. Makarov, V. Sverdlov, and S. Selberherr. Modelling of Multipurpose Spintronic Devices. *International Journal of Nanotechnology*, 12:313–331, 2015.
- [4] J. Ghosh, T. Windbacher, V. Sverdlov, and S. Selberherr. Spin Injection in a Semiconductor Through a Space-Charge Layer. *Solid-State Electronics*, 101:116–121, 2014.
- [5] J. Ghosh, T. Windbacher, V. Sverdlov, and S. Selberherr. Spin Injection and Diffusion in Silicon Based Devices from a Space Charge Layer. *Journal of Applied Physics*, 115(17):17C503–1–17C503–3, 2014.
- [6] J. Ghosh, D. Osintsev, V. Sverdlov, and S. Selberherr. Variation of Spin Lifetime with Spin Injection Orientation in Strained Thin Silicon Films. *ECS Transactions*, 66:233–240, 2015.
- [7] J. Ghosh, D. Osintsev, V. Sverdlov, J. Weinbub, and S. Selberherr. Evaluation of Spin Lifetime in Thin-Body FETs: A High Performance Computing Approach. *Lecture Notes in Computer Science*, 9374:285–292, 2015.
- [8] J. Ghosh, D. Osintsev, V. Sverdlov, and S. Selberherr. Dependence of Spin Lifetime on Spin Injection Orientation in Strained Silicon Films. In *Proceedings of the Joint International EUROSIOI Workshop and International Conference on Ultimate Integration on Silicon (EUROSIOI-ULIS)*, pages 285–288. IEEE, 2015.
- [9] J. Ghosh, D. Osintsev, V. Sverdlov, and S. Selberherr. Injection Direction Sensitive Spin Lifetime Model in a Strained Thin Silicon Film. In *Proceedings of the 20th International Conference on Simulation of Semiconductor Processes and Devices (SISPAD)*, pages 277–280, 2015.

- [10] J. Ghosh, V. Sverdlov, and S. Selberherr. Influence of Valley Splitting on Spin Relaxation Time in a Strained Thin Silicon Film. In *Proceedings of the 18th International Workshop on Computational Electronics (IWCE)*, pages 1–4, 2015.
- [11] V. Sverdlov, J. Ghosh, A. Makarov, T. Windbacher, and S. Selberherr. CMOS-Compatible Spintronic Devices. In *Proceedings of the 30th Symposium on Microelectronics Technology and Devices (SBMicro)*, 2015.
- [12] V. Sverdlov, J. Ghosh, A. Makarov, T. Windbacher, and S. Selberherr. Silicon and CMOS-Compatible Spintronics. In *Proceedings of the International Conference on Applied Physics, Simulation and Computers (APSAC 2015)*, pages 17–20. Recent advances in Computer Engineering, 2015.
- [13] V. Sverdlov, J. Ghosh, A. Makarov, T. Windbacher, and S. Selberherr. Silicon Spintronics: Recent Advances and Challenges. In *Proceedings of the 2015 International Conference and School for Young Scientists Information Technology and Nanotechnology (ITNT)*, 2015.
- [14] J. Ghosh, V. Sverdlov, and S. Selberherr. Spin Diffusion and the Role of Screening Effects in Semiconductors. In *Proceedings of the 17th International Workshop on Computational Electronics (IWCE)*, pages 1–4, 2014.
- [15] V. Sverdlov, J. Ghosh, D. Osintsev, and S. Selberherr. Modeling Silicon Spintronics. In *Recent Advances in Mathematical Methods in Applied Sciences*, volume 32, pages 195–198, 2014.
- [16] V. Sverdlov, J. Ghosh, H. Mahmoudi, A. Makarov, D. Osintsev, T. Windbacher, and S. Selberherr. Modeling of Spin-Based Silicon Technology. In *Proceedings of the International Conference on Ultimate Integration on Silicon (ULIS)*, pages 1–4, 2014.
- [17] V. Sverdlov, J. Ghosh, H. Mahmoudi, A. Makarov, D. Osintsev, T. Windbacher, and S. Selberherr. Modeling Spin-Based Electronic Devices. In *Proceedings of the 29th International Conference on Microelectronics*, pages 27–34, 2014.
- [18] J. Ghosh, V. Sverdlov, and S. Selberherr. Influence of a Space Charge Region on Spin Transport in Semiconductor. In *Proceedings of the International Semiconductor Device Research Symposium (ISDRS)*, page 27, 2013.
- [19] J. Ghosh, D. Osintsev, V. Sverdlov, and S. Selberherr. Increase of Surface Roughness and Phonon Scattering Mediated Spin Lifetime in Thin Strained SOI Film. In *Book of Abstracts of the 2015 E-MRS Fall Meeting*, 2015.
- [20] J. Ghosh, D. Osintsev, V. Sverdlov, and S. Selberherr. Intersubband Spin Relaxation Reduction and Spin Lifetime Enhancement by Strain in SOI Structures. In *Book of Abstracts of the 19th Conference on Insulating Films on Semiconductors*, pages 235–236, 2015.

- [21] J. Ghosh, D. Osintsev, V. Sverdlov, and S. Selberherr. Spin Lifetime Dependence on Spin Injection Orientation in Strained Silicon Films. In *Bulletin of the American Physical Society (APS March Meeting)*, volume 60/1, 2015.
- [22] J. Ghosh, D. Osintsev, V. Sverdlov, and S. Selberherr. Spin Lifetime Dependence on Valley Splitting in Thin Silicon Films. In *Book of Abstracts of the 18th International Workshop on Computational Electronics (IWCE)*, pages 35–36, 2015.
- [23] J. Ghosh, D. Osintsev, V. Sverdlov, and S. Selberherr. Variation of Spin Lifetime with Spin Injection Orientation in Strained Thin Silicon Films. In *Proceedings of the 227th ECS Meeting (ECS)*. ECS Transactions, 2015.
- [24] J. Ghosh, V. Sverdlov, and S. Selberherr. Increment of Spin Lifetime by Spin Injection Orientation in Stressed Thin SOI Films. In *Program and Abstract Book of the 8th International School & Conference on Spintronics and Quantum Information Technology*, page 130, 2015.
- [25] D. Osintsev, J. Ghosh, V. Sverdlov, J. Weinbub, and S. Selberherr. Spin Lifetime in MOSFETs: A High Performance Computing Approach. In *Book of Abstracts of the 10th International Conference on Large-Scale Scientific Computations (LSSC)*, pages 60–61, 2015.
- [26] V. Sverdlov, J. Ghosh, A. Makarov, T. Windbacher, and S. Selberherr. Silicon spintronics. In *Book of Abstracts of the NATO Advanced Research Workshop "Functional Nanomaterials and Devices for Electronics, Sensors, Energy Harvesting"*, pages 44–45, 2015.
- [27] V. Sverdlov, J. Ghosh, A. Makarov, T. Windbacher, and S. Selberherr. Spin-Driven Applications of Silicon and CMOS-Compatible Devices. In *Proceedings of the BIT's 5th Annual Congress of Nano Science and Technology-2015*, page 175, 2015.
- [28] V. Sverdlov, J. Ghosh, D. Osintsev, and S. Selberherr. Electron Spin Lifetime Enhancement by Shear Strain in Thin Silicon Films. In *Book of Abstracts of the 2015 CMOS Emerging Technologies Research Symposium (CMOSETR)*, page 58. Google Books, 2015.
- [29] V. Sverdlov, D. Osintsev, J. Ghosh, and S. Selberherr. Strained Silicon-on-Insulator for Spintronic Applications: Giant Spin Lifetime Enhancement. In *Book of Abstracts of the Advanced Research Workshop on Future Trends in Microelectronics: Journey into the Unknown*, page 63, 2015.
- [30] J. Ghosh, D. Osintsev, V. Sverdlov, and S. Selberherr. Evaluation of Spin Lifetime in Thin Silicon Films by Multilevel Parallelization. Posterpresentation: nanoHUB User Conference, West Lafayette, Indiana, USA, 2015.
- [31] J. Ghosh, V. Sverdlov, and S. Selberherr. Spin Diffusion in Silicon from a Ferromagnetic Contact. In *Book of Abstracts of the 10th European Conference on Magnetic Sensors and Actuators (EMSA 2014)*, page 165, 2014.

- [32] J. Ghosh, V. Sverdlov, and S. Selberherr. Spin Injection in Silicon: The Role of Screening Effects. In *Book of Abstracts of the 17th International Workshop on Computational Electronics (IWCE)*, pages 63–64, 2014.
- [33] V. Sverdlov, J. Ghosh, D. Osintsev, and S. Selberherr. Modeling Silicon Spintronics. In *Book of Abstracts of the International Conference on Mathematical Models and Methods in Applied Sciences*, page 78, 2014.
- [34] J. Ghosh, T. Windbacher, V. Sverdlov, and S. Selberherr. Spin Injection and Diffusion in Silicon Based Devices from a Space Charge Layer. In *Book of Abstracts of the 58th Annual Conference of Magnetism and Magnetic Materials (MMM)*, pages 713–714, 2013.
- [35] J. Ghosh, D. Reuter, M. Rennau, K. Hiller, G. Salvan, M. Fronk, D. R. T. Zahn, C. C. Bof Buffon, and O. Schmidt. I-V Characteristics of Copper Phthalocyanine Based Laterally Stacked Devices Fabricated by Semiconductor Processing. In *Book of Abstracts of the Deutsche Physikalische Gesellschaft (DPG)*, 2012.

Curriculum Vitae

July 2001 – June 2005

Jadavpur University, Calcutta, India
Bachelor's of Electrical Engineering
Concentration: Control System Engineering
Graduation with honors

Oct. 2005 – July 2008

IBM India Pvt. Ltd., Kolkata, India
Working as a Software Engineer

Nov. 2008 – April 2011

TU Chemnitz, Chemnitz, Germany
Graduate program in Micro and Nano Systems
Masters's Thesis: "Fabrication of Laterally Stacked Spin Devices by Semiconductor Processing"

May 2011 – Dec. 2011

TU Chemnitz, Chemnitz, Germany
Project Assistant at the Department of Semiconductor Physics

Mar. 2012 – Aug. 2012

TU Wien, Vienna, Austria
Project Assistant at Insitute for Microelectronics

since May 2013

TU Wien, Vienna, Austria
Enrolled in a full Ph.D. program at the Institute for Microelectronics under the supervision of Prof. Viktor Sverdlov